IntechOpen

Optoelectronics
Recent Advances

Edited by Touseef Para

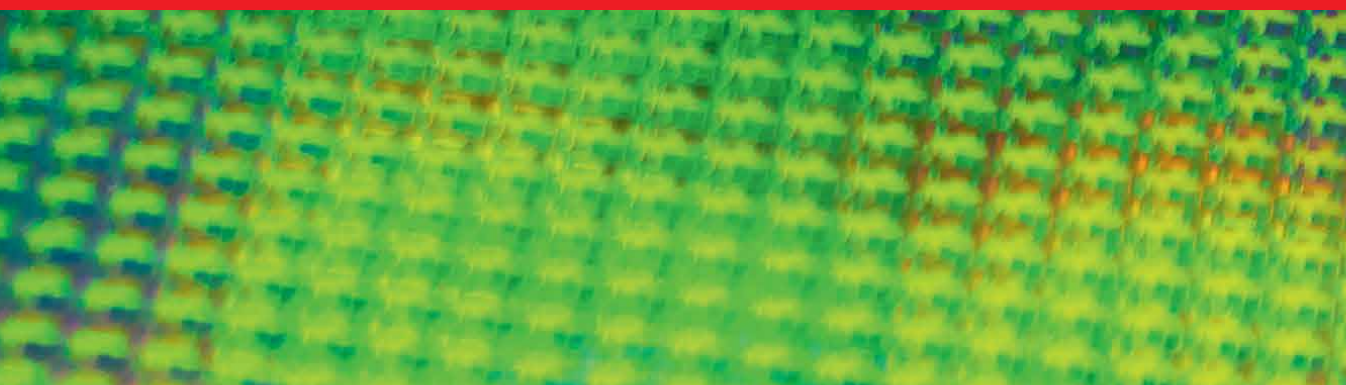

Optoelectronics - Recent Advances

Edited by Touseef Para

Published in London, United Kingdom

Optoelectronics - Recent Advances
http : //dx . doi . org/10 . 5772/intechopen . 110929
Edited by Touseef Para

Contributors
Touseef Para , Puskar Chapagain , Suman Neupane , Hai-Zhi Song , Qiang Zhou , Guangwei Deng , Qian Dai , Zichang Zhang , You Wang , Viktor Pachkov , Jie Lin , Geng He , Yun Hu , Jingsong Huang , Pantea Nadimi Goki , Thomas Teferi Mulugeta , Nicola Sambo , Roberto Caldelli , Ramin Solaimani , Luca Potì , Abhivyakti Gautam

First published in London , United Kingdom , 2024 by IntechOpen
IntechOpen is the global imprint of INTECHOPEN LIMITED , registered in England and Wales , registration number : 11086078 , 5 Princes Gate Court , London , SW7 2QJ , United Kingdom

British Library Cataloguing-in-Publication Data
A catalogue record for this book is available from the British Library

Additional hard and PDF copies can be obtained from orders@intechopen . com

Optoelectronics - Recent Advances
Edited by Touseef Para
p . cm .
Print ISBN 978-1-83769-796-0
Online ISBN 978-1-83769-795-3
eBook (PDF) ISBN 978-1-83769-797-7

Meet the editor

Touseef Para, with a Master's, M. Phil, and Ph.D. in Physics, is a distinguished researcher and educator. Published in various reputed international journals, he brings extensive teaching experience across undergraduate, graduate, and postgraduate levels. A recipient of the Young Scientist Award, Para has contributed to reputable Indian research institutes like UGC DAE CSR Indore, NCL Pune, IIT Bombay, NPL Delhi, IIT ISM Dhanbad. His expertise spans Crystallography, XRD, Rietveld refinement, XPS, Raman, IR, UV Vis spectroscopies, solar cells, and Na-ion batteries. Currently focused on upscaling Na-ion battery manufacturing, Para is not only a dedicated scientist but also a proud son, husband, and father.

Contents

Preface

Welcome to *Optoelectronics – Recent Advances* an anthology that delves into the fascinating realm of optoelectronics through the lens of diverse expertise and perspectives. As the editor of this compilation, I am thrilled to present a collection of chapters that collectively illuminate the multifaceted recent landscape of optoelectronic research.

The journey begins with an enlightening Introductory Chapter that sets the stage for our exploration of the intricate world of optoelectronics. Each subsequent chapter contributes a unique thread to this narrative, offering insights and discoveries that span the breadth of this dynamic field.

Chapter 2 takes us on a journey through the longitudinal assembly of gold nanorods on various templates, showcasing the versatility of optoelectronics in material science. Meanwhile, Chapter 3 explores the intersection of optoelectronics and quantum information processing, revealing the potential for groundbreaking advancements at the nexus of these two fields.

In Chapter 4, we encounter an algorithm designed for calculating the coordinates of images in an optoelectronic device with a matrix photodetector, highlighting the crucial role of computational methods in optimizing device functionality. Chapter 5 pushes the boundaries with an exploration of advances in colloidal quantum dot laser diodes, demonstrating the cutting-edge developments that propel the field forward.

Chapter 6 introduces us to the concept of a device fingerprint as a transmission security paradigm, showcasing the evolving strategies for ensuring the integrity and security of optoelectronic systems. Finally, in Chapter 7, we gain a broader perspective on the integration of optoelectronics into neural interfaces, opening new horizons for the intersection of technology and neuroscience.

This collection is a testament to the collaborative effort of experts in the field, each chapter representing a unique facet of optoelectronics. I extend my sincere appreciation to all the contributors who have shared their knowledge and insights, enriching this anthology with a tapestry of ideas.

As you embark on this journey through the chapters of this book, I invite you to explore the ever-expanding boundaries of optoelectronics and witness the transformative potential that lies within this dynamic field.

Enjoy.

Touseef Para
Department of Energy Science and Engineering,
Indian Institute of Technology Bombay,
Mumbai, India

Section 1

Introduction

Chapter 1

Introductory Chapter: Optoelectronics

Touseef Para

1. Introduction

Optoelectronics, the seamless union of optics and electronics, represents one of the most captivating and transformative fields of modern science and technology. It delves into the intricate interactions between light and electronic devices, giving birth to an array of innovations that have revolutionized the modern world. From the crisp color rendition of a smartphone screen to the precise pulse of a laser surgery tool, optoelectronics is powering the modern world in unimaginable ways.

The interaction between light and electricity has been harnessed by humankind for centuries. From the earliest observations of sunlight magnified through a glass lens to the development of the first solid-state lasers, our fascination with manipulating light and harnessing its properties has led to a profound understanding of the fundamental principles governing this intriguing realm. The subject of optics has been fascinating to the world from ancient times, either in the form of myths or the purely stupendous scientific inquisition. People often depicted light, optical phenomena, and sources of light as divine and heavenly, so much so that many civilizations prayed to them or considered them gods. And civilizations that did not concur with this idea sought light as the pathway to salvation, tranquility, and serendipity. Many skeptical minds arose from these ranks who tried to understand the light as materialistic as other physical quantities. Among the first who actually used light as the source of power and energy was Archimedes. Although not replicable, his infamous and alleged blaze of Roman ships on the Tyrrhenian Sea is more progressive as a concept. What followed the incident in the coming centuries propelled the world into a new light (or fire).

The journey of optoelectronics began long before the term was even coined. In the nineteenth century, Thomas Young's double-slit experiment laid the foundation for wave-particle duality, which would become fundamental in understanding light's nature. Building upon Young's work, James Clerk Maxwell's equations revolutionized our understanding of electromagnetism and light propagation. This newfound knowledge opened the doors to the development of telegraphy and, eventually, fiber optic communications that connect our world today.

In the early twentieth century, Albert Einstein's groundbreaking work on the photoelectric effect unveiled the particle nature of light and inspired the development of photodetectors. World War II saw the emergence of optoelectronic devices such as night-vision goggles and proximity fuzes, laying the groundwork for modern military technology.

The term "optoelectronics" emerged in the mid-twentieth century to describe a burgeoning field that sought to exploit the symbiotic relationship between optics and electronics. Researchers began to explore the potential of materials capable of

controlling and manipulating light through electronic means. This era witnessed the birth of key optoelectronic devices, including the light-emitting diode (LED) and the semiconductor laser, both of which would become indispensable in modern technology.

Today, optoelectronics finds applications across an astonishingly diverse range of fields, from information and communication technologies, where it underpins the internet and enables high-speed data transmission, to healthcare, where it plays a pivotal role in medical imaging and non-invasive diagnostics. Optoelectronics also enhances our understanding of the cosmos through telescopes and space-based sensors, while simultaneously transforming industries such as automotive, energy, and manufacturing.

As we embark on this journey into the realm of optoelectronics, we will explore the fundamental principles that govern the interactions between light and electronic materials. We will delve into the construction and operation of key optoelectronic devices, understanding their significance in both historical and contemporary contexts. Moreover, we will uncover the latest innovations and future prospects of optoelectronics, contemplating the remarkable advancements that lie ahead and their potential to shape our world.

In the following sections, we will navigate the intricate pathways of photons and electrons, seeking to unravel the mysteries and harness the potential of optoelectronics. Join us on this captivating voyage as we explore the boundless possibilities that emerge when light and electronics converge, paving the way for a brighter and more connected future.

2. Nature of light

2.1 Wave nature of light

Light, as we perceive it in our everyday lives, is a phenomenon that can be understood through the lens of both wave and particle characteristics. In this section, we will delve into the wave nature of light, which provides a fundamental framework for comprehending its behavior and interactions. However, another aspect of light needs to be considered first, the geometric optics.

2.1.1 Reflection and refraction

The first scientific description of propagation and interaction of light with objects around us was made using geometric optics and few obsolete ideas [1]. The geometric optics led to the optical revolution, where we could peek into the world invisible to the naked eye both in size and distance, with the advent of microscopes and telescopes. At the heart of it were the laws of reflection and refraction.

2.1.1.1 Reflection

Reflection is a fundamental optical phenomenon that occurs when light encounters a surface and bounces back in accordance with the law of reflection [1]. This law states that the angle of incidence ($\theta_{incident}$) is equal to the angle of reflection ($\theta_{reflection}$), both

measured with respect to the normal (an imaginary line perpendicular to the surface) at the point of incidence.

Mathematically, the law of reflection can be expressed as:

$$\theta_{incident} = \theta_{reflected} \tag{1}$$

Reflection is responsible for a wide range of everyday experiences, from seeing your own reflection in a mirror to the way light interacts with polished surfaces. It is also the basis for various optical devices, such as periscopes and retroreflectors, which use multiple reflections to redirect light.

2.1.1.2 Refraction

Refraction, on the other hand, is the bending of light as it passes from one medium into another with a different optical density. The optical density of a medium is characterized by its refractive index (η), which is a measure of how much light slows down or speeds up when entering that medium compared to a vacuum.

Snell's law describes the relationship between the angles of incidence and refraction ($\theta_{incident}$ and $\theta_{refracted}$) and the refractive indices of the two media:

$$\eta_1 \bullet \sin(\theta_{incident}) = \eta_2 \bullet \sin\left(\theta_{refracted}\right) \tag{2}$$

Key points about refraction include:

- When light enters a medium with a higher refractive index, it bends toward the normal line, and when it enters a medium with a lower refractive index, it bends away from the normal line.

- The change in speed of light when it enters a different medium results in a change in wavelength and frequency. This phenomenon is responsible for the dispersion of light, where different colors of light are separated when passing through a prism.

- Lenses, such as those found in eyeglasses and cameras, rely on refraction to focus and manipulate light. Concave lenses cause light to diverge, while convex lenses converge light to a point.

- Atmospheric refraction is responsible for optical illusions like the mirage, where objects appear displaced from their actual positions due to the bending of light in different layers of the atmosphere.

Reflection and refraction are essential concepts in the field of optics and optoelectronics, forming the basis for the design of optical components, lenses, and imaging systems. These principles are also at the core of how we perceive the world around us and are integral to many aspects of our daily lives, from the operation of optical sensors to the functioning of eyeglasses and cameras. Understanding these phenomena is crucial for engineers and scientists working in optoelectronics, as they enable the manipulation and control of light for various applications.

2.1.2 Wave-particle duality

The wave-particle duality of light is a fundamental concept in physics that emerged in the late 17th and early 18th centuries. It posits that light exhibits both wave-like and particle-like properties depending on the circumstances of observation. This duality is not limited to light; it extends to all particles and is encapsulated in the famous principle enunciated by Louis de Broglie in the 1920s, which states that particles, like electrons and photons (the particles of light), can exhibit both wave and particle characteristics.

2.1.3 Wavelength and frequency

At its core, the wave nature of light can be characterized by its wavelength (λ) and frequency (ν). Wavelength represents the spatial extent of one complete cycle of the wave, usually measured in units such as meters (m) or nanometers (nm). Frequency, on the other hand, denotes the number of oscillations or cycles that occur in 1 second, typically measured in hertz (Hz).

The relationship between wavelength and frequency is described by the wave equation:

$$c = \lambda\nu \tag{3}$$

where:

- c is the speed of light in a vacuum (approximately 3×10^8 meters per second),
- λ is the wavelength of the light,
- ν is the frequency of the light.

This equation illustrates a fundamental principle: as the wavelength of light decreases, its frequency increases, and vice versa. This relationship has profound implications for the behavior of light.

2.1.4 Interference and diffraction

One of the key phenomena associated with the wave nature of light is interference. When two or more light waves of the same frequency meet, they can either reinforce each other (constructive interference) or cancel each other out (destructive interference). This phenomenon is the basis for various optical devices like diffraction gratings, which split light into its constituent colors or patterns.

Diffraction, another consequence of the wave nature of light, occurs when light waves encounter an obstacle or aperture. Instead of producing a sharp shadow, as particles would, light exhibits a diffraction pattern characterized by bright and dark regions. This behavior is instrumental in fields such as optics, where it allows for precise measurements and the design of optical elements.

2.1.5 Polarization

The wave nature of light is also responsible for polarization, a property that describes the orientation of the electric field vector within a light wave. Polarizers,

such as those used in sunglasses, selectively allow light waves with a particular orientation of the electric field to pass through while blocking others. Understanding polarization is crucial in applications like 3D cinema, liquid crystal displays (LCDs), and optical communications.

In summary, the wave nature of light is a foundational concept that underpins our understanding of how light propagates and interacts with matter. It enables us to explain a wide range of optical phenomena and serves as the basis for many optical technologies and devices. To fully appreciate the world of optoelectronics, it is essential to grasp the intricate wave-like properties of light and how they influence the design and operation of optoelectronic systems.

2.2 Particle nature of light

While the wave nature of light provides a comprehensive framework for understanding many optical phenomena, the particle nature of light, as described by quantum theory, offers a different perspective that is equally essential for a complete understanding of light's behavior. This duality, wherein light exhibits characteristics of both waves and particles, is known as wave-particle duality and is a cornerstone of modern physics.

2.2.1 Photons: Quantum particles of light

In the early twentieth century, Albert Einstein, in his groundbreaking work on the photoelectric effect, proposed that light consists of discrete packets of energy, each carrying a quantum of electromagnetic energy. These packets of energy were named "photons." Photons are quantum particles that behave both as particles and as waves, depending on the context of observation.

The particle nature of light is described by photons, which are discrete packets of energy. This concept is crucial in understanding the behavior of light at the quantum level. Photons are fundamental in various optoelectronic devices, including photodetectors, lasers, and solar cells.

The energy (E) of a photon is directly proportional to its frequency (ν) or inversely proportional to its wavelength (λ) and can be calculated using the following equation:

$$E = h\nu \tag{4}$$

where:

E = Energy of the photon (in joules, J).

h = Planck's constant (6.626×10^{-34} joule-seconds, J·s).

ν = Frequency of the photon (in hertz, Hz).

Additionally, the speed of light (c) is related to the frequency and wavelength of light by Eq. (4).

This particle-like behavior of light is crucial in understanding phenomena like the photoelectric effect, where photons striking a material surface can eject electrons from it. It also plays a key role in the operation of devices like photodetectors, which convert incident photons into electrical current.

In quantum mechanics, the probability of finding a photon with a specific energy E in a given state is described by the photon's wavefunction, typically represented by the symbol ψ. The square of the magnitude of this wavefunction, $|\psi|^2$, represents the probability density of finding the photon with energy E in a particular region of space.

Key characteristics of photons include:

Energy quantization: Photons have discrete energy levels determined by their frequency. Higher-frequency light (shorter wavelengths) carries more energy per photon than lower-frequency light.

Wave-particle duality: Photons exhibit wave-like behavior, such as interference and diffraction, when considered collectively. However, when interacting with matter, they manifest as discrete particles with well-defined energy.

No mass: Photons are massless particles, which is a unique feature among elementary particles in the Standard Model of particle physics.

Travel at the speed of light: Photons always travel at the speed of light (\(c\)) in a vacuum and undergo no acceleration. In other media, their speed is slightly reduced due to interactions with atoms and molecules [2].

2.2.2 Particle aspects of light: The photoelectric effect

The photoelectric effect, first observed by Heinrich Hertz and later explained by Albert Einstein, provides strong evidence for the particle nature of light [3]. In this phenomenon, photons striking the surface of a material can transfer their energy to electrons within the material. If the energy of a photon exceeds the work function of the material (the minimum energy required to release an electron), the electron is emitted from the material. The energy of the emitted electrons depends on the frequency (or wavelength) of the incident light, not its intensity. This phenomenon forms the basis for photodetectors and solar cells.

The photoelectric effect is a phenomenon in which electrons are emitted from a material's surface when it is exposed to light. This effect played a crucial role in establishing the particle nature of light and is described by several key equations.

Einstein's photoelectric equation: The energy E of electrons emitted in the photoelectric effect is given by Einstein's photoelectric equation:

$$E = h\nu - \phi \tag{5}$$

where:

E = Energy of the emitted electron (in electronvolts, eV).

h = Planck's constant (\(6.626 \times 10^{-34}\) joule-seconds, J·s).

ν = Frequency of the incident light (in hertz, Hz).

ϕ = Work function of the material (in electronvolts, eV).

The work function represents the minimum energy required to release an electron from the material's surface. If the energy of the incident photons ($h\nu$) is greater than the work function (ϕ), electrons are emitted with kinetic energy (E_k).

Kinetic energy of emitted electrons: The kinetic energy of the emitted electrons can be calculated as:

$$E_k = h\nu - \phi \tag{6}$$

where:

E_k = Kinetic energy of the emitted electron (in electronvolts, eV).

Maxwell's equation for the photoelectric current: The photoelectric current (\(I\)) is the flow of electrons emitted from the material. It is described by Maxwell's equation:

$$I = \eta A e \tag{7}$$

where:

I = Photoelectric current (in amperes, A).

η = Number of electrons emitted per second.

A = Area of the material's surface exposed to light (in square meters, m^2).

e = Elementary charge ((1.602×10^{-19}) coulombs, C).

The photoelectric effect has important applications, such as in photodetectors and solar cells, where it is used to convert light energy into electrical energy.

2.2.3 Complementarity of wave and particle descriptions

Wave-particle duality implies that the description of light depends on the context of observation. In some experiments, light behaves as a wave, exhibiting interference and diffraction patterns. In others, it behaves as discrete particles (photons), particularly in interactions with matter. This dual nature is not unique to light; it extends to other particles, such as electrons and even larger molecules, although the manifestations differ.

Understanding the particle nature of light is vital in the realm of optoelectronics, particularly in the design and operation of photodetectors, imaging sensors, and photon sources. Photons play a crucial role in the transmission of information in optical fiber communication and the generation of light in lasers, making the concept of light as both a wave and a particle central to the advancement of optical technologies and quantum optics.

3. Electronics revolution

3.1 Light blubs

3.1.1 Incandescent light bulbs

Incandescent light bulbs, often associated with the pioneering work of Thomas Edison, are one of the oldest and most familiar types of electric lighting [4]. These bulbs operate on a relatively simple principle: when an electric current passes through a filament, the filament heats up to a high temperature, causing it to emit visible light. The filament inside an incandescent bulb is typically made of tungsten, a material with a high melting point. When electricity flows through the filament, it heats up due to resistance, reaching temperatures of around 2700 to 3300 degrees Celsius (4800 to 5900 degrees Fahrenheit). This extreme heat causes the filament to glow, producing visible light. Incandescent bulbs are known for their inefficiency. A significant portion of the electrical energy they consume is transformed into heat rather than visible light. This makes them energy-inefficient compared to other lighting technologies. Incandescent bulbs emit a warm and pleasing quality of light, with a color temperature that is often described as "soft white" or "warm white." This warm color rendering is favored in some residential and decorative lighting applications. Due to their inefficiency and energy consumption, incandescent bulbs have been phased out or banned in many countries in favor of more energy-efficient lighting technologies like compact fluorescent lamps (CFLs) and light-emitting diodes (LEDs).

3.1.2 Fluorescent light bulbs

Fluorescent light bulbs, commonly known as CFLs (compact fluorescent lamps), are a more energy-efficient alternative to incandescent bulbs [5]. They operate based on the principle of fluorescence and offer several advantages. Inside a fluorescent bulb, a gas (typically mercury vapor) emits ultraviolet (UV) light when excited by an electric current. The UV light then interacts with a phosphor coating on the interior surface of the bulb, causing it to fluoresce and emit visible light.

Energy efficiency: CFLs are significantly more energy-efficient than incandescent bulbs. They produce the same amount of light while consuming a fraction of the electricity. This energy efficiency results in lower energy bills and reduced greenhouse gas emissions.

Longer lifespan: CFLs have a longer lifespan compared to incandescent bulbs, typically lasting around 8000 to 10,000 hours. This longer lifespan reduces the frequency of bulb replacement.

Cooler operation: Unlike incandescent bulbs, CFLs operate at lower temperatures, making them a safer choice, especially in enclosed fixtures. They are also more suitable for applications where heat can be a concern.

Different color temperatures: CFLs are available in various color temperatures, ranging from warm white to cool white. This versatility allows users to select the desired lighting ambiance for different settings.

Mercury content: It is important to note that CFLs contain a small amount of mercury, which can be a concern for environmental disposal. Recycling programs are available to properly handle and dispose of used CFLs.

While CFLs have gained popularity for their energy efficiency, they are gradually being replaced by LED (light-emitting diode) bulbs, which are even more energy-efficient, have a longer lifespan, and do not contain hazardous materials like mercury. LEDs have become the preferred choice for energy-conscious consumers and are rapidly advancing in terms of technology and affordability.

3.2 Lasers and laser diodes

Lasers (light amplification by stimulated emission of radiation) and their miniature counterparts, laser diodes, represent a remarkable class of devices with applications spanning from telecommunications to medical surgery [6, 7]. These devices generate intense, coherent, and monochromatic light, making them indispensable in various fields.

3.2.1 How lasers work

Lasers operate on the principle of stimulated emission within a gain medium. Here is a simplified explanation of how lasers work:

Gain medium: A laser contains a gain medium, which can be a solid, gas, liquid, or semiconductor material. When energy is applied to this medium (through electrical current, optical pumping, or other means), electrons are excited to higher energy levels.

Stimulated emission: When an excited electron encounters a photon with the same energy level (frequency), it can be stimulated to emit another photon of the same energy. This process creates a cascade of photon emissions, resulting in a population inversion—more electrons in higher energy states than lower ones.

Coherent light: As electrons return to lower energy levels, they emit photons that are coherent (in phase) with the stimulating photons. This coherence results in laser light that is highly directional and maintains a single wavelength (monochromatic).

Optical resonator: The gain medium is placed between two mirrors, forming an optical resonator. One of these mirrors is partially reflective, allowing some laser light to escape, while the other is highly reflective, causing photons to repeatedly bounce back and forth through the gain medium, amplifying the light in the process.

Laser emission: Eventually, the intensity of the emitted light exceeds the losses within the optical resonator, and a coherent, intense beam of laser light is emitted through the partially reflective mirror.

3.2.2 Laser diodes

Laser diodes, also known as semiconductor lasers, are compact, efficient, and versatile laser sources that have become integral in various applications [7]. They operate on a similar principle to traditional lasers but with semiconductor materials. Key features and applications of laser diodes include:

Semiconductor Materials: Laser diodes are typically constructed using semiconductor materials like gallium arsenide (GaAs) or indium phosphide (InP). These materials allow for compact and efficient devices.

Diverse wavelengths: Laser diodes can emit light at various wavelengths, making them suitable for applications ranging from telecommunications (e.g., optical fiber communication) to medical devices (e.g., laser surgery).

Small size: The miniature size of laser diodes makes them ideal for integration into electronic devices, including laser pointers, barcode scanners, DVD players, and optical communication transmitters.

Efficiency: Laser diodes are energy-efficient compared to other laser technologies, such as gas lasers. They convert a significant portion of electrical input into laser light.

Modulation: Laser diodes can be modulated rapidly, allowing for applications in data transmission and laser printing.

3.2.3 Applications of lasers and laser diodes

Lasers and laser diodes have a multitude of applications, including:

Telecommunications: They are used in optical fiber communication systems for transmitting data over long distances.

Medical and surgery: Lasers are employed in various medical procedures, such as eye surgery (LASIK), skin treatments, and dental procedures.

Material processing: Lasers are used for cutting, welding, engraving, and marking materials in industries ranging from manufacturing to aerospace.

Scientific research: Lasers play a crucial role in scientific experiments, such as spectroscopy and laser cooling, enabling the study of atomic and molecular behavior.

Entertainment: Laser light shows and laser projectors are popular in entertainment and artistic displays.

In conclusion, lasers and laser diodes are transformative technologies that have found a multitude of applications across diverse fields. Their ability to generate intense and coherent light has paved the way for advancements in communication, healthcare, manufacturing, and scientific research, among many other areas. Their continued development and integration into new technologies hold promise for further innovation and discoveries in the future.

3.3 Displays

3.3.1 Laser displays, LCDs, and TFTs

Optoelectronic devices have found applications in a variety of display technologies, including liquid crystal displays (LCDs) and thin-film transistor (TFT) displays [8]. These technologies have revolutionized the way we view and interact with digital content, from computer monitors to flat-screen televisions.

3.3.1.1 Liquid crystal displays (LCDs)

Liquid crystal displays (LCDs) are a prevalent type of display technology used in a wide range of electronic devices, including computer monitors, televisions, smartphones, and digital watches. LCDs rely on the interaction of liquid crystals and polarized light to produce images. Key features of LCDs include:

Liquid crystals: LCDs contain a layer of liquid crystals sandwiched between two layers of glass or plastic. These liquid crystals can change their orientation when subjected to an electric field.

Polarization: In an LCD, polarized light passes through the liquid crystal layer. The orientation of the liquid crystals can be controlled individually by applying an electric field, thereby modulating the passage of light.

Color generation: LCDs typically use three sub-pixels (red, green, and blue) to create a full spectrum of colors. By adjusting the intensity of each sub-pixel, the display can reproduce a wide range of colors and shades.

Backlighting: Most LCDs require a backlight source to illuminate the liquid crystal layer. This backlight can be provided by LEDs (light-emitting diodes) or CCFLs (cold cathode fluorescent lamps).

Thin-film transistors (TFTs): In Active Matrix LCDs, each pixel is controlled by a thin-film transistor (TFT), which allows for precise and rapid pixel switching. This results in faster refresh rates and improved image quality.

3.3.1.2 Thin-film transistor (TFT) displays

Thin-film transistor (TFT) displays are a specific type of LCD that employs thin-film transistor technology for improved image quality and faster response times. Key characteristics of TFT displays include:

High resolution: TFT displays are known for their high-resolution capabilities, making them suitable for applications where fine details are crucial, such as computer monitors and modern televisions.

Fast response times: The integration of thin-film transistors allows for individual pixel control, resulting in faster response times and reduced motion blur compared to traditional passive matrix LCDs.

Wide viewing angles: TFT displays typically offer wide viewing angles, ensuring that the image quality remains consistent even when viewed from different angles.

Variety of sizes: TFT displays come in various sizes, from small screens used in smartphones and tablets to larger screens for laptops, desktop monitors, and televisions.

3.3.1.3 Laser displays

Laser displays represent an emerging technology that utilizes lasers as the light source for creating images. They offer several advantages, including:

Bright and vivid colors: Lasers can produce exceptionally bright and saturated colors, making laser displays suitable for applications like high-end projectors and large-screen displays.

Long lifespan: Laser diodes have a longer lifespan compared to traditional lamps or bulbs used in projectors, reducing maintenance costs.

Energy efficiency: Laser displays can be energy-efficient, especially when combined with efficient modulation techniques, resulting in energy savings and reduced heat generation.

Laser projection: Laser projectors use lasers as the light source to create images on screens or surfaces. They are becoming popular for home theaters, business presentations, and large-scale events.

In summary, laser displays, LCDs, and TFTs are diverse display technologies that have transformed the way we interact with digital content. Each technology has its own set of advantages and applications, catering to various needs in consumer electronics, information displays, and projection systems. The choice between these technologies often depends on factors such as image quality, power efficiency, and cost-effectiveness for a given application.

3.4 Light-emitting diodes

3.4.1 Red, green, and blue LEDs (Light-emitting diodes)

Light-emitting diodes (LEDs) are semiconductor devices that emit light when current flows through them [9]. LEDs have become ubiquitous in modern technology and lighting due to their energy efficiency, durability, and versatility. Red, green, and blue LEDs, in particular, play a vital role in color displays and lighting applications.

3.4.1.1 Red LEDs

Red LEDs emit light in the red portion of the visible spectrum. They are typically fabricated using semiconductor materials like gallium arsenide phosphide (GaAsP) or aluminum gallium arsenide (AlGaAs). Key characteristics and applications of red LEDs include:

Wavelength: Red LEDs typically emit light with wavelengths in the range of approximately 620 to 750 nanometers (nm).

Applications: Red LEDs are commonly used in applications such as indicator lights on electronic devices, traffic signals, brake lights in vehicles, and some types of display technologies.

Color mixing: In combination with green and blue LEDs, red LEDs are used to create a wide range of colors in RGB color displays and screens.

3.4.1.2 Green LEDs

Green LEDs emit light in the green portion of the visible spectrum. They are fabricated using materials like aluminum gallium indium phosphide (AlGaInP). Some key characteristics and applications of green LEDs include:

Wavelength: Green LEDs typically emit light with wavelengths ranging from approximately 495 to 570 nm.

Applications: Green LEDs are used in applications similar to red LEDs, such as indicator lights and traffic signals. They are also crucial in creating a full spectrum of colors in RGB displays.

Brightness and visibility: Green LEDs are known for their high brightness, making them suitable for outdoor and daylight-visible applications.

3.4.1.3 Blue LEDs

Blue LEDs emit light in the blue portion of the visible spectrum and are made using materials like gallium nitride (GaN) [7, 9]. They played a pivotal role in the development of energy-efficient white LED lighting. Key characteristics and applications of blue LEDs include:

The invention of the blue LED (light-emitting diode) by Shuji Nakamura and his team in the 1990s marked a groundbreaking moment in the world of lighting and display technology. Blue LEDs paved the way for energy-efficient and long-lasting white LED lighting, which has revolutionized the illumination industry, leading to significant energy savings and reduced environmental impact. Furthermore, blue LEDs were instrumental in the development of Blu-ray disc technology, enabling high-capacity optical storage and transforming the way we store and access digital data. This innovation not only earned Nakamura a Nobel Prize but also profoundly impacted various aspects of our daily lives, from the way we light our homes to the way we enjoy high-definition entertainment.

White LEDs, an innovation largely enabled by the combination of blue LEDs and phosphor materials, have revolutionized the lighting industry. These LEDs emit a broad spectrum of light that appears white to the human eye. One remarkable feature of white LEDs is the ability to control the color temperature of the emitted light. By adjusting the composition and thickness of the phosphor coating, manufacturers can fine-tune the color temperature, offering a range of warm to cool white light options. This temperature control allows for the creation of lighting environments that can mimic the warmth of incandescent bulbs or the crispness of daylight. As a result, white LEDs have become the preferred choice for energy-efficient lighting in homes, offices, and public spaces, offering not only significant energy savings but also the flexibility to adapt the lighting ambiance to suit various needs and preferences.

Wavelength: Blue LEDs typically emit light with wavelengths in the range of approximately 450 to 495 nm.

3.4.1.4 White LED lighting and color temperature

Blue LEDs, when combined with a phosphor coating, can produce white light. This innovation has led to the widespread use of white LEDs in general lighting applications, including residential and commercial lighting.

Color mixing: Blue LEDs, in combination with red and green LEDs, form the basis of RGB color displays, screens, and illumination systems. By adjusting the intensity of each color, a broad spectrum of colors can be achieved.

Optical storage: Blue lasers, which are a specific type of blue LED, are used in optical storage devices like Blu-ray disc players.

RGB LEDs: RGB LEDs are devices that combine red, green, and blue LEDs into a single package. By individually controlling the brightness of these three colors, RGB LEDs enable a wide range of color possibilities. They are commonly used in:

Color displays: RGB LEDs are employed in displays and screens, including LED TVs, computer monitors, and large-scale video walls.

Decorative lighting: RGB LEDs are popular in decorative lighting applications, allowing users to customize and change the color of lighting fixtures.

Artistic displays: RGB LEDs are used in art installations, stage lighting, and architectural lighting to create dynamic and colorful visual effects.

In summary, red, green, and blue LEDs, along with RGB LEDs, have revolutionized lighting and display technologies. They are the building blocks of modern color displays and lighting systems, offering energy-efficient and versatile solutions for a wide range of applications in consumer electronics, lighting design, and visual communication.

3.5 Optical fiber

Optical fiber: Optical fibers are thin, flexible strands of glass or plastic that can transmit data in the form of light pulses [10]. They are a cornerstone of modern telecommunications and data transmission systems. The key advantage of optical fibers is their ability to carry vast amounts of data over long distances at incredibly high speeds.

The principle behind optical fibers is total internal reflection. When light enters the fiber at a shallow angle, it reflects off the inner walls due to the higher refractive index of the core compared to the cladding. This reflection keeps the light confined within the core, allowing it to travel long distances without significant loss of signal.

Optical fibers are widely used in telecommunications networks, including the internet's backbone. They are also essential in various industries, such as healthcare (endoscopy), manufacturing (industrial lasers), and military applications. The reliability, speed, and capacity of optical fiber communication have transformed the way we connect, share information, and communicate globally.

3.5.1 Fiber optic communication systems

Fiber optic communication systems: Fiber optic communication systems represent a revolutionary means of transmitting data, voice, and video information over long distances using optical fibers. These systems have become the backbone of modern global communication networks. Here are some key aspects of fiber optic communication systems:

Data transmission: Fiber optic systems transmit data by modulating light signals, typically in the infrared range. Information is encoded into the light, which is then transmitted through the optical fiber.

Low signal loss: Optical fibers have minimal signal loss compared to traditional copper cables. This allows for data transmission over vast distances without the need for frequent signal regeneration.

High bandwidth: Fiber optic systems offer exceptionally high bandwidth capabilities, enabling the transmission of large volumes of data at incredibly high speeds. This is crucial for supporting modern internet services, streaming media, and other data-intensive applications.

Security: Fiber optic cables are difficult to tap into without being detected, making them more secure than traditional copper cables, which can be vulnerable to eavesdropping.

Immunity to electromagnetic interference (EMI): Unlike copper cables, fiber optics are not affected by electromagnetic interference, making them suitable for use in environments with high levels of EMI, such as industrial settings.

Longevity and reliability: Fiber optic cables have a long lifespan and are highly durable, requiring less maintenance compared to traditional cables. They are also less susceptible to environmental factors like moisture and temperature variations.

Versatility: Fiber optic communication systems are used in various applications, including long-distance telecommunications, local area networks (LANs), internet connections, cable television (CATV), and submarine communications.

Multiplexing: Optical fibers support techniques like wavelength-division multiplexing (WDM) and time-division multiplexing (TDM), allowing multiple data streams to be transmitted simultaneously over a single fiber.

Future-proofing: Fiber optic networks are considered future-proof because they have the potential to support even higher data rates as technology advances, making them a wise investment for long-term infrastructure planning.

Overall, fiber optic communication systems have transformed the way the world communicates and shares information. They have become essential for global connectivity, enabling real-time communication, high-definition video streaming, and rapid data exchange on a scale that was once unimaginable.

3.6 Photosensors: capturing light for information

Photosensors, also known as photodetectors or light sensors, are devices designed to detect and measure light or other electromagnetic radiation. They play a critical role in various applications, ranging from cameras and smartphones to industrial automation and scientific instruments. Photosensors convert incoming photons of light into electrical signals, allowing us to capture and quantify light in many forms. Some common types of photosensors include:

Photodiodes: These semiconductor devices generate a current or voltage when exposed to light. Photodiodes are commonly used in applications like light meters, optical communication systems, and cameras to capture images.

Phototransistors: Similar to photodiodes, phototransistors are also light-sensitive semiconductor devices, but they provide amplification of the incoming light signal, making them useful for low-light detection and optical switching applications.

Photomultiplier tubes (PMTs): PMTs are highly sensitive detectors that can amplify single photon signals. They find applications in nuclear physics, fluorescence measurements, and other low-light situations where extreme sensitivity is required.

Photovoltaic cells (Solar Cells): Photovoltaic cells convert sunlight into electricity, providing a sustainable and renewable energy source for various applications, including solar panels for generating electrical power.

Avalanche photodiodes (APDs): APDs are specialized photodiodes that operate in high-gain avalanche mode. They are used in applications demanding high sensitivity, such as LIDAR (light detection and ranging) systems and laser rangefinders.

Photosensors are crucial components in modern technology, enabling everything from digital photography and remote sensing to medical diagnostics and automation. The ability to convert light into electrical signals has transformed the way we collect

data, monitor our environment, and capture images, making photosensors indispensable in our daily lives and numerous scientific and industrial applications.

3.7 Solar cells: Harnessing the power of the sun

Solar cells, also known as photovoltaic cells, are devices that convert sunlight into electricity through a process known as the photovoltaic effect [11–16]. They are a sustainable and renewable energy source with a wide range of applications, from powering small electronic devices to generating electricity for homes and large-scale power plants. Here, we explore various types of solar cells:

3.7.1 Silicon crystal solar cells

Monocrystalline silicon solar cells: These solar cells are made from a single crystal structure, providing high efficiency and a long lifespan. They are known for their uniform appearance and high cost.

Polycrystalline silicon solar cells: Polycrystalline cells consist of multiple silicon crystals. They are less expensive to manufacture but slightly less efficient than monocrystalline cells.

3.7.2 Thin-film solar cells

Thin-film silicon solar cells: These cells use a thin layer of silicon material, resulting in lightweight and flexible panels. They are used in various applications, including building-integrated photovoltaics (BIPV).

Organic solar cells: Organic photovoltaics use organic materials like polymers and small molecules to absorb and convert sunlight into electricity. They are lightweight, flexible, and suitable for low-power applications.

Perovskite solar cells: Perovskite materials have shown tremendous potential for high-efficiency and low-cost solar cells. They are still under development but offer exciting possibilities for the future of photovoltaics.

3.7.3 Other solar cell types

Tandem solar cells: Tandem cells stack multiple layers of different materials to capture a broader spectrum of sunlight and increase efficiency. They often combine materials like silicon and perovskite.

Dye-sensitized solar cells (DSSCs): DSSCs use a dye-coated semiconductor to capture sunlight. They are cost-effective and flexible, making them suitable for portable applications.

Multi-junction solar cells: These solar cells have multiple p-n junctions stacked on top of each other, each designed to absorb a specific part of the solar spectrum. They are commonly used in concentrated photovoltaic systems.

Each type of solar cell has its advantages and limitations, with factors like efficiency, cost, and application-specific requirements influencing the choice of technology. Solar cell research continues to advance, aiming to improve efficiency, reduce costs, and expand the range of applications for clean and sustainable energy generation.

4. Unification of optics, electronics, and quantum mechanics

The unification of optics, electronics, and quantum mechanics represents a pivotal convergence in the world of science and technology. Traditionally, optics, mechanics, and electronics were separate fields, dealing with the manipulation of light, matter, and the control of electrical currents, respectively. However, in recent decades, the boundaries between these disciplines have blurred, giving rise to the field of optoelectronics.

Optoelectronic devices bridge the gap between optics and electronics by integrating light-based functionalities with electronic components and, more recently, quantum mechanical phenomena. Some notable examples include light-emitting diodes (LEDs), photodetectors, laser diodes, solar cells, optical communication systems, liquid crystal displays (LCDs), and organic light-emitting diode (OLED) displays. The emerging field of quantum optoelectronics explores the interaction between light and quantum states of matter, thereby unifying the three. It holds promise for quantum computing, quantum communication, and quantum cryptography, where photons are harnessed for advanced information processing and secure communication.

The unification of optics, quantum mechanics and electronics has not only expanded the capabilities of existing technologies but has also opened up new frontiers in research and innovation. This interdisciplinary approach continues to drive advancements in various sectors, from telecommunications and energy production to healthcare and fundamental science. As optoelectronic technologies evolve, they promise to shape the future of how we communicate, interact with the digital world, and understand the fundamental properties of light and matter.

This book is a collection of reports of such recent, though limited, advancements in the field of optoelectronics. Each chapter presents a unique solution to the research problem along with a specific technological and research objective.

Author details

Touseef Para[1,2]

1 Indian Institute of Technology Bombay, Mumbai, Maharashtra, India

2 Rechargion Energy Private Limited, Pune, Maharashtra, India

*Address all correspondence to: drtouseefpara@yahoo.com

IntechOpen

References

[1] Born M, Wolf E. Principles of Optics: Electromagnetic Theory of Propagation, Interference and Diffraction of Light. Elsevier; 2013

[2] Einstein A. Indeed, it seems to me that the observations regarding "blackbody radiation," photoluminescence, production of cathode rays by ultraviolet. Annals of Physics. 1905;**17**:132

[3] Einstein A. Generation and conversion of light with regard to a heuristic point of view. Annalen der Physik. 1905;**17**:132

[4] Latimer LH. Incandescent Electric Lighting: A Practical Description of the Edison System. D. Van Nostrand Company; 1890

[5] Atkinson ADS. Dealing with the principles and practice of fluorescent lighting, for electrical engineers, illuminating engineers and architects. Fluorescent Lighting. G. Newnes. 1946

[6] Siegman AE. Lasers. University Science Books; 1986

[7] Nakamura S, Pearton S, Fasol G. The blue laser diode. The Complete Story, Measurement Science and Technology. 2001;**12**:755

[8] Tsukada Y. Tft/lcd: Liquid-Crystal Displays Addressed by Thin-Film Transistors. CRC Press; 1996

[9] Akasaki I, Amano H, Nakamura S. Blue LEDs–Filling the World with New Light. Nobel Prize; 2014

[10] Senior JM, Jamro MY. Optical Fiber Communications: Principles and Practice. Pearson Education; 2009

[11] Fonash S. Solar Cell Device Physics. Elsevier; 2012

[12] Halme J, Vahermaa P, Miettunen K, Lund P. Device physics of dye solar cells. Advanced Materials. 2010;**22**:E210

[13] Choy WCH. Organic Solar Cells: Materials and Device Physics. Springer; 2012

[14] Green MA. Solar cells: Operating principles, technology, and system applications. Englewood Cliffs. 1982

[15] Blom PWM, Mihailetchi VD, Koster LJA, Markov DE. Device physics of polymer: Fullerene bulk heterojunction solar cells. Advanced Materials. 2007;**19**:1551

[16] Lopez-Varo P, Jiménez-Tejada JA, García-Rosell M, Ravishankar S, Garcia-Belmonte G, Bisquert J, et al. Device physics of hybrid perovskite solar cells: Theory and experiment. Advanced Energy Materials. 2018;**8**:1702772

Section 2

Research and Applications

Chapter 2

Longitudinal Assembly of Gold Nanorods on Various Templates for Optoelectronics

Puskar Chapagain and Suman Neupane

Abstract

Different synthesis methods such as lithography, physical vapor deposition, layer-by-layer deposition, self-assembly, and laser irradiation are commonly used to deposit and arrange functional nanoparticles on a substrate. The properties of these hierarchically organized materials can be fine-tuned by controlling the shape, size, and crystallinity of the fundamental building blocks. However, achieving controlled organization of the building blocks in a desired architecture on a substrate remains a formidable challenge. This topic will discuss the most recent progress in self-assembly technique and challenges in achieving linear assembly of gold nanorods on a suitable substrate in one, two, or three dimensions and their impact on photonic applications.

Keywords: self-assembly, linear array, gold nanorods, different templates, optoelectronics

1. Introduction

Gold nanorods (GNRs) are valuable materials for fundamental studies because of their stability, ease of synthesis using wet-chemical methods, controllable yield, and cost efficiency. Moreover, their shape, size, and crystallinity can be readily adjusted, allowing modification of their plasmonic properties. Consequently, GNRs are preferred for various applications such as sensors, surface-enhanced Raman spectroscopy (SERS), catalysis, and photothermal applications [1–5].

To harness the unique properties and controllable characteristics of GNRs, these particles are commonly assembled in a host material to create a hybrid material. This organization of particles on un-patterned/pre-patterned surfaces of substrates enables the modification of individual particle properties related to electronics, magnetism, and optics, opening exciting potential applications in sensors, catalysis, and biomedicine. As an illustration, consider the optical properties, such as the longitudinal surface plasmon resonance peaks, which are correlated with the local orientation of the GNRs. The axial interaction leads to a red-shift of the longitudinal plasmon resonance peak, whereas the lateral interaction leads to a blue-shift of the main plasmon band. It has been reported that the lateral orientation yields more pronounced spectral changes than the axial case [6]. Therefore, GNRs play a vital role

as key materials and building blocks in the bottom-up fabrication of new materials, shaping the future of novel optoelectronic devices [7]. These devices exploit not only the collective behavior of the ensemble but also preserve the directionality and long-range order while controlling the spacing between them. Thus, it is crucial to understand the properties of GNRs along with their interaction with the supporting material to effectively utilize and enhance the functionality of such an ordered system [8].

Various methods have been employed to generate efficient, reliable, and sustainable micro/nanodevices on predefined geometries through self-assembly [3, 9, 10], layer-by-layer [11, 12], and physical vapor deposition [13, 14]. Here, we limit ourselves to the discussion of the self-assembly technique for the organization of particles in a linear array. The self-assembly is a simple powerful technique due to its easiness, low cost, flexibility, and reproducibility. Therefore, it is considered the most promising approach for organizing particles with the desired properties into higher-order structures [10]. However, the construction of organized arrays of GNRs with tangible functionality on a desired platform presents several challenges. These challenges include the quantum size effect of GNRs, choice of the host material, arrangement of nanoparticles within the pattern, nucleation onto the platform, grain boundaries, and the coupling among the rods [8, 15, 16]. Usually, particle size, shape, and composition can be adjusted during chemical synthesis. The coupling or interparticle spacing can be addressed by selecting capping or cross-linking molecules. The rod arrangement can be controlled via assembly or guiding through a patterned surface. These steps are mutually exclusive and do not affect one another. Thus, the strength of creating hierarchically organized materials through self-assembly lies in the independence of the building blocks and assembly process [8].

As mentioned earlier, the ensemble of GNRs displays distinct properties arising from the coupling of surface plasmons, and the interaction of electric or magnetic moments among particles collectively, or through external fields. Organizing GNRs into self-assemblies shows potential applications as electrodes for light-harvesting devices, electrochemical cells, conductive platforms for plasmon-enhanced imaging, solar cells, photodetectors, and plasmonic waveguides [3, 17, 18]. The bottom-up self-assembly approach miniaturizes modern optoelectronic devices while offering an alternative to conventional top-down nanodevice fabrication. Currently, self-assembled GNR arrays are primarily used for sensing biological or chemical agents and identifying molecules through SERS. Detection of biochemical components of these sensors relies on changes in UV–Vis or photoluminescence spectroscopy of plasmon wavelength peaks [19, 20]. Limited applications exist in the area of photothermal and cancer treatments. Compared to conventional sensors, GNR-assembled sensors demonstrate enhanced selectivity, sensitivity, and improved charge dynamics. In SERS detection, the array shows several times enhancement in Raman scattering compared to discrete gold nanorods [21]. The intensity of scattering and hot spot locations (points with the highest electromagnetic field concentration) is found to be sensitive to the shape and size of the GNRs [22]. Overall, the self-assembled GNR arrays hold great promise for advancing nanotechnology and finding practical applications in fields such as sensing, molecular detection, imaging, and medical treatments.

In the following section, we begin our discussion with the common host materials used in self-assembly. We then explore the strategies for GNR self-assembly, followed by its effect on optoelectronic properties, and potential applications of such ensemble.

2. Self-assembly across various platforms

2.1 Self-assembly on glass substrates

Glass is a popular host material due to its rigidity, low cost, and abundance of exposed surface OH groups. The optical transparency of glass substrates is another major benefit. To prepare the glass surface to bind the GNRs suspended in colloids, the substrates must first be treated with an acidic solution and then rinsed in siloxane. Thus, functionalized glass introduces chemical groups that can easily tie GNRs either covalently or electrostatically. Typically, a monolayer of GNRs is deposited using this method [23]. Thiosilane is a widely used molecule that can create uniform high-quality monolayers of GNR on glass substrates [24]. Similarly, a glass substrate modified with polyanionic polymers can facilitate the end-to-end assembly of GNRs [25]. An efficient, reusable, thermal, and photochemical GNR-catalyst assembly was created on glass through electrostatic interactions by treating glass with (3-aminopropyl) trimethoxysilane and polystyrene sulfonate [26]. Additionally, the self-assembly of GNRs can be performed directly in a bulk solution or on a glass surface. Despite the high yield of GNR dimers in both cases, assembling particles directly on the substrate was reported to be more flexible in controlling the shape and size of NR within the dimer. In addition, these GNR dimers can be used to enhance two-photon-excited fluorescence signals at the single-molecule level [22]. The evaporative self-assembly of noble metal nanorods into ordered structures on glass holds great promise for fabricating optical and plasmonic devices [10]. These studies suggest that glass plays a crucial role in the fabrication of hybrid nanostructures for plasmonic nanophotonics.

2.2 Self-assembly on metal

The assembly of GNRs on metal surfaces was similar to that on glass substrates. In both cases, the surface must first be functionalized for the adsorption of GNRs. The organization of GNRs on metals has shown superior quality in optoelectrical applications. For example, the assembly of a GNR core in Zr-based metal–organic framework composites exhibited a remarkable enhancement of SERS by a factor of two and eight times higher than that of ordered bare GNR arrays and random stacking of bare GNRs, respectively [21]. The self-assembly of GNRs on a Cu substrate has shown that it is possible to create thin films of one-, two-, and three-dimensional structures. Some of the three-dimensional assemblies can be extended to the superlattices of GNRs [9].

2.3 Self-assembly on silicon (Si) wafers

Si is a common material used for fabricating micro/nanostructured devices. The self-assembly technique, which is based on convective and capillary forces, was used to create standing arrays of GNRs on lithographically predefined areas of functionalized Si wafers. The hexagonal close-packed structure of GNRs thus creates an ideal substrate for SERS [27]. A wire-like superstructure was built by evaporative self-assembly of GNRs onto a functionalized 3-mercaptopropyl trimethoxysilane Si substrate. This procedure enabled the generation of single wire-like superstructures together with double and triple repeating wire-like arrays [28]. In another report, controlled self-assembly of gold nanoarrows was achieved through the bulk solution

evaporation method on a Si wafer, resulting in nanoparticles with distinct packing and interlocking capabilities in two- and three-dimensional supercrystals. This approach enables the creation of tunable self-assembled complex superstructures on configurable architecture, offering unusual functionality for nanophotonics and metamaterials [29].

2.4 Self-assembly on carbon

The electrodeposition of gold structures onto carbon electrodes has potential applications in electrocatalysis. For instance, direct electrodeposition of Au nanostructures onto glassy carbon electrodes can be used for the non-enzymatic detection of glucose [30]. GNRs can be self-assembled into long fibers by inserting graphene quantum dots between rods, which is useful for optical properties. This is due to electrostatic interactions between the functional groups of CTAB and the amine groups of graphene [19]. Combining the plasmonic properties of self-guided GNRs with the superior electronic, chemical, and mechanical properties of single-walled carbon nanotubes (SWCNTs) creates multifunctional hybrid nanocomposites for optoelectronic applications. This was supported by drop-cast deposition of GNRs on SWCNT films/fibers, resulting in macroscopic arrays of ordered composites [17]. Layer-by-layer self-assembly of GNRs and glucose oxidase onto an SWCNT-functionalized three-dimensional sol-gel matrix for biosensor applications [31]. Similarly, the self-assembly of GNRs can form a ring-like structure on polystyrene microspheres at the fluid–fluid interface via dip coating followed by solvent evaporation [32].

Spontaneous self-assembly of GNRs functionalized with polyethylene glycol (PEG) has shown tremendous potential for bioimaging and photothermal [33]. A thermoplastic polymer mixed with a small amount of glycerol can be used as a matrix material for making GNR-composite films, which behave like a dichroic polarizer with a transmission axis perpendicular to the stretch direction [34]. The self-assembly of polymer nanocomposite films containing GNRs and poly (2-vinyl pyridine) has shown that, depending on the nanorod volume and thickness of the film, the particles are aligned side-by-side or end-to-end. This research demonstrated a strong correlation between nanoparticle dispersion and optical absorption, showing that side-by-side and end-to-end alignments induce blue and red shifts, respectively [35–37].

2.5 Self-assembly at metal/dielectric interfaces

Interface plasmons, which propagate along metal-dielectric film boundaries, have the potential to guide waves along patterned films, stripes, and nanowires. Additionally, this can enhance Raman scattering and nonlinear processes [38]. The self-assembly of polymer end-tethered GNRs into two-dimensional arrays with tilted structures has been shown to have tunable physicochemical properties. These properties are useful in photonics, electronics, plasmonics, and other applications [39].

The functionalization of GNRs with (11-mercaptoundecyl)hexa(ethylene glycol) and self-assembly using ethanol/water resulted in highly regular side-by-side arrays. This hierarchically structured material has sizes ranging from 200 nm to 10 μm and periodicities ranging from 400 nm to 20 μm. This structure has been demonstrated as a SERS sensor for biomolecule detection in water and complex biological media [12].

Incorporating octadecyltrimethoxysilane -functionalized, gold/silica (Au/SiO_2) core/shell nanospheres and nanorods into the active layer of an organic photovoltaic device increased the photoconversion efficiency [40]. Surface plasmon-enhanced

photoluminescence was also demonstrated in monolayer MoS_2 in the presence of GNRs. However, the enhancement did not increase monotonically with an increase in the metal plasmonic treatment. Instead, emissions dropped after a certain coverage [12].

Once the functionalized surface of a suitable host material is prepared, appropriate assembly methods can be selected to create highly ordered materials. In this section, we explore different methods for organizing noble metal particles.

3. Approaches to self-assemble GNRs

3.1 Drop-casting (spin-coating)

Drop-casting is a versatile, cost-effective technique that enables nanoparticles to spread on a solid substrate for an ordered structure because by precisely controlling the evaporation of droplets on hydrophobic substrates, a large-scale ordered assembly of GNRs can be achieved (**Figure 1**). Upon solvent evaporation, dispersion forces between particles and the substrate or between particles facilitate the self-organization of materials into desired mono- or multilayer structures [8]. As an illustration, hydrophobic substrates were created by spin-coating silicone oil onto glass slides followed by annealing to create the desired arrays. These arrays exhibit immense potential for SERS in rhodamine detection [41].

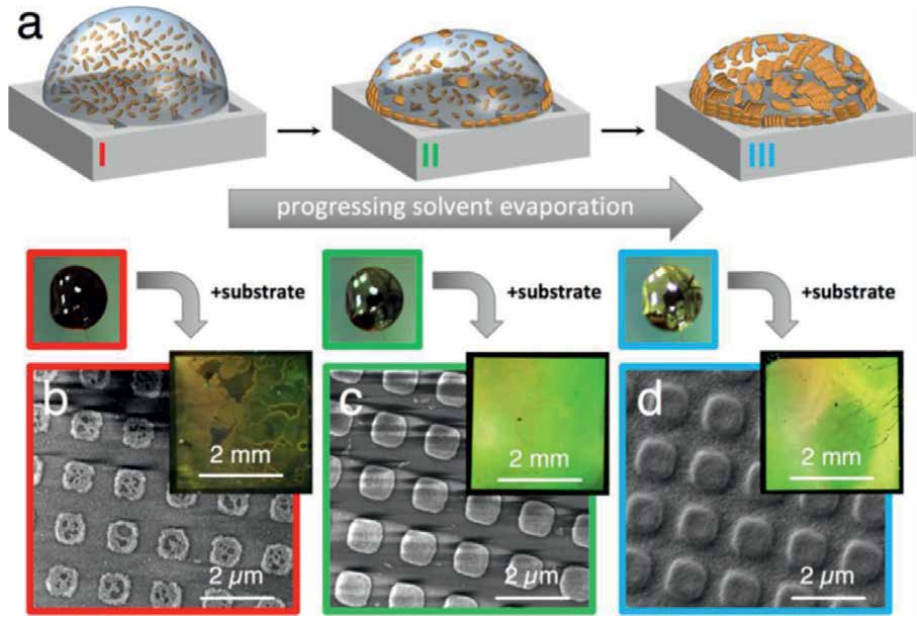

Figure 1.
Influence of pre-evaporation and correlation between droplet appearance and the resulting assembly structure. Partial evaporation of EtOH leads to the pre-assembly of the AuNRs at the liquid-air interface, causing a golden shimmer at the droplet surface due to interparticle coupling (a and inset droplet photos). For identical initial composition and volume of the dispersion, contact with the target substrate at different times leads to distinct substrate qualities (b–d). The degree of pre-assembly directly correlates with the amount of particles deposited on the structured substrate area, where the underfilled surface is marked with a red frame, the optimally prepared sample with a green frame, and a vastly overfilled array with a blue one. Reprinted with permission from Ref. [12]. Copyright @2019, American Chemical Society.

3.2 Langmuir–Blodgett technique

The Langmuir–Blodgett (LB) technique involves the self-assembly of molecules or other hydrophobic materials into an ordered monolayer at an air-water interface, followed by transferring the monolayer onto a solid substrate [42]. This method has been successful in creating highly packed two-dimensional arrays of GNRs with various structures by adjusting the surface pressure in the LB trough [34].

3.3 Cross-linking through molecules

Accurate particle linking is essential for bottom-up device fabrication, which can be achieved through molecular linkers [43]. These cross-linked molecules facilitate the formation of transport channels between individual GNRs, enabling collective optoelectronic behavior as a single entity. This technique generates not only GNR dimers but also trimers or higher-order alignments, allowing control over the shape and size of each rod in the final product [22]. Moreover, sandwiched molecules, nanoparticles, and molecules have been reported to exhibit superior charge transport. This is because of the combination of the electrical properties of nanoparticles and organic ligands, indicating the potential for large-area devices [44]. Electrical measurements conducted on connected GNRs via thiol end-capped oligophenylenevinylene solution for both before and after immersion in the solution, demonstrated a three-order-of-magnitude increase in conductance, highlighting molecular-mediated transport for nanoelectronics, and photonics [45]. GNRs synthesized by radiolysis were selectively end-functionalized by a fully conjugated thiol bearing a pendant terpyridine group; the addition of ferrous ions led to end-to-end one-dimensional self-assembly of the nanorods [46], and the linkers can create three-dimensional assemblies of covalently linked particles [47]. Varying the concentrations of these ligands can alter the organization of the group, as shown by Zhou et al. [48], who observed a change in the orientation of rods from end-to-end to side-by-side by adjusting the linker density.

3.4 External perturbation-assisted assembly

External stimuli, such as pH, temperature, light, magnetic field, and electric field, are commonly utilized to control the self-assembly of plasmonic particles. While pH, temperature, and light indirectly impact nanoparticles by primarily affecting linker molecules, electric and magnetic field-driven assembly directly influences particles through thermal gradients, magnetic dipole–dipole forces, and dielectrophoretic forces. In the case of field-guided self-assembly, surface modification is not necessary, making it easier to control GNRs. Field-driven assembly offers the potential for reversible control over particle arrangement, which may not apply in the former case [49].

3.4.1 Self-assembly by variation of pH

By changing the pH of the solution, GNRs can be self-assembled in an end-to-end fashion. Sethi et al. [50] demonstrated the self-assembly of GNRs into linear structures using cysteine. Cysteine controlled the assembly through thiol and amine attached to the tips of the individual NRs. End-to-end assemblies of nanorods were formed through cysteine mediation by varying the pH. The activity of cysteine was

highest below the pK_a value of the R-carboxylate group, preventing two-point electrostatic assemblies. No assembly of GNRs was observed at higher pH values when a zwitterionic structure was present. In another study, self-assembly of GNRs was initiated in the presence of L-cysteine molecules at a pH level of 3.1. Moreover, by blocking the assembling process with a negative layer of poly (sodium-p-styrene sulfonate) polyelectrolyte, the average number of connected GNRs could be fixed at any given moment in the solution to achieve the desired plasmonic response. The electric field between the linked nanoparticles was found to be sensitive to para-amino thiophenol. This end-to-end arrangement demonstrated an SERS application with a significantly higher enhancement factor than that of individual GNRs [51].

3.4.2 Self-assembly by laser irradiation

By irradiating a linearly polarized laser and utilizing the geometrically oriented attachment and self-assembly of GNRs single-crystalline Au nanowires can be synthesized [18] (**Figure 2**). Reinhardt et al. [52] employed laser simultaneously to reorganize and fuse GNRs to build nanowire arrays through directed assembly or self-organization on a Si-wafer. This process involves the initial creation of laser-induced periodic surface structures, followed by concomitant melting facilitated by optical heating, which promotes the formation of continuous structures, such as periodic gold nanowire arrays.

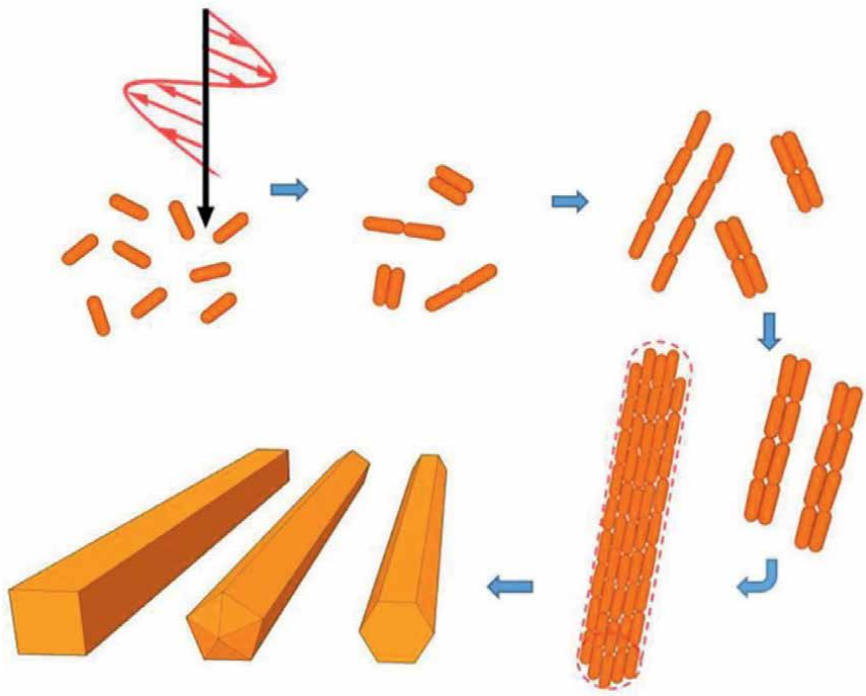

Figure 2.
A hypothesis for the plasmonic-mediated synthesis of single-crystalline Au NWs. A schematic illustration for the light-driven formation of Au NWs including the plasmonic-mediated oriented attachment of Au NRs (primary building blocks) and 3D self-assembly of the secondary, tertiary, and even higher-order building units, as well as the last stage of plasmonic heat treatment for recrystallization. Reprinted with permission from Ref. [18]. Copyright @2017, The Author(s), Spinger Nature.

3.4.3 Self-assembly by variation of temperature and humidity

Temperature is a critical factor in the self-assembly of GNRs as observed in a climate chamber. According to Liang et al. [53], the optimal temperature for achieving nematic, curved end-to-end assembly and transition mode is 30° C– 50° C on a wrinkled template. Moreover, GNRs can be molded at room temperature using Au-Si alloy as feedstock [54]. By thermal annealing the GNRs after the evaporation of the solvent and gradually increasing the temperature from 20°C to 140°C, a quasi-continuous wire-like structure was obtained [28]. Rey et al. [45] also discovered that a higher yield of linear arrays for broader impact in nano-electronics, photonics, medicine, and sensors can be attained at the optimum temperature difference between the assembly and the dew point of the solvent. Similarly, humidity also plays a role in the arrangement of GNRs. In low humidity, GNRs tend to form the nematic arrangement, while in high humidity, GNRs prefer the curved end-to-end fashion as mentioned in ref. [54].

3.4.4 Self-assembly under magnetic field

Self-assembled arrays of GNRs can be created using a magnetic field by exploiting the magnetic behavior of bare plasmonic particles or by reincorporating superparamagnetic materials. An external magnetic field must be used to manipulate or reorient the assembly. For instance, in the case of pristine GNRs, the assembly process involves partial capping with either laterally or terminally attached nematic liquid crystals. Subsequently, the incorporation of organic matter on TEM grids was performed, which caused the orientation of rods to be quasi-planar to vertical under the influence of an external magnetic field [55]. Similarly, in another study, dispersed GNRs were self-aligned through cylindrical micelle self-assembly in nematic and hexagonal liquid crystalline phases of anisotropic fluids (**Figure 3**). In this case, the external magnetic field along with shearing is responsible for the alignment and realignment of the liquid [56].

Theoretical [57] and experimental [58, 59] studies have shown that magnetic-field-assisted self-assembly of one-dimensional chains of colloidal Fe_3O_4@Au is possible for optical, photothermal, and SERS detection. The volume fraction and surface charge of plasmonic particles play a significant role in the formation and distribution of chains. As a chain forms, its absorption peak redshifts and approaches

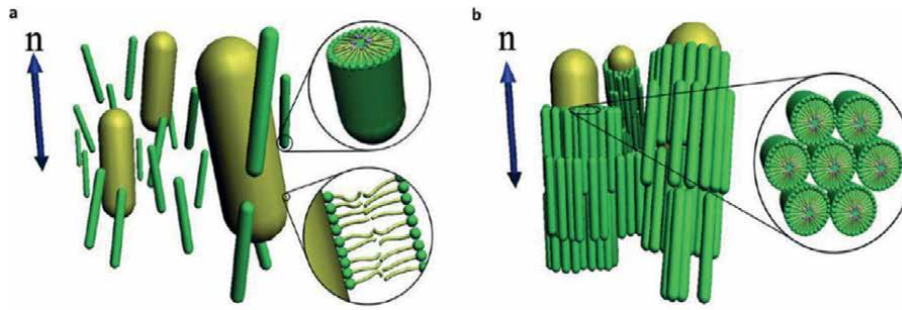

Figure 3.
(a) Schematic illustration of GNR alignment in the nematic liquid crystal (LC). (b) GNR alignment in a columnar hexagonal lyotropic LC phase. The diameter of micelles is 2–3 nm. GNRs have diameter within 15–25 nm and length of ~50 nm. Reprinted with permission from Ref. [56]. Copyright @ 2010, American Chemical Society.

that of an infinite chain, while photothermal transduction concentrates at its center. Rizvi et al. [60] demonstrated the magnetic alignment of GNRs covered with Fe_3O_4 nanoparticles carbon-coated Cu substrate and colloidal solution. The magnetic dipolar interactions among the neighboring core-shell structures give rise to magnetic anisotropy, which causes the composite material to align parallel to the applied magnetic field, thereby modifying the surface plasmon resonances. These composite materials exhibit useful magnetic properties while preserving their optical properties. The magnetic-field-induced alignment was sensitive to the core-shell size, and saturation could be achieved under a low magnetic field.

3.4.5 Self-assembly under electric field

An alternating electric-field-assisted assembly can be used to position individual nanowires suspended in a dielectric medium between two electrodes defined lithographically on a SiO_2 substrate [61]. An external electric field can control the orientation and direct the self-assembly of anisotropic Au nanoparticles into highly organized two- and three-dimensional assemblies for optical applications [62, 63]. The assembly of polystyrene-tethered AuNRs was confined and reoriented in a one-dimensional cylindrical system with the assistance of an electric field for dual applications in optoelectronics and magneto-storage [64] as shown in **Figure 4**. Droplet evaporation and application of dielectrophoretic forces have been employed

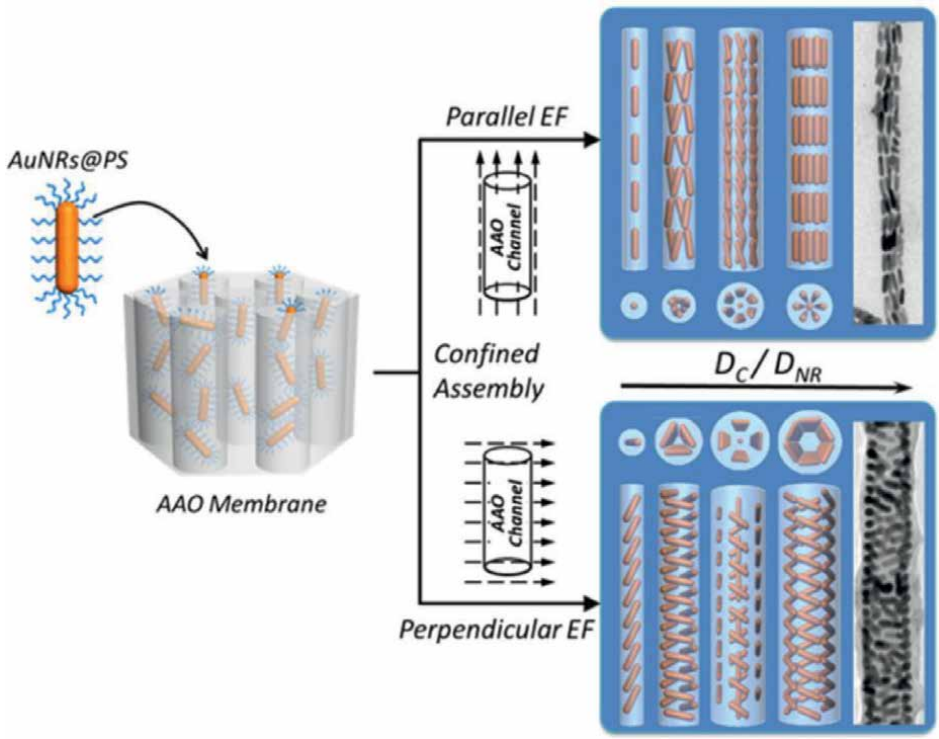

Figure 4.
Illustration showing the strategy for confined assembly of polymer-tethered AuNRs in anodic aluminum oxide Cylindrical Channel with the assistance of electric field. Reprinted with permission from Ref. [64]. Copyright @ 2016, American Chemical Society.

to self-organize GNRs into ordered arrays into end-to-end lines of one-dimensional, side-to-side fashion for two-dimensional or hexagonal arrangements for three-dimensional [65].

3.4.6 Capillary self-assembly or template-assisted self-assembly

An alternative pathway to position and orient nanoscale particles on a target substrate involves directed pathways, such as capillary or template-assisted methods, either individually or in combination. Capillary assembly involves casting a controlled drop of a colloidal solution onto a structured template to organize particles at predetermined sites. Microscopically, particles at the assembly sites experience capillary forces from the liquid-air interface. These forces apply for a moment as the contact line is pinned at the assembly site. Therefore, for successful assembly, particles must be present at the assembly site during a capillary breakup [66] (**Figure 5**). Evaporative self-assembly of noble metal nanoparticles into ordered structures by strong unidirectional microflow in the capillary of a monolayer membrane in glass cells [10]. Similarly, capillary-force-assisted self-assembly of AuNPs into highly ordered plasmonic thin films could be useful for ultrasensitive SERS [67].

In template-assisted assembly, GNRs are assembled into restructured surfaces, particularly polymers, to preserve their positions and orientations [68]. Hierarchical self-assembly of GNRs into patterned nanostructures, thereby achieving high control over supercrystal morphology and tuning the topography of the patterned substrate on the millimeter scale for SERS [69].

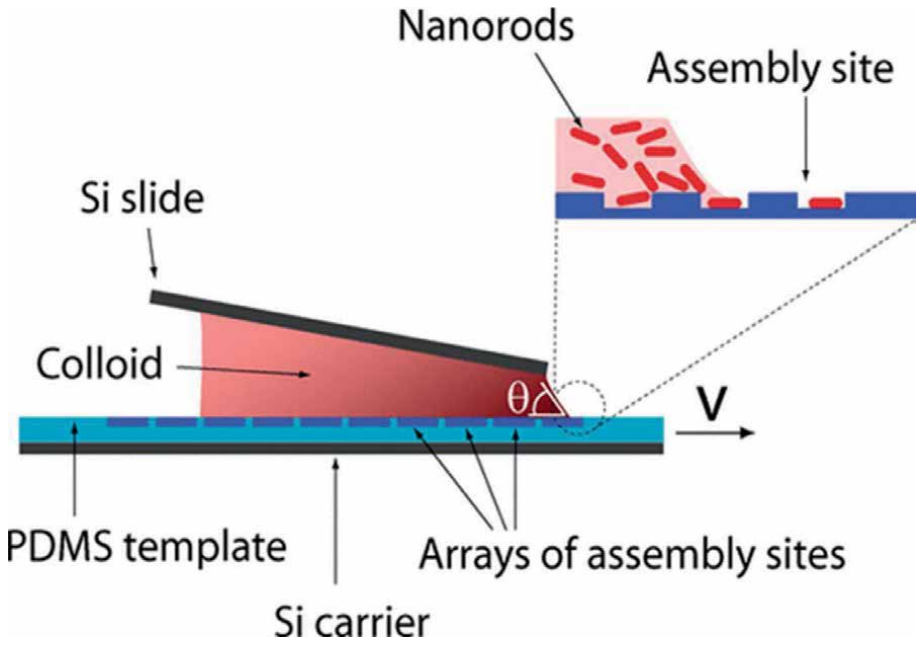

Figure 5.
Capillary assembly and experimental setup. Nanorods are assembled in holes at the three-phase contact line by capillary forces. The silicon slide and the colloidal drop are stationary while the PDMS template is moved to the right. Reprinted with permission from Ref. [66]. Copyright @ 2011, American Chemical Society.

4. Optoelectronic applications of self-assembled GNR-arrays

4.1 Sensors

The organized ensemble of GNRs has enormous potential for fabricating high-performance enzyme-based biosensors. For instance, in ref. [31], a novel amperometric glucose biosensor was fabricated using layer-by-layer self-assembly of GNRs and glucose oxidase onto SWCNTs functionalized three-dimensional sol-gel matrix. These sensors demonstrated high sensitivity, fast recovery, and response time as compared to conventional biosensors. Moreover, another study [50] showed that this assembly approach could be applied to larger biological species like peptides and proteins.

4.2 Luminescence

A localized surface plasmon of GNRs around the monolayer of MoS_2 resonates with MoS_2 gain spectrum. The spatial and spectral overlapping of the localized surface plasmon polariton and waves emitted from MoS_2 thus further enhance the light emission from the MoS_2 monolayer. This approach couples GNRs with two-dimensional nanomaterials to boost emission efficiency for future optoelectronic devices [20]. In another photoluminescence study, long fibers of GNRs self-assembled on graphene demonstrate modification of the absorption peak along with photoluminescence quenching over time. This unique arrangement of GNRs on graphene shows potential for biomedical-based nanoscale devices [19].

4.3 Electrical applications, photovoltaics and charge dynamics

Gold nanowires, formed on a Si-substrate using an electric-field assisted assembly technique, exhibit room-temperature resistivities of approximately 2.9 and 4.5×10^{-6} ohm-cm [61]. This indicates the suitability of the composite for electrical devices. Additionally, the coupling of external fields and cylindrically confined self-assembly holds promise for generating ordered hybrid assemblies with hierarchical structures. These structures have potential applications in photoelectric devices, biosensors, and data storage devices [64]. If the self-assembled GNRs are sandwiched between a double layer of alkanedithiol linkers, this could enhance conductance, as measured by current–voltage curves. The presence of GNRs offers more efficient electron transport pathways in this complex, hierarchically arranged material. Therefore, the self-assembly of gold nanoparticles can be beneficial for photovoltaic devices by controlling the charge dynamics between different layers of constituent materials [44]. Similarly in ref. [40], the incorporation of self-assembled GNRs with different aspect ratios into organic photovoltaic active layers enhances LSPR near-field absorption over a wide range of wavelengths. This adjustment has shown enhancement in photoconversion efficiency and short-circuit current of two organic photovoltaic polymer systems.

4.4 Photothermal/cancer treatment

Despite limited research on self-assembly of GNRs, the complex arrangement has demonstrated its potential for photothermal cancer treatment [33]. A self-assembled DNA origami-GNR complex has also shown promise for cancer

theranostics [70]. Additionally, self-assembled thermal GNR-loaded thermosensitive liposome-encapsulated ganoderic acid has proved effective in cancer photochemotherapy [71].

4.5 SERS

Self-organization of GNRs has significant potential in SERS. Hybrid nanostructures of plasmonic nanocrystals caged in a metal–organic framework exhibit superior SERS sensitivity [21]. The orientation of the GNRs within the arrays plays a critical role in SERS performance. For instance, vertically ordered GNR arrays show higher SERS signals than tilted arrays [39]. Moreover, the face-face stacked orientation yields larger SERS enhancements for Rhodamine 6G detection [48]. The lattice periodicity also influences molecule detection. Decreasing the lattice periodicity can enhance the signal significantly [12].

To broaden the application of SERS, controlling the chemical kinetics of droplet evaporation might be useful to alter packing arrangements while improving the mechanism behind SERS [41, 63]. Additionally, an optimum surface coverage of more than 60% ensures higher efficiency of SERS and superior accumulation of hot spots. Too much particle aggregation deteriorates SERS performance [42, 43]. The electromagnetic hot spots localized in linear assemblies of GNRs can be controlled by monitoring the pH of the assembly in the presence of L-cysteine for minutes to hours [51]. Preparation methods of the assembly could also influence SERS-based performance as in probe molecule rhodamine 6G [63, 67, 69]. Coating GNRs with magnetic materials and supplying an external magnetic field can improve the efficiency of SERS by two orders of magnitude [58].

5. Conclusion

In summary, a bottom-up approach for GNR assembly on patterned surfaces can potentially yield a highly organized, multifunctional nanostructure with tunable properties. In this chapter, we highlighted recent studies on creating GNR-ensemble to exploit their collective behavior for optoelectronic devices. Surface functionalization of rods or host materials and coupling of nanorods through physical and chemical processes are crucial for generating elegant devices. Despite progress in the self-assembly of GNRs and understanding the underlying mechanisms, large-scale production with reproducible results and controllable nanogaps between the rods remain significant challenges in this field. Furthermore, investigating solvent evaporation and drying kinetics is also essential for a better understanding of the fabrication mechanism of hierarchically arranged nanostructures [3, 72, 73]. Efforts should be made to assemble structures comprising anisotropic shapes, such as triangles, plates, stars, or multipods to explore the broader implication of the anisotropic properties of gold particles.

Acknowledgements

P.C. likes to acknowledge the financial support from the NASA EPSCoR prime award # NNX15AR71H (SAU2908 and SAU27014) to initiate the gold nanoparticles research at SAU.

Conflict of interest

The authors declare no conflict of interest.

Author details

Puskar Chapagain[1*] and Suman Neupane[2]

1 Department of Engineering and Physics, Southern Arkansas University, Magnolia, AR, USA

2 Department of Physics and Astronomy, Middle Tennessee State University, Murfreesboro, TN, USA

*Address all correspondence to: prchapagain@saumag.edu

References

[1] Wulf V, Knoch F, Speck T, Sönnichsen C. Gold Nanorods as Plasmonic sensors for particle diffusion. Journal of Physical Chemistry Letters. 2016;**7**(23):4951-4955

[2] Yu Y, Zeng P, Yang C, Gong J, Liang R, Ou Q, et al. Gold-nanorod-coated capillaries for the SERS-based detection of Thiram. ACS Applied Nano Materials. 2019;**2**(1):598-606

[3] Wei W, Bai F, Fan H. Oriented gold Nanorod arrays: Self-assembly and optoelectronic applications. Angewandte Chemie, International Edition. 2019;**58**(35):11956-11966

[4] Carabineiro SAC. Supported gold nanoparticles as catalysts for the oxidation of alcohols and alkanes. Frontier in Chemistry. 2019;**2019**:7. Available from: https://www.frontiersin.org/articles/10.3389/fchem.2019.00702

[5] Chapagain P, Guisbiers G, Kusper M, Geoffrion LD, Benamara M, Golden A, et al. Tuning the surface plasmon resonance of gold dumbbell nanorods. ACS Omega. 2021;**6**(10): 6871-6880

[6] Gluodenis M, Foss CA. The effect of mutual orientation on the spectra of metal nanoparticle rod–rod and rod–sphere pairs. The Journal of Physical Chemistry. B. 2002;**106**(37):9484-9489

[7] Daniel MC, Astruc D. Gold nanoparticles: Assembly, supramolecular chemistry, quantum-size-related properties, and applications toward biology, catalysis, and nanotechnology. Chemical Reviews. 2004;**104**(1):293-346

[8] Zabet-Khosousi A, Dhirani AA. Charge transport in nanoparticle assemblies. Chemical Reviews. 2008;**108**(10):4072-4124

[9] Nikoobakht B, Wang ZL, El-Sayed MA. Self-assembly of gold Nanorods. The Journal of Physical Chemistry. B. 2000;**104**(36):8635-8640

[10] Liu X, Chen Z, Liu Q, Sheetah GH, Sun N, Zhao P, et al. Morphological and orientational controls of self-assembly of gold Nanorods directed by evaporative microflows. ACS Applied Materials & Interfaces. 2021;**13**(44):53143-53154

[11] Takahashi H, Niidome T, Kawano T, Yamada S, Niidome Y. Surface modification of gold nanorods using layer-by-layer technique for cellular uptake. Journal of Nanoparticle Research. 2008;**10**(1):221-228

[12] Hanske C, Hill EH, Vila-Liarte D, González-Rubio G, Matricardi C, Mihi A, et al. Solvent-assisted self-assembly of gold nanorods into hierarchically organized plasmonic mesostructures. ACS Applied Materials & Interfaces. 2019;**11**(12):11763-11771

[13] Dong J, Zhao X, Gao W, Han Q, Qi J, Wang Y, et al. Nanoscale vertical arrays of gold Nanorods by self-assembly: Physical mechanism and application. Nanoscale Research Letters. 2019;**14**(1):118

[14] Cross CE, Hemminger JC, Penner RM. Physical vapor deposition of one-dimensional nanoparticle arrays on graphite: Seeding the electrodeposition of gold nanowires. Langmuir. 2007;**23**(20):10372-10379

[15] Grzelczak M, Vermant J, Furst EM, Liz-Marzán LM. Directed self-assembly

of nanoparticles. ACS Nano. 2010;**4**(7):3591-3605

[16] Bishop KJM, Wilmer CE, Soh S, Grzybowski BA. Nanoscale forces and their uses in self-assembly. Small. 2009;**5**(14):1600-1630

[17] Dan B, Wingfield TB, Evans JS, Mirri F, Pint CL, Pasquali M, et al. Templating of self-alignment patterns of anisotropic gold nanoparticles on ordered SWNT macrostructures. ACS Applied Materials & Interfaces. 2011;**3**(9):3718-3724

[18] Yu SY, Gunawan H, Tsai SW, Chen YJ, Yen TC, Liaw JW. Single-crystalline gold nanowires synthesized from light-driven oriented attachment and plasmon-mediated self-assembly of gold nanorods or nanoparticles. Scientific Reports. 2017;**7**(1):44680

[19] Bagheri P, Farivar M, Simchi A. Graphene-mediated self-assembly of gold nanorods into long fibers with controllable optical properties. Materials Letters. 2018;**224**:13-17

[20] Lee KC, Chen YH, Lin HY, Cheng CC, Chen PY, Wu TY, et al. Plasmonic gold nanorods coverage influence on enhancement of the photoluminescence of two-dimensional MoS_2 monolayer. Scientific Reports. 2015;**5**(1):1-9

[21] Li J, Liu Z, Tian D, Li B, Shao L, Lou Z. Assembly of gold nanorods functionalized by zirconium-based metal–organic frameworks for surface enhanced Raman scattering. Nanoscale. 2022;**14**(14):5561-5568

[22] Lu X, Punj D, Orrit M. Controlled synthesis of gold nanorod dimers with end-to-end configurations. RSC Advances. 2022;**12**(21):13464-13471

[23] Shipway AN, Katz E, Willner I. Nanoparticle arrays on surfaces for electronic, optical, and sensor applications. ChemPhysChem. 2000;**1**(1):18-52

[24] Weinrib H, Meiri A, Duadi H, Fixler D. Uniformly immobilizing gold nanorods on a glass substrate. Journal of Atomic and Molecular Physics. 2012;**2012**

[25] Honda K, Niidome Y, Nakashima N, Kawazumi H, Yamada S. End-to-end assemblies of gold nanorods adsorbed on a glass substrate modified with polyanion polymers. Chemistry Letters. 2006;**35**(8):854-855

[26] Harrington JA, Harms ZD, Zaleski JM. Electrostatic assembly of gold nanorods on a glass substrate for sustainable photocatalytic reduction via sodium borohydride. RSC Advances. 2016;**6**(64):59113-59123

[27] Thai T, Zheng Y, Ng SH, Mudie S, Altissimo M, Bach U. Self-assembly of vertically aligned gold Nanorod arrays on patterned substrates. Angewandte Chemie, International Edition. 2012;**51**(35):8732-8735

[28] Lestini E, Andrei C, Zerulla D. Linear self-assembly and grafting of gold nanorods into arrayed micrometer-long nanowires on a silicon wafer via a combined top-down/bottom-up approach. PLoS One. 2018;**13**(4):e0195859

[29] Wang Q, Wang Z, Li Z, Xiao J, Shan H, Fang Z, et al. Controlled growth and shape-directed self-assembly of gold nanoarrows. Science Advances. 2017;**3**(10):e1701183

[30] Shu H, Cao L, Chang G, He H, Zhang Y, He Y. Direct electrodeposition of gold nanostructures onto glassy carbon electrodes for non-enzymatic

detection of glucose. Electrochimica Acta. 2014;**132**:524-532

[31] Wu B, Hou S, Miao Z, Zhang C, Ji Y. Layer-by-layer self-assembling gold nanorods and glucose oxidase onto carbon nanotubes functionalized sol-gel matrix for an amperometric glucose biosensor. Nanomaterials. 2015;**5**(3):1544-1555

[32] Thomas N, Shivkumar S, Mani E. Self assembly of nanorods on microspheres at fluid–fluid interfaces. Physical Chemistry Chemical Physics. 2020;**22**(25):14201-14209

[33] Khan NU, Lin J, Younas MR, Liu X, Shen L. Synthesis of gold nanorods and their performance in the field of cancer cell imaging and photothermal therapy. Cancer Nanotechnology. 2021;**12**(1):20

[34] Stoenescu S, Packirisamy M, Truong VV. Improved alignment of gold Nanorods embedded in polymer films. International Journal of Theory Applied Nanotechnology. 2013;**1**(2):26-29

[35] Hore MJA, Frischknecht AL, Composto RJ. Nanorod assemblies in polymer films and their dispersion-dependent optical properties. ACS Macro Letters. 2012;**1**(1):115-121

[36] Jiang G, Hore MJA, Gam S, Composto RJ. Gold nanorods dispersed in homopolymer films: Optical properties controlled by self-assembly and percolation of nanorods. ACS Nano. 2012;**6**(2):1578-1588

[37] Hore MJA, Composto RJ. Nanorod self-assembly for tuning optical absorption. ACS Nano. 2010;**4**(11):6941-6949

[38] Maier SA, Atwater HA. Plasmonics: Localization and guiding of electromagnetic energy in metal/dielectric structures. Journal of Applied Physics. 2005;**98**(1):10

[39] Li F, Wang K, Deng N, Xu J, Yi M, Xiong B, et al. Self-assembly of polymer end-tethered gold nanorods into two-dimensional arrays with tunable tilt structures. ACS Applied Materials & Interfaces. 2021;**13**(5):6566-6574

[40] Janković V, Yang Y, You J, Dou L, Liu Y, Cheung P, et al. Active layer-incorporated, spectrally tuned Au/SiO_2 Core/Shell Nanorod-based light trapping for organic photovoltaics. ACS Nano. 2013;**7**(5):3815-3822

[41] Usman M, Ishafaq MUU, Muhammad Z, Ali W, Zhang X, Wang L. Evaporation-induced self-assembly of gold nanorods on a hydrophobic substrate for surface enhanced Raman spectroscopy applications. Frontier in Materials. 2023;**2023**:758

[42] Tim B, Błaszkiewicz P, Nowicka AB, Kotkowiak M. Optimizing SERS performance through aggregation of gold nanorods in Langmuir-Blodgett films. Applied Surface Science. 2022;**573**:151518

[43] López-Lorente ÁI. Recent developments on gold nanostructures for surface enhanced Raman spectroscopy: Particle shape, substrates and analytical applications. A review. Analytica Chimica Acta. 2021;**1168**:338474

[44] Zhou P, Qiao X, Milan D, Higgins S, Vezzoli A, Nichols R. Enhanced charge transport across molecule–nanoparticle–molecule sandwiches. Physical Chemistry Chemical Physics. 2023;**25**(10):7176-7183

[45] Rey A, Billardon G, Lörtscher E, Moth-Poulsen K, Stuhr-Hansen N, Wolf H, et al. Deterministic assembly of linear gold nanorod chains as a platform for nanoscale applications. Nanoscale. 2013;**5**(18):8680-8688

[46] Selvakannan PR, Dumas E, Dumur F, Péchoux C, Beaunier P, Etcheberry A, et al. Coordination chemistry approach for the end-to-end assembly of gold nanorods. Journal of Colloid and Interface Science. 2010;**349**(1):93-97

[47] Brust M, Schiffrin DJ, Bethell D, Kiely CJ. Novel gold-dithiol nano-networks with non-metallic electronic properties. Advanced Materials. 1995;**7**(9):795-797

[48] Zhou H, Yan H, Zhang A, Zheng L, Jia H. π–π stacking interaction induced the assembly of gold nanorods. Materials Chemistry and Physics. 2014;**148**(3):503-506

[49] Watanabe K, Kuroda K, Nagao D. External-stimuli-assisted control over assemblies of Plasmonic metals. Materials. 2018;**11**(5):794

[50] Sethi M, Joung G, Knecht MR. Linear assembly of Au Nanorods using biomimetic ligands. Langmuir. 2009;**25**(3):1572-1581

[51] Tie L, Focsan M, Bosson J, Tira C, Campu A, Vulpoi A, et al. Controlling the end-to-end assembly of gold nanorods to enhance the plasmonic response in near infrared. Material Research Express. 2019;**6**(9):095038

[52] Reinhardt HM, Bücker K, Hampp NA. Directed assembly of gold nanowires on silicon via reorganization and simultaneous fusion of randomly distributed gold nanoparticles. Optics Express. 2015;**23**(9):11965

[53] Liang Y, Xie Y, Zhu Z, Ji Y, Wu X, Liu Q. Self-assembly of gold nanorods on wrinkled template. Nano. 2014;**09**(07):1450076

[54] Raj A, Liu N, Liu G, Sohn S, Xiang J, Liu Z, et al. Nanomolding of gold and gold–silicon heterostructures at room temperature. ACS Nano. 2021;**15**(9):14275-14284

[55] Umadevi S, Feng X, Hegmann T. Large area self-assembly of Nematic liquid-crystal-functionalized gold nanorods. Advanced Functional Materials. 2013;**23**(11):1393-1403

[56] Liu Q, Cui Y, Gardner D, Li X, He S, Smalyukh II. Self-alignment of plasmonic gold nanorods in reconfigurable anisotropic fluids for tunable bulk metamaterial applications. Nano Letters. 2010;**10**(4):1347-1353

[57] Xue X, Liu K, Furlani EP. Theoretical study of the self-assembly and optical properties of 1D chains of magnetic–plasmonic nanoparticles. Journal of Physical Chemistry C. 2017;**121**(17):9489-9496

[58] Hu F, Lin H, Zhang Z, Liao F, Shao M, Lifshitz Y, et al. Smart liquid SERS substrates based on Fe_3O_4/Au nanoparticles with reversibly tunable enhancement factor for practical quantitative detection. Scientific Reports. 2014;**4**:7204

[59] Porta AL, Sánchez-Iglesias A, Altantzis T, Bals S, Grzelczak M, Liz-Marzán LM. Multifunctional self-assembled composite colloids and their application to SERS detection. Nanoscale. 2015;**7**(23):10377-10381

[60] Rizvi MH, Wang R, Schubert J, Crumpler WD, Rossner C, Oldenburg AL, et al. Magnetic alignment for Plasmonic control of gold Nanorods coated with Iron oxide nanoparticles. Advanced Materials. 2022;**34**(40):2203366

[61] Smith PA, Nordquist CD, Jackson TN, Mayer TS, Martin BR, Mbindyo J, et al. Electric-field assisted

assembly and alignment of metallic nanowires. Applied Physics Letters. 2000;**77**(9):1399-1401

[62] Vutukuri HR, Badaire S, de Winter DAM, Imhof A, van Blaaderen A. Directed self-assembly of micron-sized gold nanoplatelets into oriented flexible stacks with tunable interplate distance. Nano Letters. 2015;**15**(8):5617-5623

[63] Dong J, Yuan J, Cao Y, Zhao Y, Han Q, Gao W, et al. Electrically controllable self-assembly of gold nanorods into a plasmonic nanostructure for highly efficiency SERS. Optics Letters. 2022;**47**(24):6365-6368

[64] Wang K, Jin SM, Xu J, Liang R, Shezad K, Xue Z, et al. Electric-field-assisted assembly of polymer-tethered gold nanorods in cylindrical nanopores. ACS Nano. 2016;**10**(5):4954-4960

[65] Martin A, Schopf C, Pescaglini A, O'Riordan A, Iacopino D. Synthesis, optical properties and self-assembly of gold nanorods. Journal of Experimental Nanoscience. 2012;**7**(6):688-702

[66] Kuemin C, Stutz R, Spencer ND, Wolf H. Precise placement of gold Nanorods by capillary assembly. Langmuir. 2011;**27**(10):6305-6310

[67] Dong J, Wu H, Cao Y, Yuan J, Han Q, Gao W, et al. Capillary-force-assisted self-assembly of gold nanoparticles into highly ordered plasmonic thin films for ultrasensitive SERS. Physical Chemistry Chemical Physics. 2023;**25**(3):1649-1658

[68] Holzner F, Kuemin C, Paul P, Hedrick JL, Wolf H, Spencer ND, et al. Directed placement of gold Nanorods using a removable template for guided assembly. Nano Letters. 2011;**11**(9):3957-3962

[69] Hamon C, Novikov S, Scarabelli L, Basabe-Desmonts L, Liz-Marzán LM. Hierarchical self-assembly of gold nanoparticles into patterned Plasmonic nanostructures. ACS Nano. 2014;**8**(10):10694-10703

[70] Jiang Q, Shi Y, Zhang Q, Li N, Zhan P, Song L, et al. A self-assembled DNA origami-gold nanorod complex for cancer theranostics. Small. 2015;**11**(38):5134-5141

[71] Zhang W, Yu W, Ding X, Yin C, Yan J, Yang E, et al. Self-assembled thermal gold nanorod-loaded thermosensitive liposome-encapsulated ganoderic acid for antibacterial and cancer photochemotherapy. Artificial Cells, Nanomedicine, and Biotechnology. 2019;**47**(1):406-419

[72] Nie Z, Petukhova A, Kumacheva E. Properties and emerging applications of self-assembled structures made from inorganic nanoparticles. Nature Nanotechnology. 2010;**5**(1):15-25

[73] Ramasamy K, Gupta A. Routes to self-assembly of nanorods. Journal of Materials Research. 2013;**28**(13):1761-1776

Chapter 3

Optoelectronic Devices for Quantum Information Processing

Hai-Zhi Song, Qiang Zhou, Guangwei Deng, Qian Dai, Zichang Zhang and You Wang

Abstract

The recent developments of optoelectronics do promote the progress in many other fields. For quantum information processing, we made efforts in manufacturing quantum devices by using optoelectronic techniques. We designed quantum dot embedded nanocavities to serve as efficient quantum emitters; using spectral multiplexing technique, we fabricated a heralded single-photon source, emitting highly pure and speedy single photons; and defects in GaN were observed serving as room temperature quantum random number generators. An entangled photon emitter with visibility of 97% was developed using cascaded second-order nonlinear optical process in PPLN waveguides; and Si_3N_4 microrings were effectively applied to establish photon entanglers. Readout circuits were optimized to fabricate specific single-photon avalanche detectors, and telecomm-band single-photon avalanche detectors have been improved to 128 × 32 arrays for quantum imaging. A multiplexed quantum memory was explored to simultaneously store 1650 single photons. Opto-electro-mechanical devices were studied or fabricated in order to measure minor quantities in quantum level. These works may shed light on quantum information technology for the future.

Keywords: optoelectronics, device, quantum information, single photon, entanglement

1. Introduction

Quantum information science has now attracted significant attention, since it has been well proved and is believed to support quantum computation, quantum communication, and quantum metrology in the near future by using unique quantum mechanical characteristics [1]. Characteristics of quantum states have opened the opportunities to accomplish tasks beyond classical limits, resulting in a frontier field of quantum technologies [2–8]. Among them, quantum computation technology can accelerate the speed of computers exponentially with respect to the classical machine, quantum communication technology guarantees completely secure communication [9–14], and quantum measurement technology can greatly optimize the sensitivity and/or resolution of many instruments [15–18]. These potential accomplishments have led to the development of innovative and advanced applications in various sectors such as the military, communication, and therefore, people are presently

struggling to construct efficient quantum information systems and quantum networks [10, 19–23].

To realize practical quantum information systems and quantum networks, fundamental devices must be firstly well developed. The successful fabrication of superconductor quantum circuit chips led to an achievement of constructing quantum computer of 127 qubits [24]. Realization of more general quantum computers needs much larger scaled, more robust, more quantum logic circuit chip consisting of probably superconductors [25], cold atoms [26], semiconductors [27], photonic crystals [28], etc. The primary obstacles in establishing a quantum network involve the distribution of entangled qubits among nodes that are physically distant from each other, which need high-performance entangled photon source and quantum memory [29]. Among various types of quantum devices, optoelectronic devices play a key and central role, since the advanced microelectronic, optical, and optoelectronic platforms enable fabricating the building blocks for most of the quantum information processing systems [30]. Technologies based on optoelectronics have the potential to realize a complete product chain in the field of quantum information [31, 32].

Materials with optoelectronic properties for quantum information applications encompass crystals exhibiting optical nonlinearity [33], semiconductors with wideband characteristics [34], semiconductor quantum dots [35], optical fibers, photonic crystals, diamonds, 2D materials [36], perovskites [37], metamaterials [38], topologic insulators, etc. These materials have been utilized in the development of various quantum devices such as circuits, emitters, detectors, memories, repeaters, channels [33–38], but further developments are still strongly required, for example, to improve the scalability of quantum information networks. To face up with the coming challenges, we need first look back what we have really resolved and probably see how we can step forward.

In this chapter, the optoelectronic devices we manufactured for quantum information processing will be reviewed. Our works on single-photon emitters, entangled photon sources, single-photon detectors, and other devices will be described in sections 2, 3, 4, and 5, respectively. At the same time, we also discuss some demonstrations and applications using these devices. We hope this review is helpful for the realization of quantum information network in the future.

2. Single-photon emitters

Single-photon emitters refer to light sources that release light in the form of individual particles or photons. Single-photon emitters are the fundamental devices for quantum communication. They are also well used in quantum detection and photonic quantum computation. In this direction, we have studied single-photon emitters based on quantum dot [32, 39–42], heralded single-photon sources [43], identity of single photon [44], and a quantum random number generator [45].

2.1 Quantum dot single-photon emitters

Most of the single-photon emitters in use are probabilistic devices [46], which are not well satisfying the sophisticated requirements of quantum information system. Semiconductor quantum dots (QDs) are tiny particles, typically a few nanometers in size, which exhibit distinct optical and electronic characteristics due to the principles of quantum mechanics. QDs are believed to be ideal candidate for on-demand,

deterministic single photon emitters, so materials containing QDs were deeply investigated to pursue quantum emitters based on QDs, for which we have a review paper [47]. Early in 2005, we participated in the work from Ref. [43], where remarkable photon antibunching was obtained from the InAlAs single QD, and its further strengthened single-photon generation was demonstrated [39]. These devices were designed to match the visible light range of the highly efficient Si single-photon detectors, but higher requirements lie in the telecommunication bands. For the application in optical fiber-based quantum communication, we have fabricated InAs/InP quantum dot single-photon emitter and achieved the highest single-photon purity (~10^{-3}) [40]. This source has been applied in a conventional system of quantum key distribution and effectively practiced secure key transmitting over 50 km of commercial fiber. These single photo-emitters, however, were subject to low-emitting rates, which is hindering its application in quantum communication. Using the cavity Purcell effect to modulate the QD lifetime, we designed Si/SiO_2 distributed Bragg reflectors (DBR)-based micropillar cavities in hybrid with InP-based semiconductors for weak [48] and strong coupling (with tapered DBR) [49] of telecom-band photons with QDs to achieve highly efficient, indistinguishable, and even coherent single-photon emitters.

Considering the difficulty in hybrid processing, we then designed monolithic micropillar InP-based single-photon emitters [41, 50, 51]. In these works, new designs for pillar cavities operating at a wavelength of 1.55 μm were proposed and investigated. These structures consist of layers made from InP, air apertures, and InGaAsP materials. It has been verified that these structures can be manufactured using a single-integrated process. By incorporating air apertures and tapered DBRs, it is possible to achieve a high-quality factor ranging from 10^4 to 10^5 at the desired wavelength of 1.55 μm.

The diagram of the proposed cavity is schematically demonstrated in **Figure 1(a)**. **Figure 1(b)** displays the instances of the computed optical mode spectra accompanied by corresponding DBR optical bands. This nanocavity exhibits potential as a promising option for QD single-photon sources in the 1.55-μm telecom band, owing

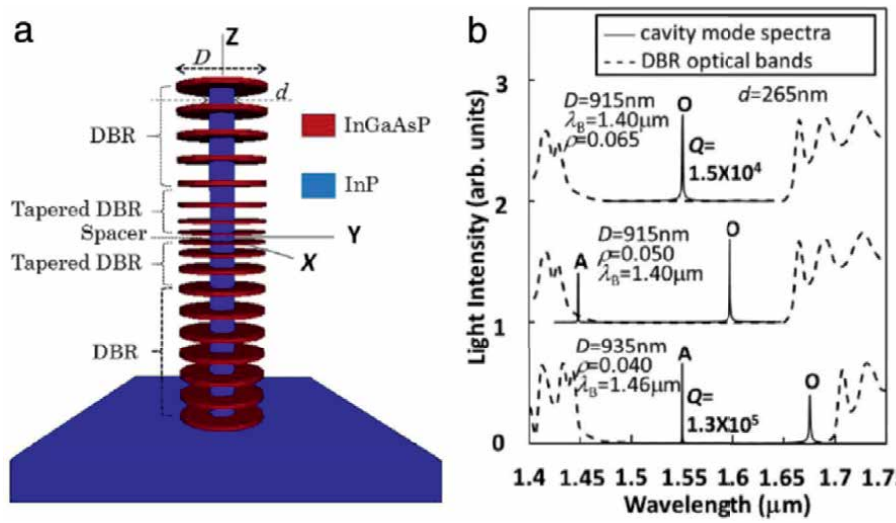

Figure 1.
(a) A visual representation of the proposed cavity in three dimensions. (b) Optical mode spectra and corresponding DBR optical bands were calculated, with vertical shifts applied to lines representing different design conditions for clarity. From ref. [41] (reused with approved CC BY license).

to its capability to achieve both weak coupling and strong coupling between a single semiconductor QD and an optical cavity mode. The above cavity design using adiabatic tapering technique was later extended to a general method, by which one can realize different types of highly efficient quantum emitters [52, 53].

Based on these proposals, we further studied their possible advancements to achieve high experimental availability [42, 54]. The impact of fabrication tolerance on the InGaAsP/InP-air-aperture micro–/nano-pillar cavity was investigated in our work. A finite-difference time-domain method was employed to simulate the effects of fabrication imperfections, encompassing uncertainties in layer thickness, material diameter, surface and interface roughness, and distortion of the cavity shape. The results indicated the cavity quality was robust to the imperfection of the fabrication processing. The cavity quality remained sufficiently high to create highly efficient and coherent single-photon sources at a wavelength of 1.55 μm, even with thickness errors within the range of ±2 nm, diameter uncertainties within ±2%, surface roughness variations up to ±2.5 nm, and sidewall inclinations of 0.5°. Consequently, an InGaAsP/InP-air-aperture micropillar cavity containing quantum dots shows promising potential as a realizable choice for single-photon emitters in quantum information networks based on silica fibers.

2.2 Heralded single-photon source

The above QD single-photon emitters are currently not practical enough yet, so people have to seek more useful candidates for on-demand single-photon emission. Heralded single-photon source (HSPS) represents such efforts. Although still probabilistic, it can partially approach the deterministic character. It is based on correlated photon pairs, in which one photon (the heralding photon) is detected and the existence of the other photon (the heralded photon) can be indicated. The generation of correlated photon pairs can be realized through the processes of spontaneous parametric down-conversion (SPDC) or spontaneous four-wave mixing. Besides the nearly deterministic property, such HSPSs have the advantages of convenient demonstration, flexible emission wavelength, and high indistinguishability. Lithium niobate is the most advanced material for optoelectronic and optical quantum devices, for which we have a review paper [55]. In Ref. [43], we have proposed a 1.5 μm chip-scale HSPS made of lithium niobate on insulator (LNOI) by utilizing spectrum multiplexing and active feedforward spectrum processing technology, as shown in **Figure 2**.

Furthermore, we have successfully demonstrated a preliminary experiment using discrete fiber-based elements, as depicted in **Figure 3**. The broadband correlated

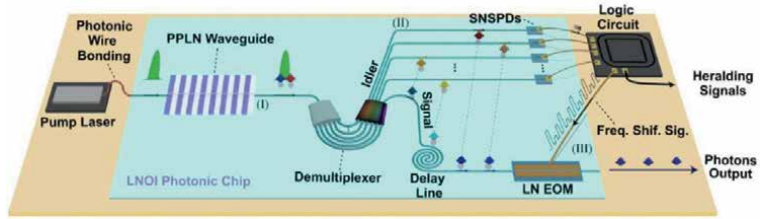

Figure 2.
A view on the future chip-scale spectrally multiplexed HSPS using LNOI technology, where a single photonic chip integrates all essential components including modules of a pump laser, a photon-pairs generator, a filter and detector, and a feedforward and frequency shifter. From ref. [43] (reuse with approved CC BY license).

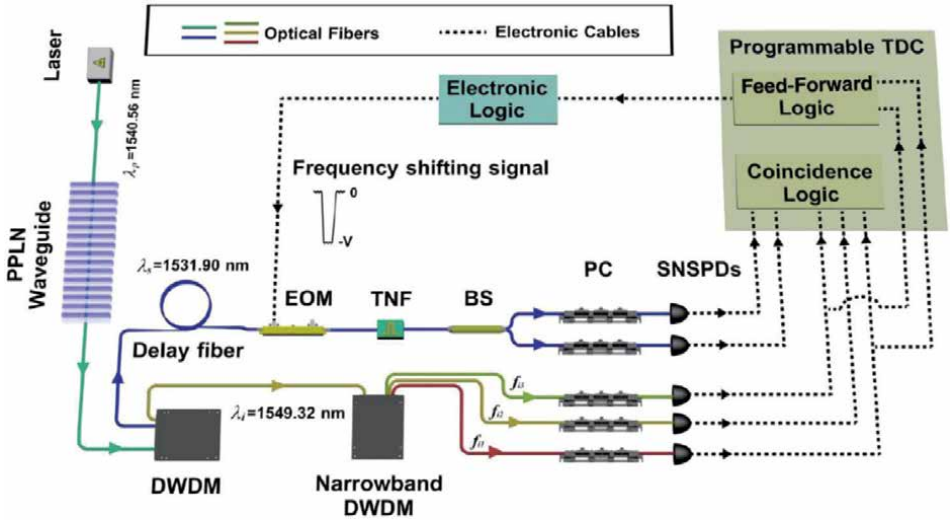

Figure 3.
Experimental setup for spectrally multiplexed HSPS. From ref. [43] (reuse with approved CC BY license).

photon pairs were generated within a fiber-connected periodically polarized lithium niobate (PPLN) waveguide. Next, the dense wavelength-division multiplexers (DWDMs) were utilized to segregate the signal photons and heralding photons, which had a bandwidth of approximately 100 GHz. The heralding photons from three paths were individually detected by three superconductor nanowire single-photon detectors (SNSPDs).

As a result, the detecting events of those photons were directed to the feedforward logic where every detecting event activates the logic circuit, causing electronic devices emit an associated frequency-shifting signal to the electro-optical modulator (EOM). The signal photons underwent a delay through a fiber loop in order to synchronize their timing with the electronic frequency shifting signal. Subsequently, the signal photons experienced frequency shifting and were combined into a shared spectral mode. Ultimately, an exceptionally low second-order correlation index $g^2(0)$ of 0.0006 ± 0.0001 was achieved at a tested single-photon emitting rate of 3.1 kHz, indicating that spectral multiplexing has enhanced the heralded single-photon rate by nearly threefold. Moreover, by implementing Hong–Ou–Mandel (HOM) interference between these spectra-multiplexing single photons and photons from independent and weakly coherent sources, it was demonstrated that the indistinguishability of multiplexed single photons after spectrum manipulation is ensured. This research opens up possibilities for scalable and highly performing HSPS on-chip with spectral multiplexing toward deterministic single-photon emitters.

2.3 The identity of single photons

For quantum information processing, for example, quantum teleportation and quantum key distribution, the issue of indistinguishability between wave packets of individual photons has been emphasized. At present, the indistinguishability of single photons has been characterized from different perspectives, such as space, time, polarization, frequency, and orbital angular momentum. From Ref. [44], we have specifically studied the evolution law of photon identity from the perspective of

dispersion through the HOM interference. In this work, a theoretical analysis model of photon identity from the perspective of dispersion was established based on HOM interference. We initially generated two wave packets with weakly coherent single photons by attenuating pulses from a mode-locked laser and subsequently manipulated them in a dispersive manner prior to their interference. The outcome demonstrated that the second-order dispersion related disparity between the two optical paths of the HOM interferometer can be correlated with the interference pattern. When both paths experienced an equal amount of dispersion, the pattern was determined by the inherent indistinguishability of the wave packets. Conversely, if there was an imbalance in dispersion between the paths, it would broaden the interference pattern and diminish its visibility. This study offers a more comprehensive comprehension of single-photon wave packets and explores potential applications of HOM interference in quantum information processing based on single photons.

2.4 Application: Quantum random number generator

Random numbers have a widely application in field of quantum information processing. Among the different types of random number generators, quantum random number generators (QRNGs) can generate true and unpredictable random numbers by utilizing inherent randomness in a system based on quantum mechanics.

Firstly, we have successfully demonstrated the single-photon emission at room temperature from a single defect in a GaN layer grown on a patterned sapphire substrate [45]. This emission exhibited a rate of 2 MHz and an auto-correlation value of 0.36 ± 0.01. Additionally, we have conducted an experimental validation of a real-time quantum random number generator utilizing the aforementioned single-photon emitter, as depicted in **Figure 4**. The excitation of the single emitter was achieved using a continuous wave laser with a wavelength of 532 nm. By employing a dichroic mirror (DM) with its cutoff wavelength set at 560 nm, the laser beam was reflected and focused onto the GaN wafer through an objective lens with numerical aperture (NA) equal to 0.9. Subsequently, the obtained luminescence resulting from this process was collected by the objective lens as above configured in confocal mode before being directed toward our detection system *via* the dichroic mirror. Consequently, we were able to achieve an initial raw bit generation rate approximately equal to 1.8 MHz while obtaining an unbiased bit generation rate around 420 kHz following von

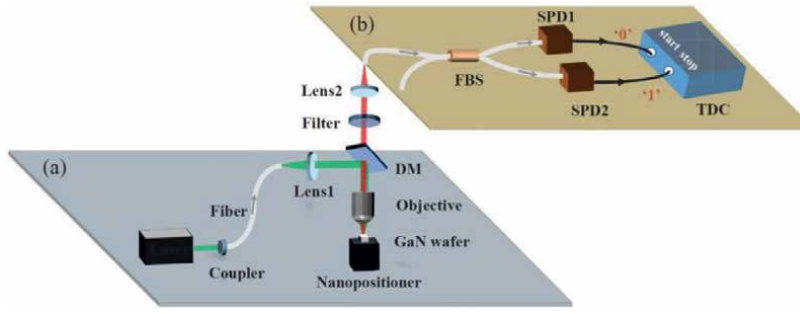

Figure 4.
Scheme of a random bit generator with branching paths. (a) the experimental setup, which involved a self-made confocal scanning microscope to stimulate the single-photon emission in the GaN wafer and capture the luminescence from individual photons. (b) the HBT configuration, employed to assess the purity of single photons emitted and generate binary random numbers. From ref. [45] (reuse with approved CC BY license).

Neumann's randomness extraction procedure. To further enhance photon count rates within our QRNG setup, it is possible to improve collection efficiency by optimizing free space optics for capturing emitted light—an area that still holds significant untapped potential for improvement within this framework. This study effectively demonstrates how commercially available GaN wafers possess immense promise for advancing integrated devices capable of emitting single photons and facilitating high-speed quantum random number generation processes.

3. Entangled photon sources

Quantum entanglement is a phenomenon that arises when a collection of particles is created, interact, or exist in close proximity to each other in such a manner that the individual quantum states of each particle cannot be figured out independently from the states of the others, even if these particles are widely separated. As a fundamental resource, quantum entangled light sources are widely used in quantum information processing [56–58]. We have made a comprehensive study on the theory [59], performance improvement [60, 61], integration [62, 63], and application [64–66] of entangled photon sources.

3.1 Theoretical study on entangled photon sources

Entangled photons with a wider wavelength range are conducive to expanding their application scenarios in quantum information processing. However, typical materials for the preparation of spectrally uncorrelated entangled photon pairs are limited to a few nonlinear crystals, making the range of photon wavelengths not as wide as ideal. To explore new schemes for obtaining a wider wavelength range, we have theoretically studied the spectrally uncorrelated entangled photon pairs produced by 15 isomorphs of potassium dihydrogen phosphate (KDP) crystal [59]. The results show that eight crystals in the "KDP family" have nonlinear optical properties similar to KDP and have the ability to generate spectrally uncorrelated entangled photon pairs within a wavelength range of ~300 nm (i.e., 792 ~ 1092 nm) according to the group velocity matching condition. Furthermore, we have investigated the preparation of heralded pure-state single photon with a purity of 0.97; namely, the output of one single photon was herald from the detection signal of another photon in the photon pair. The HOM interference between photons from independent emitters also achieved a visibility around 97%. The work expands the preparation of entangled photon pairs as well as heralded pure-state single photons with a wider wavelength range in the near-infrared band.

3.2 Performance improvement of entangled photon sources

Acting as information carriers, photons can be entangled in various degrees of freedom, such as polarization, frequency-bin, time-energy, orbital angular momentum, time-bin. To obtain high-performance discrete frequency-bin entangled photon pairs, we have proposed and demonstrated a scheme consisting of a modified Sagnac interferometer by using a single piece of PPLN waveguide [60]. The correlated two-photon states were prepared in different directions of a Sagnac interferometer based on cascaded SHG/SPDC processes. The output two-photon states could be manipulated by introducing the relative phase difference between two transmission paths

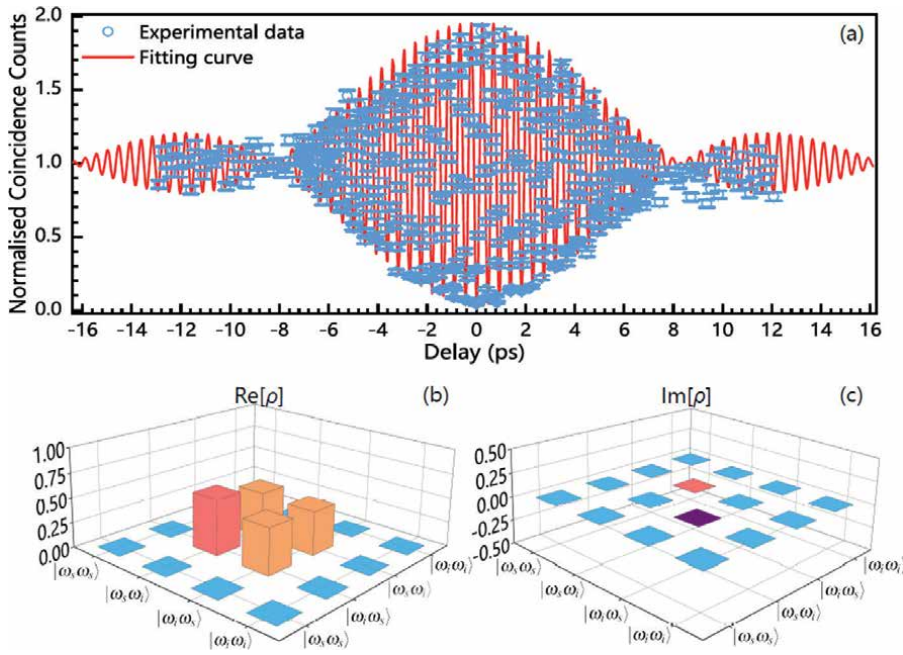

Figure 5.
The photon pair performance of frequency-bin entangled sources. (a) the spatial quantum beating; (b) the real part; and (c) the imaginary part of the density matrices, respectively. From ref. [60] (reuse with approved CC BY license).

with the change of polarization state of pump laser. Then, the discrete frequency-bin entangled photon pairs were obtained by using a fiber polarization splitter without post-selection. The performance of frequency-bin entangled photon-pairs is shown in **Figure 5**. The prepared frequency-bin entanglement achieved a fidelity of 98.0 ± 3.0% based on the visibility of spatial quantum beating of 96.0 ± 6.1%. It provides a practical frequency entangled photon source compatible with the modern telecommunication for quantum information processing.

The practicality of entangled photon sources limits their application in quantum information processing. To obtain entangled photon pairs with high performance, we have proposed a scheme of fiber-integrated PPLN waveguide module that consists of a PPLN waveguide and two noise-rejecting filters [61]. **Figure 6** shows the structure of the module and the measured spectra of correlated photon pairs and Raman photons from the module. The correlated photon pairs were prepared by cascade SHG/SPDC processes in a PPLN waveguide of a single piece. As a result, the coincidence-to-accidental ratio (CAR) of photon pairs achieved a maximum value of 52,600, and the generation rate and detection rate were 52.36 kHz and 3.51 kHz, respectively. It was actually improved for nearly one order of magnitude with respect to the previous reports.

Based on the coherently superposition of correlated photon pairs, we have further prepared energy-time, time-bin, and frequency-bin entangled photon pairs to cope with different application scenarios, respectively, as shown in **Figure 7**. The visibility of the two-photon interference of the energy-time entangled photon pair was 95.74 ± 0.86%, and the maximum S = 2.71 ± 0.02 of the Clauser–Horne–Shimony–Holt (CHSH)-Bell inequality could be calculated. The fidelity of the frequency-bin entangled photon pairs was measured to be 97.56 ± 1.79%, while the visibility of the

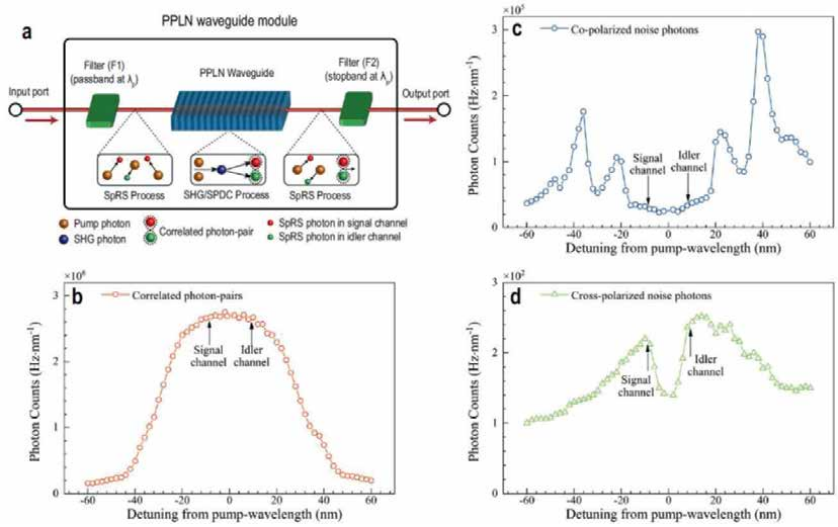

Figure 6.
(a) The structure of the PPLN waveguide module. (b) the spectra of correlated photon pairs generated from the module. (c), (d) the spectra of co- and cross-polarized Raman photons from the module. From ref. [61] (reuse with approved CC BY license).

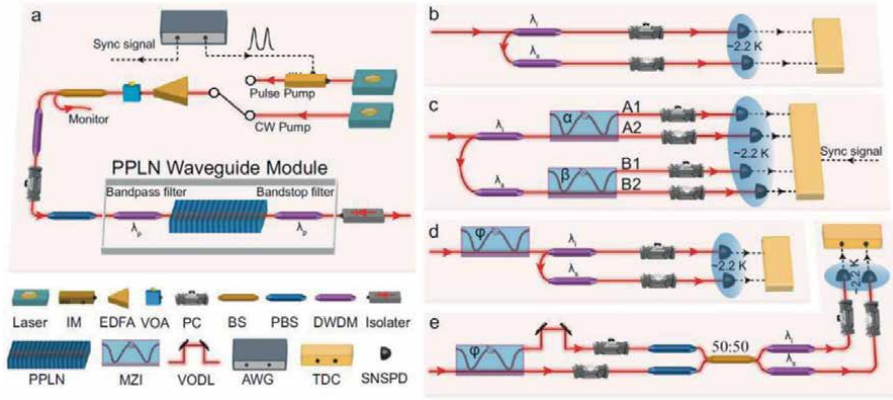

Figure 7.
Experimental setups. (a) Generation of correlated photon pairs. (b) Characterization of correlated photon pairs. (c) Characterization of energy-time and time-bin entangled photon pairs. (d) Coherently manipulation of energy-time entangled photon pairs. (e) Generation and characterization of frequency-bin entangled photon pairs. From ref. [61] (reuse with approved CC BY license).

spatial quantum beating reached 96.85 ± 2.46%. Quantum tomography revealed fidelity of 89.07 ± 4.35% for the time-bin entangled photon pairs. Our results provide a high-performance entangled photon source in quantum information processing, which can cope with various application scenarios.

3.3 Efforts on chip-level entangled photon sources

As is well known, in order to realize highly-performing quantum information processing, the development of thoroughly integrated photonic chips based on

various materials and schemes has become an inevitable tendency. We have investigated the generation of multi-wavelength correlated photon pairs *via* silicon nitride (Si_3N_4) micro-ring resonator (MRR) [62]. The single-photon spectrum in the range of 1480–1620 nm was shown. Furthermore, the dependence of core parameters, such as CAR, generation rate, and the collection efficiency, on pump laser powers, were completely demonstrated.

In addition, we have experimentally demonstrated a multi-wavelength quantum light source with a Si_3N_4 MRR [63]. The device design and characterization are shown in **Figure 8**. The optimized over-coupling Si_3N_4 MRR was designed and fabricated with the free spectral range around 200 GHz and the quality-factor about 1.0×10^6. The generation of eight high-quality correlated photon pairs with high photon generation rate, CAR, and single-photon purity was achieved by the natural resonance characteristics. With device optimization and noise-rejecting filters, we further prepared heralded single photons and energy-time entanglement for each wavelength pair. The results show a second-order auto-correlation value of $g_h^0(0) = 0.014 \pm 0.001$ at a rate of 62 kHz and a Franson interference visibility of 99.39 ± 0.45%, respectively. This multi-wavelength quantum light source represents a potential candidate for the developing of quantum information processing in an integrated platform [33].

3.4 Application of entangle photon sources

Based on the previous works on high-performance entangled photon pair, we have explored their application in quantum information processing including quantum teleportation [64, 65] and quantum key distribution (QKD).

Quantum teleportation is one of the methods of quantum communication, which could transfer an unknown quantum state between two remote nodes *via* quantum entangled photon pairs and Bell-state measurement (BSM). By utilizing the mentioned entangled photon pair source [61], we have experimentally demonstrated quantum teleportation based on 40-km-long fiber spool, and the results showed that the transmission rate and fidelity were 6.41 ± 0.37 Hz and 87.70 ± 5.75%, respectively [64].

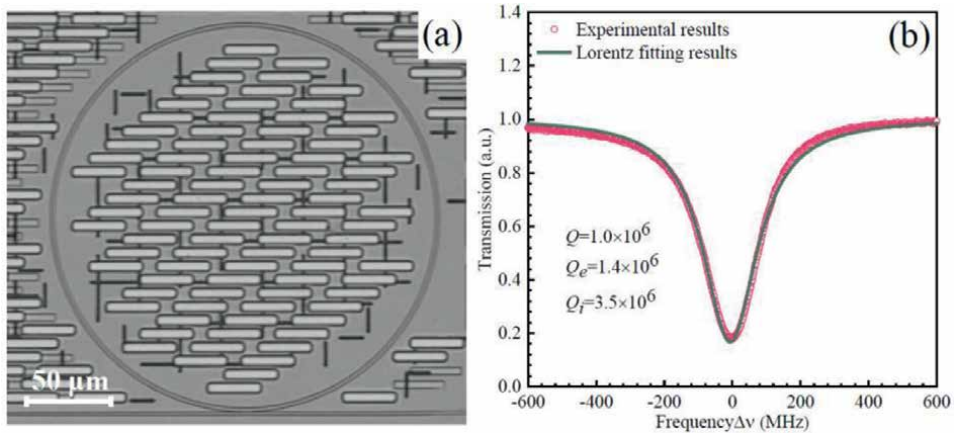

Figure 8.
Device design and characterization for Si_3N_4 micro-ring entangled photon source. (a) Microscopy image of the silicon nitride micro-ring with a thickness of 0.8 μm, width of 1.8 μm, radius of 113 μm, and gap width of 0.35 μm. (b) Resonance dip at 1540.5 nm, with a $Q = 1.0 \times 10^6$, $Q_e = 1.4 \times 10^6$, and $Q_i = 3.5 \times 10^6$. [63].

Based on the experience of previous experiment in the lab, we have further implemented the quantum teleportation system *via* campus backbone network [65]. In this scheme, a three-node quantum teleportation system was established in the University of Electronic Science and Technology of China (UESTC) campus. The three-node quantum teleportation system is shown in **Figure 9**. Alice prepared the single-photon quantum state that carries relevant information. Then, the single-photon quantum state transmitted to Charlie *via* a quantum channel. Bob prepared a pair of entangled photons and transmitted one of them, called the idler photon, to Charlie through another quantum channel. Subsequently, Charlie conducted a joint Bell State Measurement (BSM) on the photons from Alice and Bob, and communicated the outcome to Bob using a classical channel. Finally, Bob successfully retrieved the single-photon quantum state from Alice by applying a unitary transformation on the signal photon.

The characteristics of the system relied on a high-performance time-bin entangled photon source mentioned before [61]. In our system, we also have built a real-time feedback system to adjust arrival time and polarization of single photons. In this way, the indistinguishability of photons distributed through fiber channels could be guaranteed, thus achieving efficient BSM. As a consequence, we have successfully implemented a quantum teleportation system operating at a rate of 7.1 ± 0.4 Hz over a fiber channel spanning 64 km in a metropolitan area. Moreover, employing the decoy state technique, we achieved an average fidelity of single photons at approximately 90.6 ± 2.6%. This implementation marks a significant achievement in the development of quantum internet and paves the way for investigating applications of quantum information utilizing a source of entangled photons.

Quantum key distribution (QKD) establishes a private, shared cryptographic key between the remote parties. The QKD based on quantum entanglement is important for

Figure 9.
(a) Aerial view of the teleportation system based on UESTC backbone network. (b) Scheme of the teleportation system. From ref. [65] (reuse with approved CC BY license).

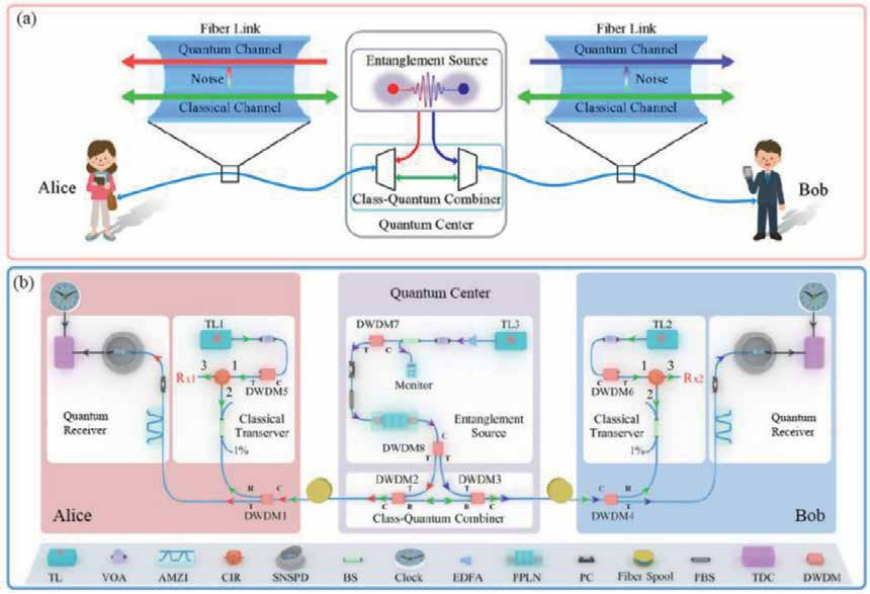

Figure 10.
(a) Illustration of entanglement distribution coexisting with classical fiber communication system. Entangled photons are distributed to Alice and bob. (b) Experimental setup in 40-km fiber [66].

future quantum secure communication networks, because photonic entanglement could be extended over remote notes and may not require additional quantum random number generators. To date, most of works on this topic have employed dark fibers. It would be more preferable to develop quantum network coexisting with classical fiber communication system. Therefore, we have successfully demonstrated the coexistence of energy-time entanglement-based QKD and classical optical communication using DWDM in the telecom C-band [66]. The configuration is illustrated in **Figure 10**. Consequently, we have experimentally verified that energy-time entanglement-based QKD can coexist with bidirectional 20 Gbps data communication over a 40-km-long optical fiber. Ultimately, employing the BBM92 protocol for QKD, we achieved a raw key generation rate of 245 bits per second and a quantum bit error rate of 8.88%. This experimental demonstration highlights the convenient compatibility between entanglement-based QKD and classical fiber communication, showcasing its immense potential for quantum networks.

4. Single-photon detectors

A single-photon detector is a photodetector, which can respond to incident light signal as weak as one single photon. Single-photon detectors play a widespread role in the field of quantum information processing since they serve as key devices, for example, readout in quantum computing, receiving in quantum communication and photon measurement in quantum metrology. We have had a review paper on a single-photon detector [67]. We focused our research on Geiger-mode avalanche photodiodes (single-photon avalanche diodes [68, 69], negative feedback avalanche diodes [70]) and the application of the two-dimensional (2D) materials for photon-level detectors [71]. Moreover, we have proposed fiber Bragg grating sensing system by utilizing single-photon detectors [72, 73].

4.1 Single-photon avalanche detectors

Avalanche photodiodes (APD) have been well studied and well fabricated for the application in many fields, for which we had a review paper on our previous works [74]. Geiger-mode (GM) avalanche photodiodes (APD) have detecting sensitivity as precise as single-photon level, so they are usually also termed as single-photon avalanche detectors (SPADs). Based on our previous works [69, 74], we recently performed more studies on Gm-APD or SPAD design and fabrication. In Ref. [68], we have proposed a detecting system of high-speed photon counting rates with an active quench and reset integrated circuit (AQR-IC) driving a InGaAs GM-APD at near-infrared range. The APD's parasitic capacitance and the circuit's input port were utilized to convert avalanche current into a voltage signal. This signal was then sent to an FPGA system for calculating counting rates, with the dead time being adjusted by the FPGA for greater flexibility in photon counting applications. The AQR-IC chip and PCB-based photon counting system are depicted in **Figure 11**. Fabricated using SMIC 0.18 μm CMOS technology, this proposed AQR-IC can achieve the maximum photon-counting rate as high as 15.6 MHz, with dead time tunable from 64 ns up to 163.6 μs at 20 ns of resolution—thereby enhancing single photon detection flexibility when operated in free-running mode. In addition, we recently fabricated a specific free-running InGaAs SPAD device, which has a very low dark count rate of 1.6 kHz and quite high photon counting rate of ~10 MHz. This device may be more available for quantum application than those reported so far.

Besides the performance improvement in single-element SPAD devices, progress has also been made on single photon imaging, that is, focal-plane single photon detecting arrays. By epitaxially growing the precise material structure and diffusing dopants locally and accurately using metalorganic chemical vapor deposition (MOCVD), fabricating the device structure using lithography, inductive coupled plasma etching (ICP), metal deposition, etc., designing and processing the integrated readout circuit chip, performing flip-chip In-shot bonding, and TEC cooled packaging, InGaAs SPAD arrays scaled 128 × 32 were successfully formed. **Figure 12** shows the measured results of photon detection efficiency (PDE) and dark count rate (DCR) for one of the fabricated arrays. It indicates an average PDE of 25% and DCR mostly lower than 9 kHz. These characteristics are as good as available for application, and we are actually trying to test their performance in some application scenes such as single-photon imaging Lidar and quantum Lidar [75].

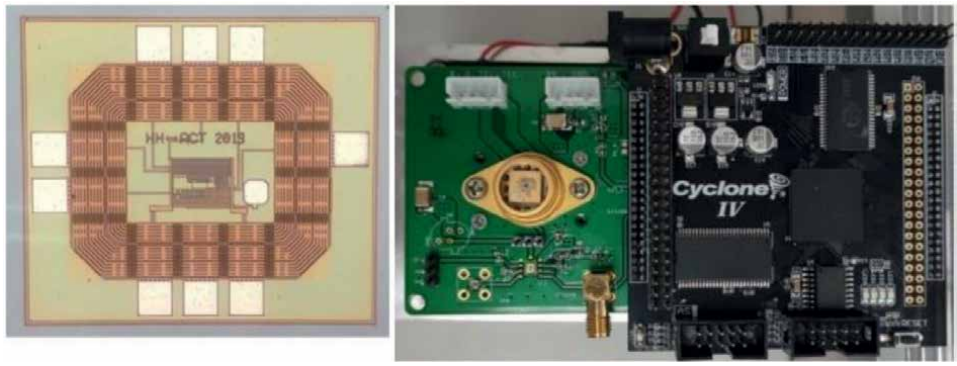

Figure 11.
(a) AQR-IC chip and (b) the photon counting system on PCB. From ref. [68] (reuse with approved IEEE license 5,606,570,125,207).

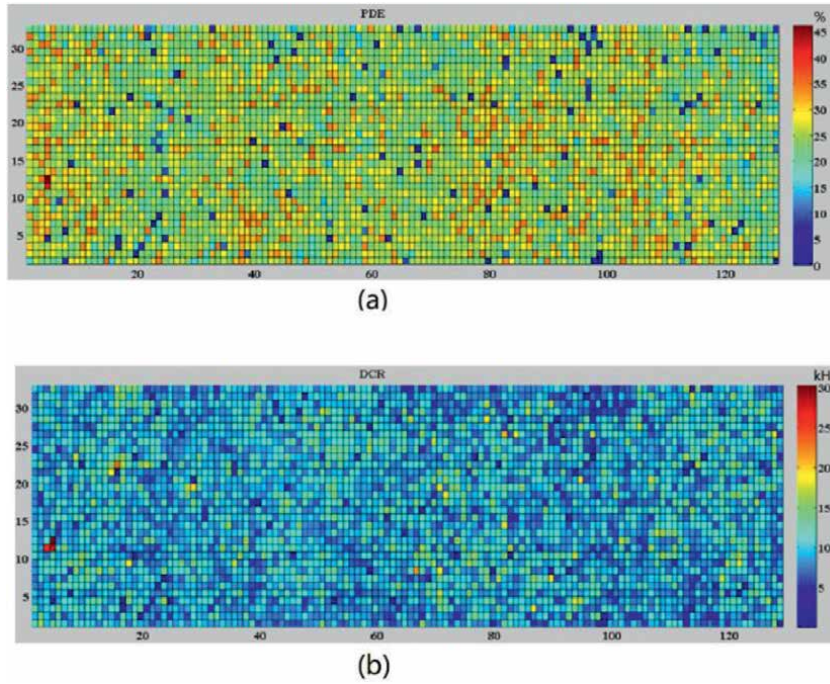

Figure 12.
The measured (a) PDE and (b) DCR of a newly fabricated 128 × 32 InGaAs SPAD array.

4.2 Negative feedback avalanche diodes for single-photon detection

With the advantages of fast quenching speed, low afterpulsing, and easy integration, negative feedback avalanche diodes (NFADs) can be used in quantum communication, fluorescence spectrum detection, single-photon counting imaging, and other application [76]. The research on NFAD devices and their application in single-photon detecting system has thus been of great significance. In Ref. [70], we have described the novel design of NFAD, and reviewed the development and application of NFAD devices in recent years. By monolithically integrating a film resistance onto SPAD, the formed self-passive quenching circuit in NFAD brings about improvements in especially afterpulsing and effectively enables photon number resolution. Further hybridizing active quenching circuit, the single-photon detection system composed of NFAD performs much better than that of conventional SPAD. Single-photon NFADs demonstrate more practical application potential in quantum information processing.

For further improvement in this field, we design new readout circuit for NFAD. To resolve the problems of avalanche signal detection and processing, afterpulsing suppression, dark counting rate, and detection efficiency of NFAD, we propose a free-running readout circuit architecture design based on InGaAs NFAD [77]. In this circuit, an ultra-low noise amplification circuit was designed, in which the noise was only ~651 μV_{rms}. At the same time, the circuit uses digital coding to control the discrimination threshold voltage and realizes precise modulation of the threshold voltage with an accuracy of 150 μV. A control circuit module based on FPGA was then constructed. The combination of digital coding control and feedback resistance was adopted to realize a large range (4.5~90 V) and high precision (0.5%), high-voltage power output. The high precision adjustable dead time delay was realized by counting

the high-frequency clock pulse signal. The photon pulse is accumulated by a 32-bit counter with high-speed (4 ns) and large-capacity counting ($1 \sim 2^{32}$). As a result, the minimum dead time becomes 20 ns, shorted by at least 70 ns. Finally, a single-photon counting module is built for testing the manufactured physical circuits. The results showed that the circuit can realize 0.1~100 μs dead time adjustment, and the NFAD can be much faster than before in quenching and recovering. This work provides a reference for the subsequent design of NFAD single-photon imaging system with integrated readout circuit.

4.3 Two-dimensional materials for photodetectors

The utilization of 2D substances presents a novel approach in creating nanoscale photodetectors [78]. Recent advancements have demonstrated that these 2D materials can be employed to fabricate both APDs and SPADs [79]. Our study in Ref. [80] extensively examined the structural, electronic, and optical characteristics of black phosphorus (BP) and indium selenide (InSe) monolayers, along with their BP/InSe heterojunctions using first-principle calculations. The analysis revealed that these materials possess remarkable geometric symmetry alongside appropriate bandgap values. Based on the findings regarding band offset, charge decomposition in bands, and electrostatic potential, it can be concluded that the heterojunction structure effectively suppresses the electron-hole pair recombination. This suppression is advantageous for enhancing carrier mobility in photoelectric devices. Furthermore, exceptional optical performance is observed in terms of refractive index, electron energy loss, reflectivity, absorption coefficient, extinction coefficient, and photon optical conductivity. The above outcomes suggest a promising future application potential for 2D materials in avalanche diodes or even single-photon detectors.

4.4 Application of single-photon detectors

Due to its compact size, ability to sense multiple points simultaneously, and resistance to electromagnetic interference, the optical fiber sensor that utilizes fiber Bragg gratings (FBG) is well-suited for monitoring physical variables in challenging environments including extreme temperatures [81], high pressures [82], and intense radiation [83]. By employing single-photon detectors, the FBG sensor has the potential to achieve quantum-level measurements. In a previous study [72], we have successfully demonstrated a highly efficient FBG sensing system with dense temporal multiplexing using single photon detection at 1.5-μm wavelength. A spatial accuracy of 5.0 cm has been accomplished, mainly depending on the time jitter of a single-photon detector and the duration of laser pulses. By employing the dual-wavelength differential detection (DWDD) technique, we achieved a wavelength precision of 0.5 pm within a range of 550 pm, resulting in an associated temperature sensitivity of 0.05°C. This sensitivity can be further enhanced to 0.01°C by elevating the repetition rate of laser pulses.

However, a shorter probe pulse width reaches a higher spatial resolution, which inevitably causes a spectrum broadening according to the Fourier transform theory. Namely, high-precision FBG sensing in the time and spectrum domains cannot be performed simultaneously. In Ref. [73], we have investigated the effect of spectrum broadening on a photon-counting FBG sensing system with a DWDD method. We built a theoretical model and characterized the photon-counting FBG sensing systems at different spatial resolutions. **Figure 13** shows the experimental setup of high spatial

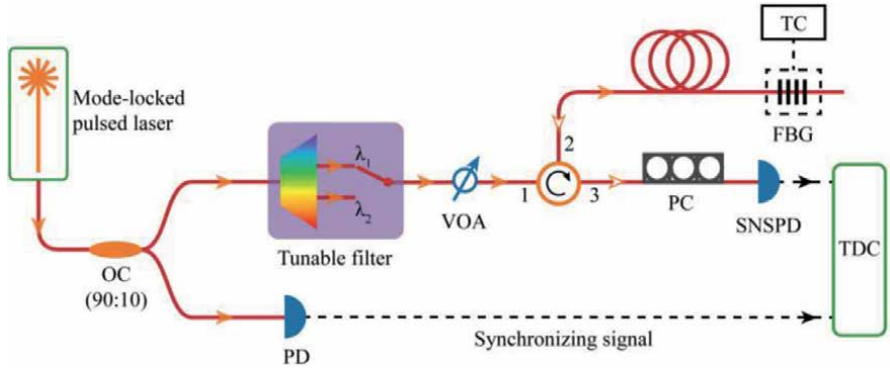

Figure 13.
Experimental setup of high spatial resolution DWDD. From ref. [73] (reuse with approved CC BY license).

resolution DWDD. A broadband coherent probe laser was generated from a mode-locked pulsed laser, and then divided into two parts by an optical coupler (OC, 90:10). One was received by an InGaAs photoelectric detector to generate a synchronizing electronic signal for a high-resolution time-to-digital converter (TDC). Then, another probe light was injected in a tunable filter to generate a pulse light with different spectral width at the central wavelength of 1550.1 nm or 1550.2 nm in turn. In order to avoid the saturation of a single-photon detector, the mean photon number of the probe laser was attenuated to 0.003 per pulse by adjusting a variable optical attenuator (VOA). As a result, a commercial FBG with a spectral width of 0.6 nm, an optimal spatial resolution of 3 mm and a corresponding sensitivity of 2.03 nm^{-1} can be achieved.

5. Other devices

In addition to the optoelectronic devices described above, we have also conducted abundant research on quantum memory [13, 84, 85], optomechanical system [86–88], and nano-opto-electro-mechanical system [89–91], including experimental studies and topic reviews.

5.1 Quantum memory

Quantum networks will probably be the main working platforms of the future quantum information technology and thus is very important in current quantum information science. Quantum memory, which is at the core of long-distance quantum repeater architectures, is the key element for quantum networks. Quantum memories have the capability to retain the quantum state of a photon or any other entangled particle while preserving its quantum information intact. In this field, we have studied photonic quantum memory based on rare-earth ions doped in solid-state materials. Erbium-doped optical fibers, which involve the incorporation of rare-earth ions into solid-state materials, exhibit efficient interaction between photons and atoms in the telecom-C band. These fibers are considered prospective candidates for quantum information processing applications, particularly in photonic quantum memory. In an experimental setting at temperatures below 10 mK, we successfully observed optical nutation in a 9.5-meter-long fiber doped with erbium ions at a concentration of 200 ppm [84]. The coherent interaction between the laser and

ensemble of erbium ions resulted in the reduction of optical nutation and provided valuable insights into transition dipole moments. We investigated how transition dipole moments vary with laser wavelength and magnetic strength, finding that a transition dipole moment about 3.4×10^{-32} Cm was achieved at 1537 nm and 0.2 T. This research lays the foundation for realizing quantum networks in the solid-state form and operating within the telecom-C band frequency range.

Furthermore, we have demonstrated both high-bandwidth and multiplexed quantum memory for C-band photons by utilizing the atomic frequency comb (AFC) quantum memory protocol in erbium-doped silica-fiber (EDF) [85]. **Figure 14** shows the experimental setup in this demonstration. The main advantage of this protocol is that the number of photons that can be stored at the same time is determined only by the time-bandwidth product. However, due to the significant inhomogeneous broadening and limited homogeneous linewidth exhibited by the employed EDF, the demonstrated quantum memory has a large storage bandwidth and a long storage time. There could be more than five spectral modes multiplexed—each 10 GHz wide—as well as over up to 330 temporal modes. As a result, we achieved the highest demonstrated multimode capacity to date, namely the simultaneous storage of 1650 heralded single photons. By making some improvements to our experimental scheme, a maximum major-mode capacity of 11,500 modes yielded by the time bandwidth product of this quantum memory could be attained. This work provides important guidance for the implementation of quantum networks based on multiplexed and broadband solid-state quantum memories.

As described above, we have made numerous significant advances in quantum networks, including quantum photon source, quantum teleportation, quantum key distribution, quantum memory, etc.

To provide a clear understanding of the current progress and future direction of quantum networks, we conducted an analysis on the significant advancements in both theory and experimentation over the last 20 years toward establishing entangled quantum nodes and ultimately constructing a global quantum network [13]. This comprehensive review encompasses the achievements made in various physical frames including single atoms, trapped ions, cold atomic ensembles, solid-state hosts doped with rare-earth ions and diamonds with nitrogen-vacancy centers. Additionally, we explored the available methods and encountered challenges associated with building practical quantum networks.

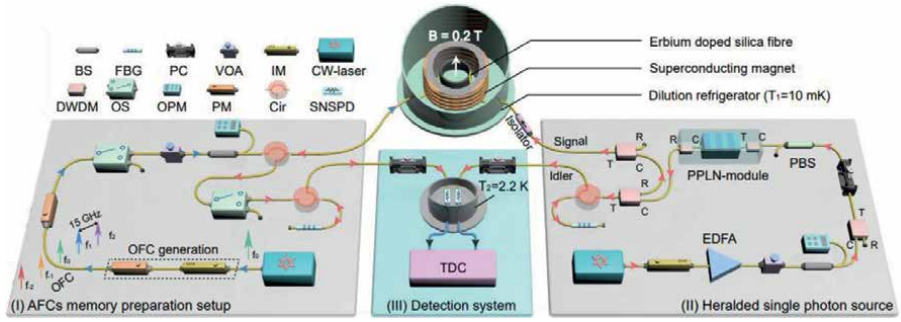

Figure 14.
The experimental setup consists of (I) multi-channel AFCs, (II) full telecom C-band heralded single photon source, and (III) measurement system. From ref. [85] (reuse with approved CC BY license).

5.2 Optomechanical system

A novel nanostructure called an optomechanical crystal nanobeam cavity has been developed, which combines both optical cavity and mechanical resonator. This innovative structure shows great potential in various applications such as modulators, sensors, and transducers. In our research, we have conducted a theoretical analysis on the impact of fabrication imperfections on the characteristics of nanobeam cavities [86]. Our findings indicate that altering the size of air holes leads to an increase in both the optomechanical coupling parameter and the optical resonance frequency, with coefficients of 0.01 MHz/nm and 0.36 THz/nm, respectively. Conversely, changing the size of air holes results in a decrease in mechanical resonance frequency at a coefficient of −0.03 GHz/nm. Interestingly, shifting the air hole line does not significantly affect any of these investigated characteristics. These insights provide valuable guidance for improving the fabrication process involved in creating nanobeam cavities.

After decades of research on entanglement generation, various schemes based on different physical platforms and information carriers have reported. Among the schemes, optomechanical systems have become a particularly promising platform due to their versatility in design, fabrication, and control. In this perspective, we have conducted a theoretical study on the generation of steady-state entanglement between optical and mechanical modes in single optomechanical crystal nanobeam [87]. As shown in **Figure 15(a)**, we considered a single optomechanical crystal cavity, including an integrated mechanical and optical nanoscale resonator within two mirror regions, formed on the surface of a microchip based on silicon-on-insulator. **Figure 15(b)** and **(c)** shows the E_y component of optical fundamental mode at telecom band and the placement field of the corresponding fundamental breathing mode, respectively. By using finite element simulations and logarithmic negativity as the entanglement measure, we have comprehensively studied the optimized parameter regimes in red- and blue-detuned optical pump situations. The results showed that the entanglement is robust against temperature and could reach an order of 10^{-2}. This work suggests important clues for the design of nanobeam structures for different application scenarios.

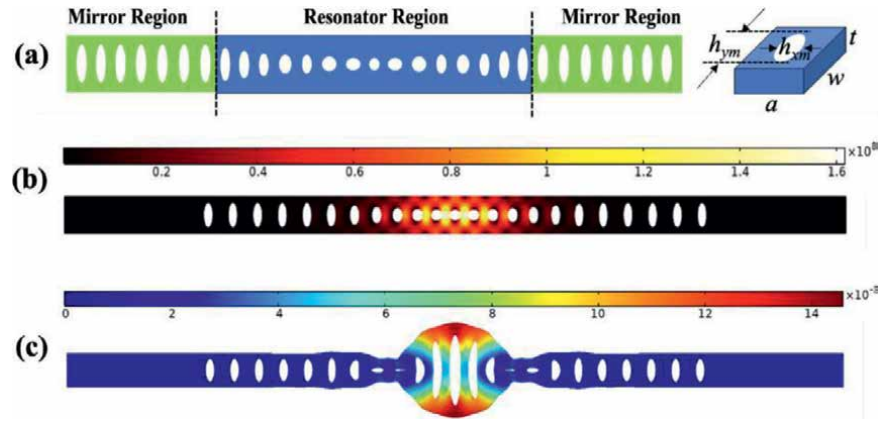

Figure 15.
(a) The schematic diagram of the plane-viewed silicon optomechanical crystal nanobeam cavity and unit cell geometry in the mirror region; (b) E_y component of the fundamental optical mode at telecom-band; (c) displacement field of the corresponding fundamental breathing mode [87].

Exploration of fundamental quantum physics and advancements in quantum information technologies greatly benefit from the significant role played by quantum entanglement in optomechanical systems. In this particular domain, we have reviewed the advancements in theory and experimentation concerning entangled states at a macroscopic level within optomechanical systems, and have provided insights into the future potential applications of this field [88]. The review also includes a concise introduction to key theoretical tools that aid in comprehending and addressing entanglement issues in opto-mechanics. Furthermore, we have introduced the entangling interaction between the electromagnetic fields and a mechanical oscillator, as well as that among multiple mechanical oscillators and that of electromagnetic fields associated with a mechanical oscillator. Additionally, we have summarized various approaches to mitigate the effect from thermal noise, which can enhance experimental feasibility and practical applicability. In conclusion, cryogenic environments will continue to play a pivotal role in future experimental studies in this field for an extended period. Maintaining quantum characteristics in more conventional settings will be an essential focus for practical applications in quantum optomechanical system.

5.3 Nano-opto-electro-mechanical system

The nano-opto-electro-mechanical system (NOEMS) is an emerging category of hybrid systems that integrate optical, electrical, and mechanical functionalities within nanoscale devices. Among them, graphene has emerged as a promising material for implementing mechanical resonators due to its exceptional characteristics, including lightweight composition, high-quality factors, and adjustable resonant frequencies. In our study, we have introduced a phonon laser operating at room temperature by utilizing an opto-mechanic cavity [89]. This cavity consisted of graphene and a silicon substrate forming an optical enclosure, with the added functionality of the graphene sheet serving as both the coupling mirror and the mechanical resonator.

The phonon dissipations decreased as the power of the pumping laser increased, and ceased when the pump power reached a sufficient level. Subsequently, the phonon transitioned into a state referred to as stimulated emission, resembling the process of photon lasing. The occurrence of phonon lasing was confirmed through observation of a distinct threshold in oscillation amplitude and a reduction in vibration mode linewidth. We anticipate that our discoveries will provide novel perspectives for developing functional devices based on mechanical graphene resonators and potentially find applications in quantum information processing.

Considering the 2D antiferromagnetic semiconductor chromium thiophosphate ($CrPS_4$) for its excellent structure, photoelectric properties, and potential magnetic characteristics, we have experimentally studied the mechanical properties of layered $CrPS_4$ and explored the resonance characteristics of a new few-layer $CrPS_4$ nanomechanical resonator [90]. **Figure 16** shows the material properties of layered $CrPS_4$ and preparation of mechanical resonators in this work. The results exhibited exceptional vibration properties using the laser interferometry setup, showcasing the distinct resonant mode, capability to operate at extremely high frequency and gate tuning. Additionally, by analyzing temperature-regulated resonant frequencies, we successfully detected the magnetic phase transition of $CrPS_4$ strips. This discovery validates the correlation between mechanical vibration and magnetic phase. These results lay a solid foundation for future exploration and utilization of 2D magnetic material resonators in quantum metrology research.

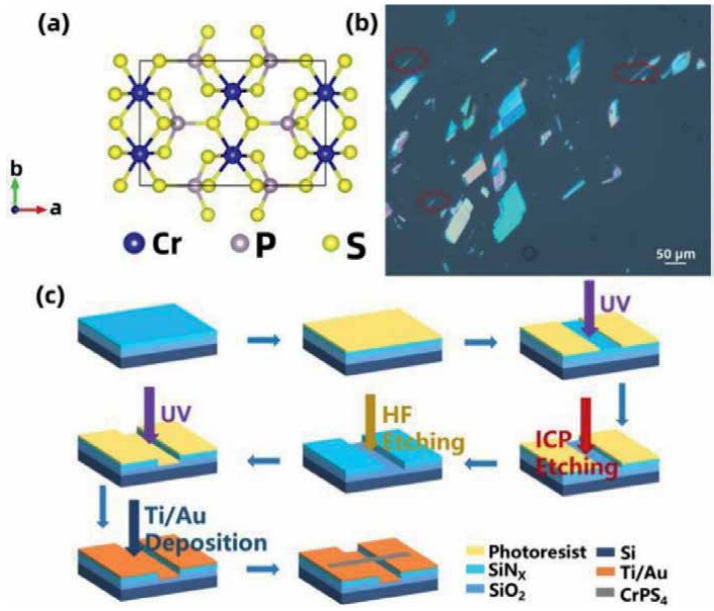

Figure 16.
Material properties of layered $CrPS_4$ and preparation of mechanical resonators. (a) the crystal structure of $CrPS_4$ is presented as an ab plane. (b) Layered $CrPS_4$ obtained by mechanical exfoliation under optical microscope. (c) Detailed process flowchart of $CrPS_4$ mechanical resonators. From ref. [90] (reuse with approved CC BY license).

Given the extensive activity in this emerging field, we have reviewed recent advancements and significant accomplishments in NOEMSs, with a particular focus on the fundamental aspects of the hybrid system and its diverse range of applications [91]. Additionally, our review delves into the distinctions between classical information transduction and quantum information processing when applying NOEMS, thereby presenting an expanded scope for engineering and enhancing NOEMS within the realm of quantum mechanics.

6. Conclusion

In order to realize practical quantum systems in the future, our group have made efforts to create and investigate quantum devices by using optoelectronic techniques. QD-embedded nanocavities were designed to improve the efficiency of and to realize on demand single photon emitters. Spectral multiplexing technique enabled the fabrication of a heralded single photon source with high purity and speed, approaching on-demand single photon emitting. A quantum random number generator working at room temperature was constructed based on single-photon emission from defects in commercial GaN material. Applying cascaded second-order nonlinear optical process in PPLN waveguides, we developed an entangled photon emitter with visibility of 97% and noise level nearly 10 times better. Another photon entangler with visibility of over 99% was established using Si_3N_4 micro-rings. Readout circuits were optimized to help fabricating high-quality SPAD devices, and SPAD focal plane devices were improved to 128 × 32 array for single photon and quantum imaging. A quantum memory was achieved to simultaneously store 1650 single photons at low temperatures, and a few opto-electro-mechanical devices were experimentally tried to obtain

quantum-level measurement ability for minor quantities. Our studies might be a step forward to the realization of practical quantum information networks.

Acknowledgements

This work was partially supported by the National Key Research and Development Program of China (Nos. 2018YFA0307400, 2018YFA0306102, 2019YFB2203400, 2021YFA0718803); Sichuan Science and Technology Program (Nos. 2020YFG0466, 2021YFSY0063, 2021YFSY0062, 2021YFSY0064, 2021YFSY0065, 2021YFSY0066, 2022YFSY0061, 2022YFSY0062, 2022YFSY0063); National Natural Science Foundation of China (Nos. U19A2076, 62005039); Innovation Program for Quantum Science and Technology (No. 2021ZD0301702); Chengdu Science and Technology Program No. 2021YF0800159GX; and the Rongpiao Plan of Chengdu city, China.

Conflict of interest

The authors declare no conflict of interest.

Author details

Hai-Zhi Song[1,2,3*], Qiang Zhou[2], Guangwei Deng[2], Qian Dai[1], Zichang Zhang[1,2] and You Wang[1,2]

1 Quantum Research Center, Southwest Institute of Technical Physics, Chengdu, China

2 Institute of Fundamental and Frontier Sciences, University of Electronic Science and Technology of China, Chengdu, China

3 Laboratory of High Power Semiconductor Laser, Changchun University of Science and Technology, Changchun, China

*Address all correspondence to: hzsong1296@163.com

References

[1] Wu J, Huang Y, Lu C, Ding T, Zheng Y, Chen X. Tunable linear polarization-state generator of single photons on a lithium Niobate Chip. Physical Review Applied. 2020;**13**(6):064068. DOI: 10.1103/PhysRevApplied.13.064068

[2] Boschi D, Branca S, De Martini F, Hardy L, Popescu S. Experimental realization of teleporting an unknown pure quantum state via dual classical and Einstein-Podolsky-Rosen channels. Physical Review Letters. 1998;**80**(6):1121-1125. DOI: 10.1103/PhysRevLett.80.1121

[3] Bouwmeester D, Pan J-W, Mattle K, Eibl M, Weinfurter H, Zeilinger A. Experimental quantum teleportation. Nature. 1997;**390**(6660):575-579. DOI: 10.1038/37539

[4] O'Brien JL. Optical quantum computing. Science. 2007;**318**(5856): 1567-1570. DOI: 10.1126/science.1142892

[5] Pan J-W, Gasparoni S, Ursin R, Weihs G, Zeilinger A. Experimental entanglement purification of arbitrary unknown states. Nature. 2003;**423**(6938):417-422. DOI: 10.1038/nature01623

[6] Pan J-W, Simon C, Brukner Č, Zeilinger A. Entanglement purification for quantum communication. Nature. 2001;**410**(6832):1067-1070. DOI: 10.1038/35074041

[7] Yamamoto T, Koashi M, Özdemir ŞK, Imoto N. Experimental extraction of an entangled photon pair from two identically decohered pairs. Nature. 2003;**421**(6921):343-346. DOI: 10.1038/nature01358

[8] Yao XC, Wang TX, Chen HZ, Gao WB, Fowler AG, Raussendorf R, et al. Experimental demonstration of topological error correction. Nature. 2012;**482**(7386):489-494. DOI: 10.1038/nature10770

[9] Gisin N, Ribordy G, Tittel W, Zbinden H. Quantum cryptography. Reviews of Modern Physics. 2002;**74**(1):145-195. DOI: 10.1103/RevModPhys.74.145

[10] Kasture S, Lenzini F, Haylock B, Boes A, Mitchell A, Streed EW, et al. Frequency conversion between UV and telecom wavelengths in a lithium niobate waveguide for quantum communication with Yb+ trapped ions. Journal of Optics. 2016;**18**(10):104007. DOI: 10.1088/2040-8978/18/10/104007

[11] Kimble HJ. The quantum internet. Nature. 2008;**453**(7198):1023-1030. DOI: 10.1038/nature07127

[12] Wehner S, Elkouss D, Hanson R. Quantum internet: A vision for the road ahead. Science. 2018;**362**(6412):eaam9288. DOI: 10.1126/science.aam9288

[13] Wei S-H, Jing B, Zhang X-Y, Liao J-Y, Yuan C-Z, Fan B-Y, et al. Towards real-world quantum networks: A review. Laser & Photonics Reviews. 2022;**16**(3):2100219. DOI: 10.1002/lpor.202100219

[14] Wengerowsky S, Joshi SK, Steinlechner F, Hübel H, Ursin R. An entanglement-based wavelength-multiplexed quantum communication network. Nature. 2018;**564**(7735):225-228. DOI: 10.1038/s41586-018-0766-y

[15] Boyer V, Marino AM, Pooser RC, Lett PD. Entangled images from four-wave mixing. Science.

2008;**321**(5888):544-547. DOI: 10.1126/science.1158275

[16] Brida G, Genovese M, Ruo BI. Experimental realization of sub-shot-noise quantum imaging. Nature Photonics. 2010;**4**(4):227-230. DOI: 10.1038/nphoton.2010.29

[17] Giovannetti V, Lloyd S, Maccone L. Advances in quantum metrology. Nature Photonics. 2011;**5**(4):222-229. DOI: 10.1038/nphoton.2011.35

[18] Treps N, Grosse N, Bowen WP, Fabre C, Bachor H-A, Lam PK. A quantum laser pointer. Science. 2003;**301**(5635):940-943. DOI: 10.1126/science.1086489

[19] Bharadwaj D, Thyagarajan K. Direct generation of hybrid entangled photon pairs in waveguides. Journal of the Optical Society of America B. 2018;**35**(4):790-796. DOI: 10.1364/JOSAB.35.000790

[20] Kumar R, Ghosh J. Parametric down-conversion in ppLN ridge waveguide: A quantum analysis for efficient twin photons generation at 1550 nm. Journal of Optics. 2018;**20**(7):075202. DOI: 10.1088/2040-8986/aac7da

[21] Kumar R, Ghosh J. SPDC photon pairs using a spatially anti-symmetric pump beam in a ppLN ridge waveguide. Applied Physics B. 2020;**126**(11):186. DOI: 10.1007/s00340-020-07537-x

[22] Santandrea M, Stefszky M, Ansari V, Silberhorn C. Fabrication limits of waveguides in nonlinear crystals and their impact on quantum optics applications. New Journal of Physics. 2019;**21**(3):033038. DOI: 10.1088/1367-2630/aaff13

[23] Zhang K, He J, Wang J. Two-way single-photon-level frequency conversion between 852 nm and 1560 nm for connecting cesium D2 line with the telecom C-band. Optics Express. 2020;**28**(19):27785-27796. DOI: 10.1364/OE.402355

[24] IBM. The IBM quantum heavy hex lattice. 2021. Available from: https://research.ibm.com/blog/heavy-hex-lattice

[25] Gambetta JM, Chow JM, Steffen M. Building logical qubits in a superconducting quantum computing system. npj Quantum Information. 2017;**3**:2. DOI: 10.1038/s41534-016-0004-0

[26] Beterov I. Quantum computers based on cold atoms. Optoelectronics, Instrumentation and Data Processing. 2020;**56**:317-324. DOI: 10.3103/S8756699020040020

[27] Zhang X, Li H-O, Cao G, Xiao M, Guo G-C, Guo G-P. Semiconductor quantum computation. National Science Review. 2019;**6**(1):32-54. DOI: 10.1093/nsr/nwy153

[28] Azuma H. Quantum computation with Kerr-nonlinear photonic crystals. Journal of Physics D: Applied Physics. 2008;**41**(2):025102. DOI: 10.1088/0022-3727/41/2/025102

[29] Wolters J, Buser G, Horsley A, Béguin L, Jöckel A, Jahn JP, et al. Simple atomic quantum memory suitable for semiconductor quantum dot single photons. Physical Review Letters. 2017;**119**:060502. DOI: 10.1103/PhysRevLett.119.060502

[30] Lamata L. Quantum and optoelectronic devices, circuits and systems. Electronics. 2023;**12**(7):1717. DOI: 10.3390/electronics12071717

[31] Michaelis de Vasconcellos S, Gordon S, Bichler M, et al. Coherent

control of a single exciton qubit by optoelectronic manipulation. Nature Photon. 2010;**4**:545-548. DOI: 10.1038/nphoton.2010.124

[32] Kimura S, Kumano H, Endo M, Suemune I, Yokoi T, Sasakura H, et al. Photon Antibunching observed from an InAlAs single quantum dot. Japanese Journal of Applied Physics. 2005;**44**(6L):L793. DOI: 10.1143/JJAP.44.L793

[33] Cheng R, Huang S, Xu Q, Xie X, Zhang W, Zhou Q, et al. Research progress of lithium niobate waveguide and its application in quantum information technology. In: 2021 Photonics & Electromagnetics Research Symposium (PIERS); 21-25 November 2021. Hangzhou, China: IEEE; 2021. pp. 877-896

[34] Wrachtrup J, Jelezko F. Processing quantum information in diamond. Journal of Physics: Condensed Matter. 2006;**18**(21):S807. DOI: 10.1088/0953-8984/18/21/S08

[35] Kagan CR, Bassett LC, Murray CB, Thompson SM. Colloidal quantum dots as platforms for quantum information science. Chemical Reviews. 2021;**121**(5):3186-3233. DOI: 10.1021/acs.chemrev.0c00831

[36] Liu X, Hersam MC. 2D materials for quantum information science. Nature Reviews Materials. 2019;**4**:669-684. DOI: 10.1038/s41578-019-0136-x

[37] Cao Z-L, Hu F-R, Zhang C-F, Zhu S-N, Xiao M, Wang X-Y. Optical studies of semiconductor perovskite nanocrystals for classical optoelectronic applications and quantum information technologies: A review. Advanced Photonics. 2020;**2**(5):054001. DOI: 10.1117/1.AP.2.5.054001

[38] Grimsmo AL, Royer B, Kreikebaum JM, Ye Y, O'Brien K, Siddiqi I, et al. Quantum metamaterial for broadband detection of single microwave photons. Physical Review Applied. 2021;**15**:034074. DOI: 10.1103/PhysRevApplied.15.034074

[39] Kumano H, Kimura S, Endo M, Suemune I, Sasakura H, Adachi S, et al. Triggered single-photon emission and cross-correlation properties in InAlAs quantum dot. Physica E: Low-dimensional Systems and Nanostructures. 2006;**32**(1):144-147. DOI: 10.1016/j.physe.2005.12.027

[40] Takemoto K, Nambu Y, Miyazawa T, Wakui K, Hirose S, Usuki T, et al. Transmission experiment of quantum keys over 50 km using high-performance quantum-dot single-photon source at 1.5 μm wavelength. Applied Physics Express. 2010;**3**(9):092802. DOI: 10.1143/APEX.3.092802

[41] Song H-Z, Hadi M, Zheng Y, Shen B, Zhang L, Ren Z, et al. InGaAsP/InP Nanocavity for single-photon source at 1.55-μm telecommunication band. Nanoscale Research Letters. 2017;**12**(1):128. DOI: 10.1186/s11671-017-1898-y

[42] Huang S, Xie X, Xu Q, Zhao X, Deng G, Zhou Q, et al. Fabrication tolerance of InGaAsP/InP-air-aperture micropillar cavities as 1.55-μm quantum dot single-photon sources. Current Optics and Photonics. 2020;**4**(6):509-515. DOI: 10.3807/COPP.2020.4.6.509

[43] Yu H, Yuan C, Zhang R, Zhang Z, Li H, Wang Y, et al. Spectrally multiplexed indistinguishable single-photon generation at telecom-band. Photonics Research. 2022;**10**(6):1417-1429. DOI: 10.1364/PRJ.450731

[44] Fan Y-R, Yuan C-Z, Zhang R-M, Shen S, Wu P, Wang H-Q, et al. Effect of dispersion on indistinguishability

between single-photon wave-packets. Photonics Research. 2021;**9**(6):1134-1143. DOI: 10.1364/PRJ.421180

[45] Luo Q, Cheng Z, Fan J, Tan L, Song H, Deng G, et al. Quantum random number generator based on single-photon emitter in gallium nitride. Optics Letters. 2020;**45**(15):4224-4227. DOI: 10.1364/OL.396561

[46] Meyer-Scott E, Silberhorn C, Migdall A. Single-photon sources: Approaching the ideal through multiplexing. Review of Scientific Instruments. 2020;**91**:041101. DOI: 10.1063/5.0003320

[47] Song H-Z. The development of quantum emitters based on quantum dots-a chapter. In: Yu P, Wang ZM, editors. Quantum Dot Optoelectronic Devices. Switzerland AG: Springer Nature; 2020. Chapter 3. pp. 83-106. DOI: 10.1007/978-3-030-35813-6

[48] Song H-Z, Takemoto K, Miyazawa T, Takatsu M, Iwamoto S, Yamamoto T, et al. Design of Si/SiO2 micropillar cavities for Purcell-enhanced single photon emission at 1.55 μm from InAs/InP quantum dots. Optics Letters. 2013;**38**:3241. DOI: 10.1364/OL.38.003241

[49] Song H-Z, Takemoto K, Miyazawa T, Takatsu M, Iwamoto S, Ekawa M, et al. High quality-factor Si/SiO2-InP hybrid micropillar cavities with submicrometer diameter for 1.55-μm telecommunication band. Optics Express. 2015;**23**(12):16264-16272. DOI: 10.1364/OE.23.016264

[50] Xie X-M, Xu Q, Shen B-Z, Chen J, Dai Q, Shi Z, et al. InGaAsP/InP micropillar cavities for 1.55 μm quantum-dot single photon sources. In: 6th Conference on Advances in Optoelectronics and Micro/Nano-Optics; 23-26 April 2017. Vol. 844(1). Nanjing, China: IOP Publishing; 2017. p. 012002

[51] Guo S-J, Zheng Y-Z, Weng Z, Yao H-C, Ju Y-H, Zhang L, et al. InGaAsP/InP-air-aperture microcavities for single-photon sources at 1.55-μm telecommunication band. In: Nanophotonics and Micro/Nano Optics III; 4 November 2016. Beijing, China: SPIE; 2016. DOI: 10.1117/12.2247841

[52] Song H-Z, Zhang W, Yu L-B, Wang Z-M. Micropillar cavity design for 1.55-μm quantum-dot single-photon sources. Journal of Electronic Science and Technology. 2019;**17**(3):221. DOI: 10.11989/JEST.1674-862X.71027010

[53] Song H-Z. Microcavities for silica-fiber based quantum information processing. In: Pyshkin S, Ballato J, editors. Optoelectronics – Advanced Device Structures. London, UK, Crotia: Intech, Chapter 2; 2017. pp. 21-48. DOI: 10.5772/67499

[54] Cheng R, Huang S, Xu Q, Xie X-M, Zhang W, Zhou Q, et al. Research Progress of lithium Niobate waveguide and its application in quantum information technology. In: IEEE Xplore/2021 Photonics & Electromagnetics Research Symposium (PIERS); 21-25 November 2021. Hangzhou, China: IEEE; 2022. pp. 877-896

[55] Huang S, Zhang W, Xi Q, Zhao XH, Xie X, Xu Q, et al. Robustness of Si/SiO_2-InP micropillar cavity for 1.55-μm single photon source. Laser Technology. 2020;**44**(5):532-537 (in Chinese)

[56] Jennewein T, Simon C, Weihs G, Weinfurter H, Zeilinger A. Quantum cryptography with entangled photons. Physical Review Letters. 2000;**84**(20):4729-4732. DOI: 10.1103/PhysRevLett.84.4729

[57] Mitchell MW, Lundeen JS, Steinberg AM. Super-resolving phase measurements with a multiphoton entangled state. Nature. 2004;**429**(6988):161-164. DOI: 10.1038/nature02493

[58] Sun Q-C, Mao Y-L, Chen S-J, Zhang W, Jiang Y-F, Zhang Y-B, et al. Quantum teleportation with independent sources and prior entanglement distribution over a network. Nature Photonics. 2016;**10**(10):671-675. DOI: 10.1038/nphoton.2016.179

[59] Jin R-B, Cai N, Huang Y, Hao X-Y, Wang S, Li F, et al. Theoretical investigation of a spectrally pure-state generation from isomorphs of KDP crystal at near-infrared and telecom wavelengths. Physical Review Applied. 2019;**11**(3):034067. DOI: 10.1103/PhysRevApplied.11.034067

[60] Li J, Yuan C, Shen S, Zhang Z, Zhang R, Li H, et al. Discrete frequency-bin entanglement generation via cascaded second-order nonlinear processes in Sagnac interferometer. Optics Letters. 2023;**48**(11):2917-2920. DOI: 10.1364/OL.489656

[61] Zhang Z, Yuan C, Shen S, Yu H, Zhang R, Wang H, et al. High-performance quantum entanglement generation via cascaded second-order nonlinear processes. npj Quantum Information. 2021;7(1):123. DOI: 10.1038/s41534-021-00462-7

[62] Fan Y-R, Lyu C, Yuan C-Z, Fan B-Y, Jing B, Zhou D-L, et al. Multi-wavelength correlated photon pairs generation in Si3N4 microring resonator. In: 2021 IEEE 6th Optoelectronics Global Conference (OGC); 15-18 September 2021. Shenzhen. China: IEEE; 2021. pp. 100-102

[63] Fan Y-R, Lyu C, Yuan C-Z, Deng G-W, Zhou Z-Y, Geng Y, et al. High-quality multi-wavelength quantum light sources on silicon nitride micro-ring chip. arXiv[quant-ph]. 2022;**2209**:11417. DOI: 10.48550/arXiv.2209.11417

[64] Shen S, Yuan C-Z, Zhang Z-C, Wang H-Q, Li H, You L-X, et al. High-performance quantum teleportation Systems at Telecom C-band. In: Conference on Lasers and Electro-Optics; 09 May 2021. San Jose, California: Optica Publishing Group; 2021. p. FM3M.2

[65] Shen S, Yuan C, Zhang Z, Yu H, Zhang R, Yang C, et al. Hertz-rate metropolitan quantum teleportation. Light: Science & Applications. 2023;**12**(1):115. DOI: 10.1038/s41377-023-01158-7

[66] Fan Y-R, Luo Y, Zhang Z-C, Li Y-B, Liu S, Wang D, et al. Energy-time Entanglement Coexisting with Fiber Optical Communication at Telecom C-band. arXiv[quant-ph]. 2023;**2305**:18696. DOI: 10.48550/arXiv.2305.18696

[67] Cheng B-T, Dai Q, Xie X-M, Xu Q, Zhang S, Song H-Z. Research progress of single-photon detectors. Laser Technology. 2022;**46**(5):601. DOI: 10.7510/jgjs.issn.1001-3806 (in Chinese)

[68] Yuan F, Lu XL, Jing L, Yang YX, Kong FL, Deng SJ, et al. A novel high-speed photon counting system with programmed dead time. In: 2019 IEEE 4th Optoelectronics Global Conference (OGC); 3-6 September 2019. Shenzhen, China: IEEE; 2019. pp. 85-88

[69] Song H-Z, Deng J, Dai Q, Shi Z, Yu L-B. Quantitative correlation between fabrication precision and device homogeneity of single-photon avalanche diodes. IEEE Transactions on Electron Devices. 2016;**63**(12):4845-4851. DOI: 10.1109/TED.2016.2618222

[70] Zhang S, Yuan F, Chen J, Xie X, Xu Q, Cheng B, et al. Research progress of negative feedback avalanche diode and its application. In: 2nd International Conference on Laser, Optics and Optoelectronic Technology (LOPET 2022); 20-22 May 2022. Qingdao, China: SPIE; 2022. pp. 182-191

[71] Huang X, Cao Q, Wan M, Song H-Z. Electronic and optical properties of BP, InSe monolayer and BP/InSe heterojunction with promising photoelectronic performance. Materials. 2022;**15**(18):6214. DOI: 10.3390/ma15186214

[72] Fan X, Ou Z, Zhang L, Zhang R, Yuan C, Deng G, et al. Dense temporally multiplexed Fiber Bragg grating sensing based on single-photon detection. Journal of Lightwave Technology. 2022;**40**(13):4458-4466. DOI: 10.1109/JLT.2022.3158074

[73] Ou Z, Fan X, Zhang L, Fan Y, Yuan C, You L, et al. Effect of spectrum broadening on photon-counting fiber Bragg grating sensing. Optics Express. 2023;**31**(5):8152-8159. DOI: 10.1364/OE.482821

[74] Song H-Z. Avalanche photodiode focal plane arrays and their application in laser detection and ranging. Chapter 9, in Advances Photodiodes - Research and Applications, ed. Kuan Chee, ISBN 978-953-51-6779-2, London, UKIntechOpen. 2018.

[75] Zheng-Ping LI, Huang X, Jiang P-Y, Hong Y, Yu H, Cao Y, et al. Super-resolution single-photon imaging at 8.2 kilometers. Optics Express. 2020;**28**(3):4076. DOI: 10.1364/OE.383456

[76] Itzler MA, Jiang X, Nyman B, et al. InP-based negative feedback avalanche diodes. In: Quantum Sensing and Nanophotonic Devices VI; 26 January 2009. Vol. 7222. California, United States: SPIE; 2009. pp. 462-473

[77] Yuan F, Lu X, Ke Z, Xie X, Liu Q, Yang Y, et al. A design of near-infrared single photon counting integrated module based on InGaAs/InP NFAD. Proceedings of SPIE. 2023;**12781**:127810Y. DOI: 10.1117/12.2687239

[78] Cheng B-T, Zho Y, Jiang R-M, Wang X-L, Huang S, Huang X-Y, et al. Structural, electronic and optical properties of some new Trilayer Van de Waals Heterostructures. Nanomaterials. 2023;**13**:1574. DOI: 10.3390/nano13091574

[79] Miao J, Wang C. Avalanche photodetectors based on two-dimensional layered materials. Nano Research. 2021;**14**:1878-1888. DOI: 10.1007/s12274-020-3001-8

[80] Zhang J, Itzler MA, Zbinden H, Pan J-W. Advances in InGaAs/InP single-photon detector systems for quantum communication. Light: Science & Applications. 2015;**4**(5):e286-e. DOI: 10.1038/lsa.2015.59

[81] Grobnic D, Smelser CW, Mihailov SJ, Walker RB. Long-term thermal stability tests at 1000 °C of silica fibre Bragg gratings made with ultrafast laser radiation. Measurement Science and Technology. 2006;**17**(5):1009. DOI: 10.1088/0957-0233/17/5/S12

[82] Wei Z, Song D, Zhao Q, Cui HL. High pressure sensor based on Fiber Bragg grating and carbon Fiber laminated composite. IEEE Sensors Journal. 2008;**8**(10):1615-1619. DOI: 10.1109/JSEN.2008.929070

[83] Gusarov AI, Berghmans F, Deparis O, Fernandez AF, Defosse Y, Megret P, et al. High total dose radiation effects on temperature sensing fiber Bragg

gratings. IEEE Photonics Technology Letters. 1999;**11**(9):1159-1161. DOI: 10.1109/68.784237

[84] Xi Q, Wei S, Yuan C, Zhang X, Wang Y, Song H, et al. Experimental observation of coherent interaction between laser and erbium ions ensemble doped in fiber at sub 10 mK. Science China Information Sciences. 2020;**63**(8):180505. DOI: 10.1007/s11432-020-2954-5

[85] Wei S-H, Jing B, Zhang X-Y, Liao J-Y, Li H, You L-X, et al. Storage of 1650 modes of single photons at telecom wavelength. 2022. DOI: 10.48550/arXiv.2209.00802

[86] Lv X, Fan B, Tang J, Xu N, Chen H, Zhang Y, et al. The influence of fabrication imperfections in an optomechanical crystal nanobeam cavity. In: Asia Communications and Photonics Conference/International Conference on Information Photonics and Optical Communications 2020 (ACP/IPOC); 24 October 2020. Beijing, China: Optica Publishing Group; 2020. p. M4A.19

[87] Cai Q, Fan B, Fan Y, Deng G, Wang Y, Song H, et al. Entangling optical and mechanical cavity modes in optomechanical crystal nanobeam. Physical Review A. 2023;**108**(2):022419. DOI: 10.1103/PhysRevA.108.022419

[88] Tang J-D, Cai Q-Z, Cheng Z-D, Xu N, Peng G-Y, Chen P-Q, et al. A perspective on quantum entanglement in optomechanical systems. Physics Letters A. 2022;**429**:127966. DOI: 10.1016/j.physleta.2022.127966

[89] Li W-J, Cheng Z-D, Kang L-Z, Zhang R-M, Fan B-Y, Zhou Q, et al. Phonon lasing with an atomic thin membrane resonator at room temperature. Optics Express. 2021;**29**(11):16241-16248. DOI: 10.1364/OE.423904

[90] Li B-L, Guo M-L, Chen J-F, Fang J-W, Fan B-Y, Zhou Q, et al. Very high-frequency, gate-tunable CrPS4 nanomechanical resonator with single mode. Optics Letters. 2023;**48**(10):2571-2574. DOI: 10.1364/OL.489345

[91] Xu N, Cheng Z-D, Tang J-D, Lv X-M, Li T, Guo M-L, et al. Recent advances in nano-opto-electro-mechanical systems. Nano. 2021;**10**(9):2265-2281. DOI: 10.1515/nanoph-2021-0082

Chapter 4

Algorithm for Calculating Coordinates of Images in an Optoelectronic Device with a Matrix Photodetector

Viktor Pachkov

Abstract

The algorithm described below simulates the functions of an optoelectronic CCD array angle meter. This algorithm makes it possible to generate implementations of useful signals from point emitters, external interference, and internal noise, as well as their additive mixture at the output of the device. In addition, it makes it possible to solve the problem of extracting a useful signal from a mixture with a constant background and external and internal noises, as well as determine the coordinates of images of emitters and evaluate the accuracy of determining these coordinates.

Keywords: CCD, simulation, optical electronic, simulation flowchart, background, noise

1. Introduction

Autonomous optical navigation and astro-orientation of spacecrafts is one possible way of improving the reliability of the spacecraft. Self-determination of the spacecraft is inextricably linked to the need to determine its exact orientation, which can be carried out using onboard optical devices based on multi-pixel converters. This work consists of an introduction, six chapters, a conclusion, and a list of literature. The first chapter is devoted to the review and analysis of Optical Electronic Instruments (OEIs) at the CCD. The second and third chapters discuss the features of signal conversion and processing in OEI with CCD, and the development of quasi-optimal methods for estimating the coordinates of images. The fourth chapter considers methods of estimating the coordinates of moving images of point emitters. The fifth chapter is devoted to the method of modeling angular OEIs. The sixth chapter shows the results of the simulation. In conclusion, the main results of the work are formulated. Attached are the modeling algorithms. This work is intended for engineers, researchers, and students.

2. Algorithm for calculating coordinates of images in an optoelectronic device with a matrix photodetector

2.1 Mathematical setting of the problem

The algorithm requires the following source data.

- Characteristics of emitters: stellar values for stars, their spectral class; radiation force, and its spectrum of emitters illuminated by the sun, as well as range to them. You must also specify the number of point sources and their angular coordinates;

- Characteristics of the optical system: angular field, diameter of the entrance pupil, focal length, and point scattering function (PSF);

- CCD matrix characteristics: format, pixel sizes, organization (frame, line-frame), operation mode (frame transfer or full illumination mode), quantum efficiency (spectral sensitivity), aperture characteristic (pixel sensitivity), charge transfer inefficiency, dark current density, noise at the output, dark current unevenness ("geometric noise"), and potential hole depth (wall);

- Characteristics of output circuit: discharge of analog-to-digital converter.

Then, based on the initial data, the implementation of the signal at the output of the CCD can be calculated according to formula (26), a useful signal is extracted according to formulae (27)–(29), its coordinates are determined using expressions (31)–(39), and a posterior probability of detecting a signal in a frame according to formulae (40)–(42) is calculated.

2.2 Algorithm description

The characteristics of an optoelectronic device with a CCD matrix can be investigated by simulation modeling. To this end, the processes taking place in such a device can be presented in the form of a flowchart shown in **Figure 1**. We will consider the simulation flowchart [1–3].

Unit 1 simulates a background-target situation in object space. Here, the number of point emitters "n" is set as spatial δ-functions, their coordinates α_i, β_i, and their radiation characteristics are stellar values, mv for stars and the radiation force I for mobile objects, including those irradiated by the sun.

The background is modeled based on initial data on its brightness at each point. The background emission force at the point is defined as:

$$I_\Phi = B\frac{\omega_1\omega_2}{NM}L^2 \tag{1}$$

where:
ω_1 is the angular field along the axis "x," rad;
ω_2 is angular field along the axis "y," rad.;
M is the number of matrix pixels along the "x" axis;
N is the number of matrix pixels along the y axis;

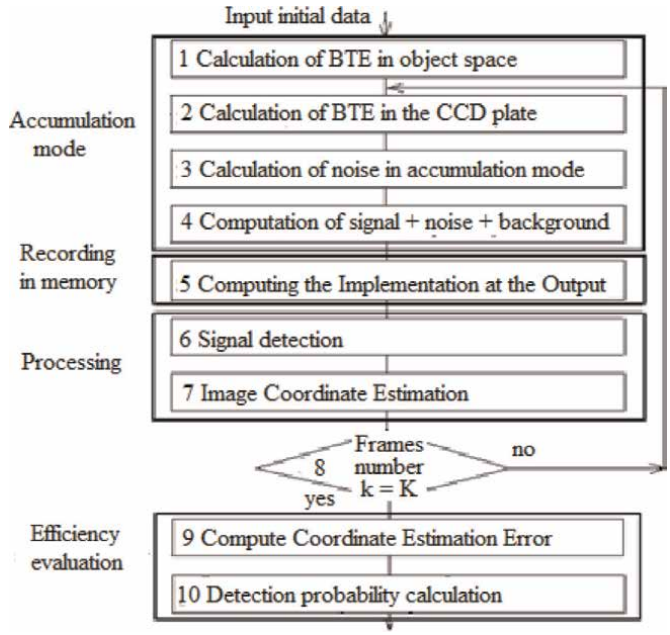

Figure 1.
Simulation flowchart.

L is range to objects space (range to target), m; and
B is the brightness of the background at this point.

Calculation sequence.

(1) Calculation of photodetector diagonal d

$$d^2 = (M\Delta x)^2 + (N\Delta y)^2 \tag{2}$$

(2) Focal length of the lens

$$f' = d/(2\,tg\,\omega), \tag{3}$$

where, ω: angular field of the lens, rad.

(3) Calculation of ω_1,ω_2

$$\omega_1 = 2\arccos\left(\frac{f'}{\sqrt{(M\Delta x/2)^2 + f'^2}}\right) \tag{4}$$

$$\omega_2 = 2\arccos\left(\frac{f'}{\sqrt{(N\Delta y/2)^2 + f'^2}}\right)$$

Then, the background is calculated by the formula (1).

In block 2, the signal from the point objects and the signal from the background in the plane of the photodetector matrix are simulated. We will simulate only those areas of the matrix where the useful signal is located. Assume that the region of the matrix

where the useful signal is generated, and the background is 16 × 16 pixels. This is based on the experience of developing an OEP with a CCD matrix ОЗД-1 (optical star sensor) by the Institute of Space Research of the Russian Academy of Sciences. Such submatrices must be "n." We determine the coordinates of the pixel where the useful signal from the nth emitter enters

$$x_n = f' \operatorname{tg} \alpha_n; y_n = f' \operatorname{tg} \beta_n \tag{5}$$

or in number of pixels

$$M1 = x_n/\Delta x; N1 = y_n/\Delta y$$

M1, N1: radiator coordinates in matrix pixels counted from the matrix center.

If the beginning of the reference is taken as the upper left corner of the matrix, then we get

$$\begin{aligned} M2 &= M/2 + M1 \\ N2 &= N/2 - N1 \end{aligned} \tag{6}$$

Thus, the final formulas for calculating the coordinates of the nth emitter in the plane of the matrix take the form.

$$\begin{aligned} M2 &= M/2 + f' \operatorname{tg}\alpha_n/\Delta x \\ N2 &= N/2 - f' \operatorname{tg}\beta_n/\Delta y \end{aligned} \tag{7}$$

The main beam from the point source is projected to this point.

Now you need to form a submatrix occupied by the image of the point source. As mentioned above, such a submatrix should occupy 16 × 16 pixels. The value of the useful signal from the radiation force source I in the pixels is defined as:

$$Q[i, j] = \frac{\pi D^2}{4L^2} \tau \chi[i, j] \cos^4 \omega_n \frac{I(\lambda) \eta(\lambda_{cp}) t \Delta\lambda \lambda_{cp}}{hC}, \tag{8}$$

where

D: diameter of the inlet pupil of the optical system, m;

τ: lens transmission, rel. unit;

χ [i, j] is a factor that takes into account the share of energy accounted for 1 pixel, rel. units;

I (λ): source radiation force, W/(cf. μm);

$\eta(\lambda_{cp})$: quantum efficiency, rel. unit;

Δλ: spectral range, m;

t: accumulation time, s;

h: Planck constant, J × s; and

C: speed of light, m/s;

Signals from stars are calculated by formulas:

$$\begin{aligned} \text{for G0} &: Q[i, j] = 0,25 \pi t D^2 \tau \chi[i, j] \cos^4 \omega_n 10^{4,423 - 0,4\, m_v} \\ \text{for B3V} &: Q[i, j] = 0,25 \pi t D^2 \tau \chi[i, j] \cos^4 \omega_n 10^{4,411 - 0,4\, m_v} \end{aligned} \tag{9}$$

Calculation sequence

1. Calculation of coefficients χ [i, j]

   The image of the point source is projected onto the submatrix of the 4 × 4 pixel. The main beam hits the point with coordinates M2, N2 or in the coordinates of the submatrix given in **Figure 2** for one of the pixels: i = 2, j = 2; i = 3, j = 2; i = 2, j = 3; i = 3, j = 3.

   The total signal from the PSF image equal to I_Σ is determined as the sum of the signals from the polychromatic light beams of the entire PSF along the "x" and "y" axes.

$$I_\Sigma = \sum_y \sum_x \Delta I,$$

   where ΔI is the number of rays (or the proportion of illumination) that falls on the elementary resolution cell of the PSF (it is 1.5 ÷ 3 μm, sometimes 5 μm).

   The share of illumination per pixel will be

$$I1[i,j] = \int_{\Delta x}\int_{\Delta y} I(x,y)\,dxdy = \sum_{\Delta x}\sum_{\Delta y} \Delta I,$$

   thus

$$\chi[i,j] = \frac{\sum_{\Delta x}\sum_{\Delta y}\Delta I}{\sum_x \sum_y \Delta I} = \frac{I1[i,j]}{\sum_x \sum_y \Delta I} \tag{10}$$

2. Calculation cos ωn

$$\cos \omega_n = \frac{f'}{\sqrt{x_n^2 + y_n^2 + f'^2}} \tag{11}$$

3. Calculation of useful signal value in submatrix pixels 4 × 4 from the radiator with radiation force I taking into account lens transmission

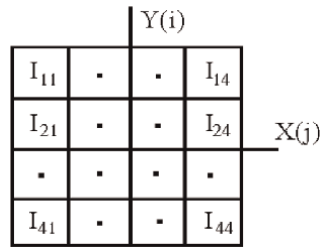

Figure 2.
Radiation distribution by submatrix.

$$Q[i,j] = \frac{\pi D^2 \tau\chi[i,j] \cos^4\omega_n I \eta t \Delta\lambda\lambda}{4L^2 hC} \tag{12}$$

4. Background calculation

Background calculated on 16 × 16 pixels submatrix

$$Q[k,l] = \frac{\pi D^2 \tau\chi 1[k,l] \cos^4\omega[k,l] I_{TM}[k,l] \eta t \Delta\lambda\lambda}{4L^2 hC} = \frac{\pi D^2 \tau \cos^4\omega[k,l] \eta t \Delta\lambda\lambda}{4L^2 hC} \times$$
$$\times\{\chi 1[k-1,l-1]I[k-1,l-1] + \chi 1[k,l-1]I[k,l-1] + \chi 1[k+1,l-1]I[k+1,l-1] +$$
$$\chi 1[k-1,l]I[k-1,l] + \chi 1[k,l]I[k,l] + \chi 1[k+1,l]I[k+1,l] +$$
$$\chi 1[k-1,l+1]I[k-1,l+1] + \chi 1[k,l+1]I[k,l+1] + \chi 1[k+1,l+1]I[k+1,l+1]\} \tag{13}$$

Unit 3 performs the procedure of generating noise of the CCD matrix of the visible range in the accumulation mode. The mathematical expectation of charge in the pixel will be defined as [3, 4]

$$q[k,l] = \frac{\Delta x \Delta y j_d t}{e} 10^{-2} \tag{14}$$

where j_d: average dark current density, A/cm^2; and
e: charge of the electron, the coulomb (C).
The value of MSE "geometric noise" will be

$$\sigma_\Gamma = \frac{H}{200} q \tag{15}$$

where H is dark current nonuniformity, %.
The implementation of dark current taking into account "geometric noise" will be defined as:

$$q_\Gamma[k,l] = q + \sigma_T \xi \tag{16}$$

where ξ are random numbers (hereinafter referred to as) having a normal distribution density with parameters (0, 1).
The MSE of dark charge fluctuations in the pixel will be calculated by the formula

$$\sigma_{Фл} = \sqrt{q_T} \tag{17}$$

Then, the realization of the dark charge in the pixel will be defined as:

$$q[k,l] = q_T + \sqrt{q_T}\xi_1 \tag{18}$$

Thus, a noise array of 16 × 16 pixels in the signal accumulation mode is to be formed. The implementation of the background signal will be determined similarly.

$$Q_{1Ф}[k,l] = Q_Ф[k,l] + \sqrt{Q_Ф}\xi_2 \tag{19}$$

In block 4, a signal mixture with noise and background is calculated.

Formulas for calculating noise and background implementations were given above. The implementation of the useful signal can be calculated similarly.

$$Q_1[i, j] = Q[i, j] + \sqrt{Q[i, j]}\xi_3 \tag{20}$$

where Q [i, j] is a signal from a star or a point emitter.

Then, the realization of the mixture of signal, noise, and background in each pixel of the matrix 16 × 16, where part of the matrix is occupied by the signal, will be calculated as an additive mixture.

$$Q_2[k, l] = Q_{1Ф}[k, l] + q_1[k, l] + Q_1[i, j] \tag{21}$$

In this case, the signal accumulation process in each nth submatrix

16 × 16 pixels end. Now, it is necessary to calculate the implementation of the signal at the output of the matrix and when writing it to the RAM.

In block 5, the signal implementation at the output of the matrix is calculated.

The value of the signal when transmitting charge to the CCD output, taking into account losses, will be determined as:

$$Q_3[k, l] = [1 - 3(M3 + N3)\varepsilon]Q_2[k, l], \tag{22}$$

where M3 and N3 correspond to indices k and l, respectively, but only in coordinates (column and row numbers) of the entire matrix.

When reading a signal, noise is added to it, the MSE of which is determined by the value

$$\sigma_{сч} = \frac{2}{e}\sqrt{(8/3)KT/g_m f_c}(C_2 + C_3), \tag{23}$$

where

e: charge of the electron,

K: Boltzmann constant, J/k.

T: absolute temperature, deg. K,

g_m: transistor slope, mA/V,

f_c: clock frequency, Hz, and

C2 + C3 = 1÷5 pf.

Then, the implementation of the signal at the output of the reader (before the ADC) will be defined as:

$$Q_4[k, l] = Q_3[k, l]\sigma_{сч}\xi_4 \tag{24}$$

Now, it is necessary to determine the price of one ADC discharge in electrons. It can be calculated as:

$$DN = Q_m/2^b \tag{25}$$

where Q_m: maximum charge that can be accumulated in potential wall (for matrix with volume channel is ~130,000 $\bar{e}$), and

b: number of ADC bits,

Then, the value of the signal after digitization will be determined as:

$$Q_5[k, l] = Q_4[k, l]/DN, \tag{26}$$

wherein Q_5 must be written as an integer.

If Q_5 [k, l] ≥ 2b, you must assign Q_5 [k, l] = 2^b (saturation mode).
Thus, "n" digitized array 16 × 16 pixels to be processed in subsequent blocks will be formed.

Block 6 solves the task of detecting a useful signal. To do this, line-by-line viewing of each of the "n" matrices is carried out. To this end, first, the mathematical expectation of a constant background on the line in the vicinity of the useful signal and the MSE of this value in the rate of arrival of samples and taking into account their accumulation is estimated, that is,

$$EV = \frac{1}{16}\sum\nolimits_{i=1}^{16} Q_4[k, l] \tag{27}$$

$$MSE = \sqrt{\frac{1}{15}\sum\nolimits_{i=1}^{16}(EV - Q_4[k, l])^2} \tag{28}$$

Then, the signal is detected in the following lines by the condition

$$Q_4[k, l] - EV \geq 3MSE \tag{29}$$

If the condition is met, then the corresponding pixel (or line pixels) is registered, if not, then again, after passing the line, the expected value (EV) and MSE are refined and again the condition (29) is checked for the next line. In this way, all lines are viewed and all item numbers where condition (29) is met are recorded, as well as the item where the signal is maximum.

The next step is to determine the sub-array 4 × 4 of the pixels occupied by the useful signal.

Set the submatrix to Q_m as shown in **Figure 3** and find the sum signal for all submatrix pixels.

$$QZUM = \sum_{i=1}^{4}\sum_{j=1}^{4} Q_4[i, j] \tag{30}$$

Then, we move the window one pixel to the right and again calculate the sum according to formula (30) and compare it with the previous one. If it is larger, then we remember it, if it is smaller, we leave it first. From this position, the window is shifted

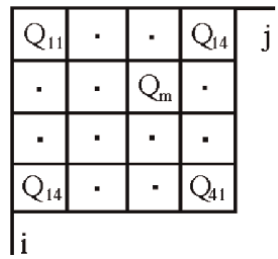

Figure 3.
Charge distribution in submatrix.

one pixel down and again we find the sum according to formula (30) and compare it with the sum that is recorded. If the new amount is larger, then we remember it and the new position of the window. The last position of the window is a shift by one pixel to the left, again calculating the sum, comparing it with the recorded one, and if the resulting sum is larger, then its record, if not, then the previous largest sum remains. Thus, the signal selection (window setting) is completed. Now you need to highlight the "clean" signal. To do this, subtract the mathematical expectation of a constant background from the signal values in the 4×4 pixels submatrix. Thus, a useful signal with zero mathematical expectation in each formed sub-array of 16×16 pixels will be extracted, which is supplied to the unit for estimating the coordinates of the obtained images.

The following quasi-optimal methods are used to estimate the coordinates of the images in block 7.

1. Estimation of image coordinates by energy center (method "weighings").

2. Modified "weighing" method.

3. Finite difference method.

4. Least squares estimation.

5. An iterative method for estimating a Kalman filter-based mismatch.

6. Nine-pixel algorithm.

Methods 1 ÷ 5 assume the formation of one-dimensional lines along the axes "x" and "y." Method 6 involves working with the original submatrix without converting it into one-dimensional signals. One-dimensional rulers from the submatrix are formed as shown in **Figure 4**. Then, expressions for estimating the coordinate of the image (similar to for) using methods 1 ÷ 4 have the form [3, 4].

$$\hat{x}_m = \frac{\Delta x}{2} \frac{(-3Q_1 - Q_2 + Q_3 + 3Q_4)}{(Q_1 + Q_2 + Q_3 + Q_4)} \tag{31}$$

$$\hat{x}_m = \frac{\Delta x}{2} \frac{\left(-3Q_1^2 - Q_2^2 + Q_3^2 + 3Q_4^2\right)}{\left(Q_1^2 + Q_2^2 + Q_3^2 + Q_4^2\right)} \tag{32}$$

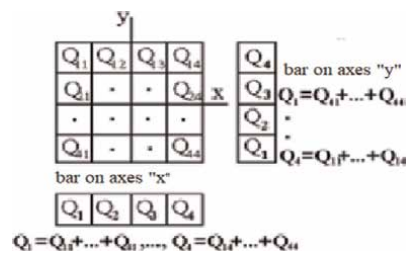

Figure 4.
Lines of readings by axes.

But for certainty that the signal Q_{23} is maximum (although it may be another pixel), then the finite difference method has the form

$$\begin{aligned} &\text{a)}\ \hat{x}_m = \Delta x\left(\frac{Q_2 - Q_3}{Q_2 - 2Q_3 + Q_4}\right) \\ &\text{b)}\ \hat{x}_m = \Delta x\left(\frac{Q_2 - Q_4}{Q_2 - 2Q_3 + Q_4}\right) \\ &\text{c)}\ \hat{x}_m = \Delta x\left(\frac{Q_3 - Q_4}{Q_2 - 2Q_3 + Q_4}\right) \end{aligned} \tag{33}$$

where the expressions (a)–(c) are derived from the interpolation formulas of Newton, Newton-Bessel, and Newton-Stirling.

$$\hat{x}_m = \frac{3\Delta x}{2}\operatorname{arctg}\left(\frac{-Q_1 - Q_2 + Q_3 + Q_4}{-Q_1 + Q_2 + Q_3 - Q_4}\right) \tag{34}$$

The mismatch between the reference function and the x-axis ruler formed from the image can be determined as follows (the algorithm for calculating the reference function will be given below). For this, an analytical description of the distribution of samples over the ruler in the form of a truncated Fourier series can be used.

$$Q(x) = a_0 + a_1 \sin\frac{\pi x}{2\Delta x} + a_2 \cos\frac{\pi x}{2\Delta x},$$

where

$$\begin{aligned} a_0 &= \frac{1}{4}(Q_{x1} + Q_{x2} + Q_{x3} + Q_{x4}); \\ a_1 &= \frac{\sqrt{2}}{4}(-Q_{x1} - Q_{x2} + Q_{x3} + Q_{x4}); \\ a_2 &= \frac{\sqrt{2}}{4}(-Q_{x1} + Q_{x2} + Q_{x3} - Q_{x4}) \end{aligned}$$

Such a description makes it possible to normalize the reference function and generated ruler, as well as determine the required mismatches at points. $x_1 = -1,5\Delta x; x_2 = -0,5\Delta x; x_3 = 0,5\Delta x; x_4 = 1,5\Delta x$ Consider the normalization operation first. To do this, you need to find the position and value of the maximum Q (x). In accordance with (34), the maximum position is defined as:

$$\hat{x}_m = \frac{2\Delta x}{\pi}\operatorname{arctg}\left(\frac{-Q_{x1} - Q_{x2} + Q_{x3} + Q_{x4}}{-Q_{x1} + Q_{x2} + Q_{x3} - Q_{x4}}\right),$$

thus

$$Q_m = a_0 + a_1 \sin\frac{\pi\hat{x}_m}{2\Delta x} + a_2 \cos\frac{\pi\hat{x}_m}{2\Delta x},$$

and the normalized values of the generated reference function ruler are defined as:

$$Q_{x1}, = \frac{Q_{x1}}{Q_m}, \ldots, Q_{x4H} = \frac{Q_{x4}}{Q_m}; F_{1H} = \frac{F_1}{F_m}, \ldots, F_{4H} = \frac{F_4}{F_m}$$

Further, on newly formed rulers $Q_{x1H}, \ldots, Q_{x4H}$; $F_{1H}, \ldots, F_{4H}$ where F_i is the reference function sample, you must define new coefficients $\mathbf{a}_{0H}, \mathbf{a}_{1H}, \mathbf{a}_{2H}$ for the reference function and the signal implementation being processed. As a result of these procedures, we will obtain those inconsistencies $\delta x_1 \div \delta x_4$ that can be defined as:

$$\delta x_1 = \frac{\Delta F_1}{\left(\frac{\partial F}{\partial x}\right)_{x=-1,5\Delta x}}, \ldots, \delta x_4 = \frac{\Delta F_4}{\left(\frac{\partial F}{\partial x}\right)_{x=1,5\Delta x}},$$

where

$$\Delta F_1 = F_{1H} - Q_{x1H}, \ldots, \Delta F_4 = F_{4H} - Q_{x4H}.$$

Derivatives in the denominator are defined as:

$$\frac{\partial F}{\partial x} = a_1 \frac{\pi}{2\Delta x} \cos \frac{\pi x}{2\Delta x} - a_2 \frac{\pi}{2\Delta x} \sin \frac{\pi x}{2\Delta x}$$

and will have values at the appropriate points

$$\left(\frac{\partial F}{\partial x}\right)_{x=-1,5\Delta x} = \frac{\pi}{2\Delta x}\left(-a_1\frac{\sqrt{2}}{2} + a_2\frac{\sqrt{2}}{2}\right) = \frac{\pi}{4\Delta x}(F_{2H} - F_{4H});$$
$$\left(\frac{\partial F}{\partial x}\right)_{x=-0,5\Delta x} = \frac{\pi}{4\Delta x}(F_{3H} - F_{1H}); \left(\frac{\partial F}{\partial x}\right)_{x=0,5\Delta x} = -\left(\frac{\partial F}{\partial x}\right)_{x=-1,5\Delta x};$$
$$\left(\frac{\partial F}{\partial x}\right)_{x=1,5\Delta x} = -\left(\frac{\partial F}{\partial x}\right)_{x=-0,5\Delta x}$$

Now you need to process the presented series of values in order to obtain an assessment $\delta \hat{x}$. The definition of the latter can be produced using the Kalman filter, which in our case has the form [3]

$$\begin{aligned} &P^*(k+1) = \tilde{P}(k) \\ &B(k) = P^*(k)/\left[P^*(k) + \Delta^2\right] \\ &\tilde{P}(k) - [1 - B(k)]P^*(k) \\ &\delta\hat{x}(k) = \delta\hat{x}(k-1) + B(k)[\delta x(k) - \delta\hat{x}(k-1)] \end{aligned} \tag{35}$$

where Δ^2: variance of systematic (or methodical) error definitions δx, in our case does not exceed $(0.05\ \Delta\ x)^2$; and

P^* is in the general case a matrix of dispersions, and in our case the variance of random error of "measurement" of value δx.

It is determined in the real device by both external interference and internal noise. Since we are now considering the system without interference, the random error is determined only by the error of calculating and rounding the signal values. In (35), P^* is a nominal value and is defined as:

$$P^*(k) = \left[\left(\frac{\sigma_\Phi}{Q_m}\right)\left(\frac{\partial F}{\partial x}\right)_k^{-1}\right]^2,$$

where σ_ϕ is the MSE of interference error.

Note that $P^* \sim$ is 2 orders of magnitude less than Δ^2. That will do to calculate the first B value of the filter gain.

Algorithmic calibration of optoelectronic system

The essence of the algorithmic calibration is to estimate the impulse response or reference function of the primary path of the meter. The main stages of a stellar sensor-type EPR, which are as follows:

1. A portion of the starry sky is shot so as to register as many stars as possible in one frame throughout the field of the device, and this data is recorded in the computer memory.

2. The corresponding method is used to subtract the background,

normalizing, bring images to a common origin, and average them. If you are performing an algorithmic calibration, you can obtain both a one-dimensional and a two-dimensional reference function, consider the calibration procedure in more detail.

Obtaining a one-dimensional reference function

As mentioned above, OEI with CCD as the first step must register a piece of a starry sky. Received frame representing a digitized signal matrix is recorded in computer memory. The signal from each individual star, which is an ideal point source, is nothing more than a function of scattering the point of the lens. Moreover, the latter has already been spatial sampled and digitized. The initial step of processing is to determine the mathematical expectation of the background and variance (or MSE) of the background (this procedure has already been described above).

Applicable to 16×16 pixels fragments. First, the sub-array 4×4 of the pixels occupied by the useful signal from the stars is eliminated, then the mathematical background expectation and background or noise variance are determined in a known manner. Further, from the signals (samples) of the 4×4 submatrix occupied by the useful signal, the background signal is subtracted and a new submatrix containing only the useful signal and random noise with zero mathematical expectation is obtained.

The next step of processing is the formation of lines along the axes "x," "y," each of which contains 4 pixels. This procedure is described above. Since the position of the datum function relative to the coordinate center of the 4×4 submatrix of the pixel is random, it is necessary to bring it to the coordinate center of the submatrix. For this, the above analytical description can be used, then the operation of bringing the reference function to the center of the submatrix is reduced to calculating derivatives and determining corrections ΔF_k to F_k at points

$$x_1 = -1,5\Delta x; x_2 = -0,5\Delta x; x_3 = 0,5\Delta x; x_4 = 1,5\Delta x,$$

that is,

$$\Delta F_1 = \hat{x}_m \left(\frac{\partial F}{\partial x}\right)_1; \Delta F_2 = \hat{x}_m \left(\frac{\partial F}{\partial x}\right)_2; \Delta F_3 = \hat{x}_m \left(\frac{\partial F}{\partial x}\right)_3; \Delta F_4 = \hat{x}_m \left(\frac{\partial F}{\partial x}\right)_4,$$

where $\hat{x}_m$ and $\left(\frac{\partial F}{\partial x}\right)_k$ defined by the expressions given above, that is,

$$\left(\frac{\partial F}{\partial x}\right)_1 = \frac{\pi}{4\Delta x}(Q_{x2} - Q_{x4}); \left(\frac{\partial F}{\partial x}\right)_2 = \frac{\pi}{4\Delta x}(Q_{x3} - Q_{x1});$$

$$\left(\frac{\partial F}{\partial x}\right)_3 = -\frac{\pi}{4\Delta x}(Q_{x2} - Q_{x4}); \left(\frac{\partial F}{\partial x}\right)_4 = \frac{\pi}{4\Delta x}(Q_{x3} - Q_{x1});$$

Then, considering $\hat{x}_m$ and $\left(\frac{\partial F}{\partial x}\right)_k$ we obtain

$$\begin{aligned}
\Delta F_1 &= \left(\frac{Q_{x2} - Q_{x4}}{2}\right)\text{arctg}\ \left(\frac{-Q_{x1} - Q_{x2} + Q_{x3} + Q_{x4}}{-Q_{x1} + Q_{x2} + Q_{x3} - Q_{x4}}\right) \\
\Delta F_2 &= \left(\frac{Q_{x3} - Q_{x1}}{2}\right)\text{arctg}\ \left(\frac{-Q_{x1} - Q_{x2} + Q_{x3} + Q_{x4}}{-Q_{x1} + Q_{x2} + Q_{x3} - Q_{x4}}\right) \\
\Delta F_3 &= \left(\frac{Q_{x4} - Q_{x2}}{2}\right)\text{arctg}\ \left(\frac{-Q_{x1} - Q_{x2} + Q_{x3} + Q_{x4}}{-Q_{x1} + Q_{x2} + Q_{x3} - Q_{x4}}\right) \\
\Delta F_4 &= \left(\frac{Q_{x1} - Q_{x3}}{2}\right)\text{arctg}\ \left(\frac{-Q_{x1} - Q_{x2} + Q_{x3} + Q_{x4}}{-Q_{x1} + Q_{x2} + Q_{x3} - Q_{x4}}\right)
\end{aligned} \tag{36}$$

Corrected values of the given reference function are determined by expressions

$$F'_1 = F_1 + \Delta F_1, \ldots, F'_4 = F_4 + \Delta F_4$$

and the maximum TFT value at point x = 0 is

$$F'_{max} = \frac{1}{4}\left(F'_1 + F'_2 + F'_3 + F'_4\right) + \frac{\sqrt{2}}{4}\left(-F'_1 + F'_2 + F'_3 - F'_4\right) \tag{37}$$

To get the average of the reference function the frame (and, accordingly, the angular field) should be normalized for each image, which is reduced to dividing F'_i by F'_m and calculating the average value $\overline{F'_i}$ of all L images of stars in the frame along each coordinate axis

$$\overline{F'_{i,j}} = \frac{1}{L}\sum_{l=1}^{L}\left(F'_{i,j}/F'_{mx,y}\right); i, j = 1, 2, 3, 4 \tag{38}$$

Thus, we get normalized and centered, relative to the origin, submatrices of the values of the datum function along the axes "x" and "y." For ease of calculation, a suitable analytical description may be adopted as the reference function. Thus, for example, to describe the reference function of the OEI ОЗД-1 (optical star sensor), Student distribution is the most suitable.

$$F(x) = \frac{2}{\pi\sqrt{3}}\left[1 + \frac{(x - x_0)^2}{3}\right]^{-2}$$

The distribution of illumination over the image of the point emitter, as a rule, has one maximum, so it is often described by the Gaussian of rotation. Based on these representations, an algorithm can be obtained for estimating the parameters of such a Gaussian: The position of the maximum $\hat{x}_m$, $\hat{y}_m$ and the parameters of the distribution σ_x, σ_y of taking into account the averaging by samples within the submatrix occupied by the useful signal. Suppose that the envelope of the distribution of counts over the image can be described by a two-dimensional gauss function [4]

$$Q(x,y) = Q_0 \exp\left[-\frac{(x-\hat{x}_m)^2}{2\sigma_x^2} - \frac{(y-\hat{y}_m)^2}{2\sigma_y^2}\right]$$

where Q_0: signal amplitude;
$\hat{x}_m, \hat{y}_m$: maximum position (note that it is in.
within pixel Q_{33}—**Figure 5**);
σ_x,σ_y: distribution parameters.
Expressions for image coordinate estimates have the form

$$\hat{\sigma}_x^2 = 3/\ln\left(\frac{Q_{23}^2 Q_{33}^2 Q_{43}^2}{Q_{22}Q_{24}Q_{32}Q_{34}Q_{42}Q_{44}}\right)$$

$$\hat{x}_m = \frac{\hat{\sigma}_x^2}{6}\ln\left(\frac{Q_{24}Q_{34}Q_{44}}{Q_{22}Q_{32}Q_{42}}\right) \quad (39)$$

$$\hat{\sigma}_y^2 = 3/\ln\left(\frac{Q_{32}^2 Q_{33}^2 Q_{34}^2}{Q_{24}Q_{44}Q_{23}Q_{43}Q_{22}Q_{42}}\right)$$

$$\hat{y}_m = \frac{\hat{\sigma}_y^2}{6}\ln\left(\frac{Q_{22}Q_{23}Q_{24}}{Q_{42}Q_{43}Q_{44}}\right)$$

Estimates of the formulas given will be obtained in the matrix decomposition pixels. It should also be noted here that the resulting values $\hat{x}_m, \hat{y}_m$ will differ from the estimates for previous algorithms by 0.5 pixel for each coordinate since the center of the coordinate system is placed in the center of the pixel.

Block 9 is intended for the calculation of error of coordinate estimation. Its Δx_m value is defined as follows. Sets the original position of the image. It calculates the value of the signal in the pixels taking into account external and internal interference within the image, according to the modeling algorithms given above. The original image position values x_0, y_0 range from $-0{,}5\Delta x$ to $+0{,}5\Delta x$. Further, a values $\Delta x_m = x_0 - \hat{x}_m$, $\Delta y_m = y_0 - \hat{y}_m$ are determined from the expressions for estimating coordinates. Thus, at least 250 implementations in each position of the image are processed and the law of distribution of this error is constructed, by which its parameters can be determined.

In the last block 10, a posteriori estimation of the probability of detecting a signal in one frame for each image is made [5]. The calculation sequence is as follows. We set the relative detection threshold for each of the "n" images z_t = 3 MSE,

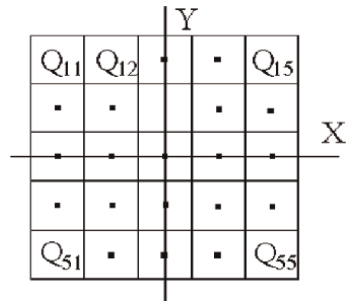

Figure 5.
Distribution of signals caused by the image over the matrix.

where MSE is the mean square deviation calculated in block 7.

Next, we find the signal-to-noise ratio ρ in the pixel containing the maximum signal within the image

$$\rho = \frac{Q_m[i, j]}{MSE},$$

where Q_m is the maximum count (minus the constant background) in the submatrix. By these values, we find $z_t - \rho = z_0$

$$\Phi(z_0) = \frac{1}{\sqrt{2\pi}} \int_0^{z_t} e^{-\frac{\theta^2}{2}} d\theta, \tag{40}$$

that allows to calculate probability of signal detection

$$P_{обн} = 0,5[1 - 2\Phi(z_0)] \tag{41}$$

each of the "n" images in the frame.

The probability of a false alarm will be determined by the expression

$$P_{лт} = 0,5 - \Phi(z_t) \tag{42}$$

This procedure ends the process of simulating the primary processing of still images in the ECU with a matrix photodetector.

Replace the entirety of this text with the main body of your chapter. The body is where the author explains experiments, and presents and interprets data of one's research. Authors are free to decide how the main body will be structured. However, you are required to have at least one heading. Please ensure that either British or American English is used consistently in your chapter.

3. Conclusion

The studies carried out in this work produced the following results. The method of modeling the angular OEI with CCD and assessing its accuracy and detection characteristics, as well as assessing the requirements for the parameters of such devices, including.

- External input impact model;
- EIA internal interference model;
- Model of operation of the OEI pixels;
- Model of processes of detection, extraction of useful signal, and estimation of its parameters.

Author details

Viktor Pachkov
Cavalia: Illumi, Toronto, Canada

*Address all correspondence to: viktor.pachkov@gmail.com

IntechOpen

References

[1] Pashkov V. On-board optoelectronic measuring system. Lightning Source Incorporated. 2022;**2022**:240. DOI: 10.31772/2587-6066-2019-20-4-416-422

[2] Pashkov V. On-board Optoelectronic Measuring System. Petersburg, Russia; 2021. p. 263. DOI: 10.31772/2587-6066-2019-20-4-416-422

[3] Pashkov V. On-board Optoelectronic Measuring System. Saarbrucken, Germany: Palamarium Academic Publishing/OmniScriptum GmbH&Co; 2014. p. 253. DOI: 10.31772/2587-6066-2019-20-4-416-422

[4] Pashkov V. Modelling of the optical-electronic device with the matrix photodetector. Danish Scientific Journal. 2017;**5**(119):85-101

[5] Pashkov VS. The signal detection simulation in the optical -electronic devices with matrix photodetectors. Znanstvena Misel Journal. 2017;**10**(104): 91-95

Chapter 5

Advances in Colloidal Quantum Dot Laser Diodes

Jie Lin, Geng He, Yun Hu and Jingsong Huang

Abstract

Colloidal quantum dots possess distinctive optoelectronic properties, rendering them a promising material for gain applications. Additionally, colloidal quantum dot lasers can emit light over a broad range of wavelengths, spanning from the near-infrared to the visible spectrum, which makes them suitable for various applications. The potential impact of colloidal quantum dot lasers on various industries and technologies cannot be overstated. Their continued development and optimization represent an exciting area of research that could revolutionize numerous fields. The review examines the challenges related to achieving lasing with colloidal quantum dots, discusses potential approaches to overcome these challenges, and surveys the latest advances made toward achieving this objective.

Keywords: colloidal quantum dot, optical microcavity, low threshold, laser, electrically pumped

1. Introduction

Since its first demonstrations in the early 1960s [1], the laser has become a crucial tool for research, but available materials can not cover all visible light emissions. Materials that produce optical gain and sustain laser emission with tunable wavelengths would spark research interest [2–4]. Colloidal quantum dots (CQDs) are promising laser materials due to their photophysical properties, solution processability, and production capability. They offer advantages over epitaxial and dry processing methods, simplifying device preparation and reducing production costs. CQDs offer advantages of both inorganic and organic materials, allowing large-area and low-cost solution processing in device fabrication, making them a typical example of a solution-processable laser device [5]. The unique technological advantages of CQD lasers have been widely acknowledged since they first appeared [3], including on-chip optical interconnects [6, 7] and integrated photonic circuits [8, 9], wearable devices [10, 11] and advanced medical imaging and diagnostics [12], clandestine markers [13], and many others. Extensive research efforts have led to significant progress in achieving CQD lasing with both optical and electrical pumping. Advances include continuous-wave optical pumping [14], optical gain in electrically-driven QLEDs [15], on-chip integrated CQD lasers [8], and dual-function devices combining optically pumped lasing and electrically-driven LED [16].

However, despite these advances, CQD lasers are still in the stage of laboratory demonstrations. In most reported studies of CQD lasing, shape control is one of the primary strategies used to suppress Auger recombination and reduce the laser threshold. Many materials scientists have utilized various strategies from the perspective of designing and synthesizing colloidal quantum dots to suppress Auger recombination, enhance the emission efficiency of biexcitons and multiexcitons, and achieve lasing using colloidal quantum dots with different shapes, for example, spherical CQDs [17], hetero-CQDs of type I [18], type II [19] and quasi-type II [20], nanorods [21], dot-in-rods [22], nanoplatelets [23], hetero-NPLs [24], and cube-shaped perovskite CQDs [25]. Relevant studies have shown that increasing the volume of nanomaterials can effectively reduce the threshold [26, 27]. At present, continuously graded quantum dots (cg-QDs) are considered ideal laser gain materials because they can suppress Auger recombination by eliminating sharp discontinuities in the confinement potential [28].

CQD laser presents challenges due to the need for a high-quality feedback structure or optical cavity [29]. Although CQD lasers have been achieved using various cavity designs, research on this topic is not as systematic as the methods proposed to suppress Auger decay. The optical gain threshold of CQDs is still too high for practical applications, and there are still key issues that need to be addressed when coupling CQDs with optical resonators. This chapter focuses on the development of lasers based on different cavity designs, discussing the working mechanisms in optically pumped CQD lasers and the key factors influencing the performance of different optical resonators. It also presents progress made in developing high current density light-emitting diodes (LEDs) using various strategies and discusses the challenges and future development of electrically pumped CQD lasers.

2. CQD lasing with various optical resonators

Current optoelectronic technology relies on expensive and rigid epitaxially grown semiconductors, while CQDs offer tunable optical bandgap from UV to mid-IR, cost-effective processing, substrate independence, and potential long-term stability. This creates an opportunity for CQDs to revolutionize the field of laser-based optoelectronics [29]. Therefore, CQDs are compatible with nearly all types of cavity architectures [30].

The resonator cavity is essential for optical feedback in light amplification. Resonator design determines resonant modes and output beam characteristics, making it crucial for high-quality, low-threshold CQD laser development. Resonators come in various forms and shapes, ranging from simple Fabry-Perot cavities to more complex geometries that require complex theories and precise preparation facilities. Examples of resonator geometries include planar distributed Bragg reflector (DBR) cavities, distributed feedback (DFB), whispering gallery modes (WGM) cavities of different geometries, microspheres, microdiscs, photonic crystals, etc. (as shown in **Figure 1**). Among them, DFB and DBR resonators are the most widely used architectures for CQD lasers. Each of these geometries has unique properties that affect their lasing performance.

Lasing phenomena have been observed in various optical structures for CQDs, including cylindrical [31–33], spherical [34, 35], and microring [36] WGMs, as well as DFB [14, 16–18, 37–42], F-P [43, 44], and VCSELs [45, 46]. **Table 1** below summarizes the performance parameters of CQD lasers in various optical structures since

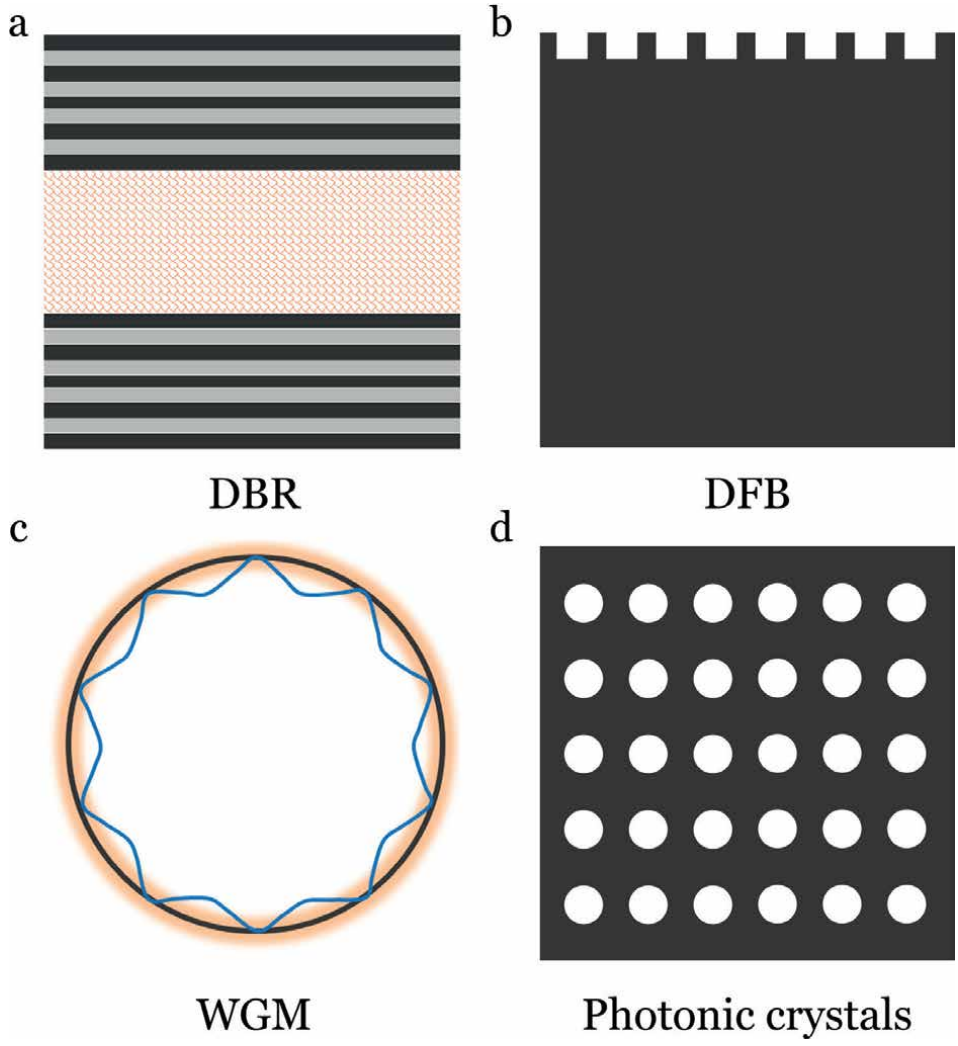

Figure 1.
Resonator structures used for CQD lasers. (a) DBR cavities. (b) 1D DFB gratings. (c) WGM cavities. (d) Photonic crystals.

Materials	Optical structure	Threshold	Wavelength	Pump source	Publication date	Ref.
CdSe/ZnS	WGM (Cylindrical)	1.25 mJ/cm^2	~614 nm	400 nm 100 fs	2002	[31]
CdSe/ZnS	WGM (Cylindrical)	3 mJ/0.75 mJ	547/626 nm	532 nm	2002	[32]
CdSe/ZnS	DFB	1 uJ	583-625 nm	400 nm 100 fs	2002	[37]
CdSe/CdZnS	WGM (spherical)	0.74 mJ/cm^2	669 nm	400 nm 100 fs	2005	[34]
CdSe/ZnS	Fabry-Perot (Self-assembled)	3 mJ/cm^2	614 nm	390 nm 150 fs	2010	[43]

Materials	Optical structure	Threshold	Wavelength	Pump source	Publication date	Ref.
InP/ZnS	DFB	2 mJ/cm^2	616 nm	400 nm 80 fs	2011	[17]
CdSe/ZnS	Flexible DFB	4 mJ/cm^2	610–640 nm	355 nm 5 ns	2011	[38]
CdSe/Zno.5 Cdo.5S CQD	VCSEL (Combined)	60 uJ/cm^2	620 nm	400 nm 100 fs	2012	[45]
CQD	Flexible DFB	~500 uJ/cm^2	607 nm	355 nm 5 ns	2014	[39]
CdSe/ZnCdS	2D DFB	120/280/330 uJ/cm^2	610/575/ 455 nm	355 nm/ 532 nm 0.4 ns	2014	[40]
CdSe/CdS	VCSEL (Combined)	2.49 mJ/cm^2	597–603 nm	800 nm 120 fs	2014	[46]
CdZnS/ZnS	WGM (Cylindrical)	25.2 mJ/cm^2	597–603 nm	385 nm 5 ns	2015	[33]
CdSe/CdS	Fabry-Perot (Self-assembled)	10 uJ/cm^2	632 nm	400 nm 70 fs	2015	[44]
CdSe/CdS/ZnS	2D-DFB	88 kW/cm^2	~645 nm	442 nm 1.8 us	2015	[41]
CdSe-CdS	2D-DFB	6.4–8.4 kW/ cm^2	~639 nm	CW 442 nm	2017	[14]
CdSe/CdS	WGM (spherical)	10 uJ/cm^2	~638 nm	400 nm 100–200 fs	2018	[35]
CdSe/CdS/ZnS	WGM (microring)	22 uJ/cm^2	610 nm	405 nm 340 fs	2018	[36]
CdSe/CdxZn1-xSe cg-QDs	2D-DFB	9 uJ/cm^2	~628 nm	400 nm 130 fs	2019	[18]
cg CdSe/ CdxZn1-xSe/ZnSeo.5So.5/ ZnS	2D-DFB	5.5 uJ/cm^2	~630.9 nm	400 nm 130 fs	2020	[16]
CdSe/CdxZn1-xSe cg-QDs	2D-DFB	82 uJ/cm^2	~615 nm	343 nm 190 fs	2023	[42]

Table 1.
Representative CQD lasers with various optical structures.

Malko et al. pioneered coating CQD solid films onto the inside wall of microcapillary tubes and claimed the observation of lasing in whispering-gallery modes in 2002. Besides the resonator geometry, other factors can also affect the performance of CQD lasers, such as the quality and uniformity of the gain medium, and the optical coupling efficiency between the gain medium and the resonator.

The DFB structure has proven to be an effective and versatile optical resonator for CQD lasers, with numerous research advances made in recent years, as shown in **Figure 2**. In CQD DFB lasers, the grating structure is typically created by periodic modulation of the refractive index or the gain/loss of the waveguide. This modulation

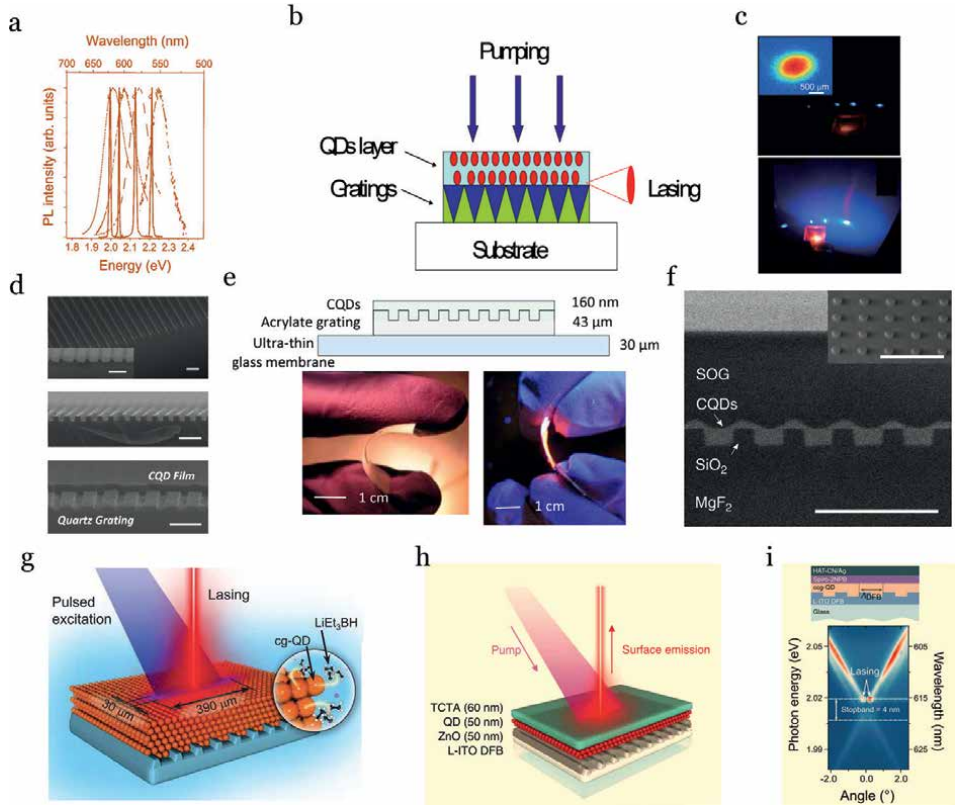

Figure 2.
Representative CQD laser with DFB as optical resonator. (a) Earlier demonstrated DFB CQD laser. (b) DFB laser based on InP/ZnS CQD. (c) Flexible DFB CQD laser. (d) Surface-emitting DFB CQD laser. (e) Wavelength-tunable DFB CQD laser. (f) Quasi-continuous-wave DFB CQD laser. (g) Continuous-wave DFB CQD laser. (h) LED-coupled DFB dual-function devices. (i) DFB-based, high-current density QLED. Reprinted with permission from refs. [16–18, 37–42].

can be achieved through various techniques, such as electron beam, holographic, and nanoimprint lithography. Among various optical structures, DFB is one of the earliest and most popular choices. In a survey of 20 representative articles on CQD lasers, DFB was used as an optical resonator in 10 of them. Adachi et al. and Fan et al. achieved quasi-continuous [41] and continuous wave [14] CQD laser emission using the DFB structure, which further increased its popularity. Due to its compatibility with a QD-LED-like device [16], DFB has become one of the feasible resonator structures for realizing electrically driven devices. The incorporation of DFB into a QD-LED-like device enables the device to operate in both electrical and optical pumping modes. This has led to the development of electrically pumped CQD DFB lasers with low-threshold current densities and high efficiencies. Recent research progress indicates that this hybrid structure can achieve high current injection [42].

From the statistical results in **Table 1**, it can be seen that WGM-based optical resonators are the second most commonly used optical structure for CQD lasers. **Figure 3** shows a comparison between the various geometries based on WGM-based CQD lasers. WGM-based CQD lasers have several advantages, such as low threshold, single-mode operation, high efficiency, and wavelength tunability. The resonant modes in WGM-based cavities are confined by total internal reflection at the curved surface

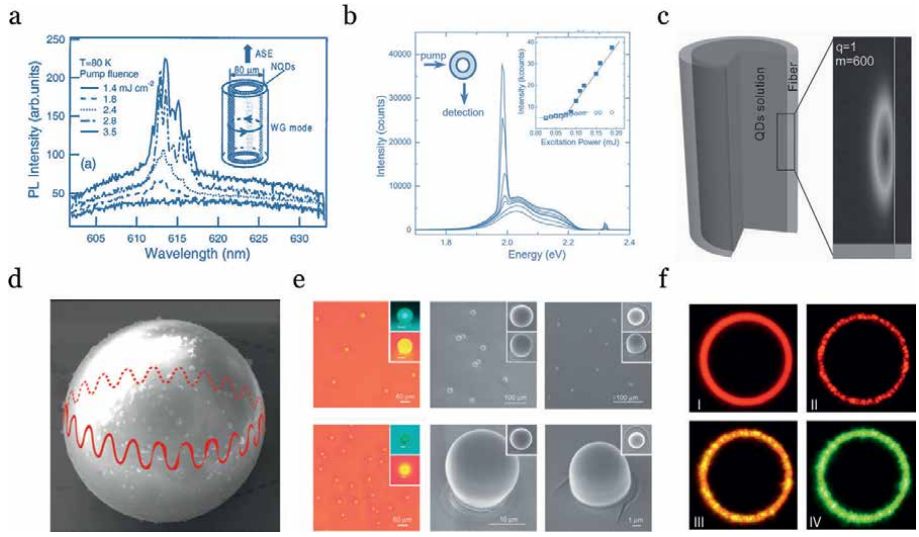

Figure 3.
Representative CQD laser with WGMs as optical resonator. (a) CQD laser with cylindrical microcavities. (b) Lasing from semiconductor quantum rods in a cylindrical microcavity. (c) Quasi-continuous CQD laser with fused silica hollow fibers as the resonators. (d) CQD laser with self-assembled spherical resonators. (e) CQD laser from a microsphere resonator composite. Reprinted with permission from. (f) Active color-controlled CQD ring laser. Reprinted with permission from refs. [31–36].

of the cavity, which allows for high-Q modes and strong light-matter interaction. WGM-based CQD lasers have been demonstrated in various geometries, including cylindrical, spherical, and microring resonators. These resonators can be fabricated using various techniques, such as lithography, etching, and self-assembly. WGM-based CQD lasers are a promising candidate for various applications, such as biosensing, spectroscopy, and on-chip optical communication systems. However, there are also challenges to be addressed, such as the optimization of the cavity geometry for specific applications, the stability of the resonant modes, and the development of efficient injection schemes for electrically pumped WGM-based CQD lasers.

Finally, it is important to also focus on another type of optical resonator structure commonly used in other types of lasers, the Fabry-Perot cavity, also known as the vertical-cavity surface-emitting laser (VCSEL) cavity (**Figure 4**). Compared to WGM-based CQD lasers, VCSELs have a simpler cavity geometry and can be fabricated more easily and with higher yield. They also have excellent beam quality and can emit light perpendicular to the surface. However, VCSELs typically have a higher threshold and lower efficiency. They also suffer from wavelength tuning limitations due to the fixed cavity geometry. It is worth noting that some recent studies have also explored the use of VCSEL-like geometries for CQD lasers, such as the use of sub-wavelength metallic grating structures as the top mirror to enhance the light-matter interaction and reduce the lasing threshold. These structures have shown promising results in terms of high efficiency and wavelength tunability. In summary, while WGM-based CQD lasers and VCSELs have their own advantages and disadvantages, both have demonstrated significant progress in recent years and are expected to continue to play important roles in various fields of photonics and optoelectronics.

Optically pumped CQD lasers have achieved significant progress, and recent advancements have allowed for electrically driven devices, which have expanded the

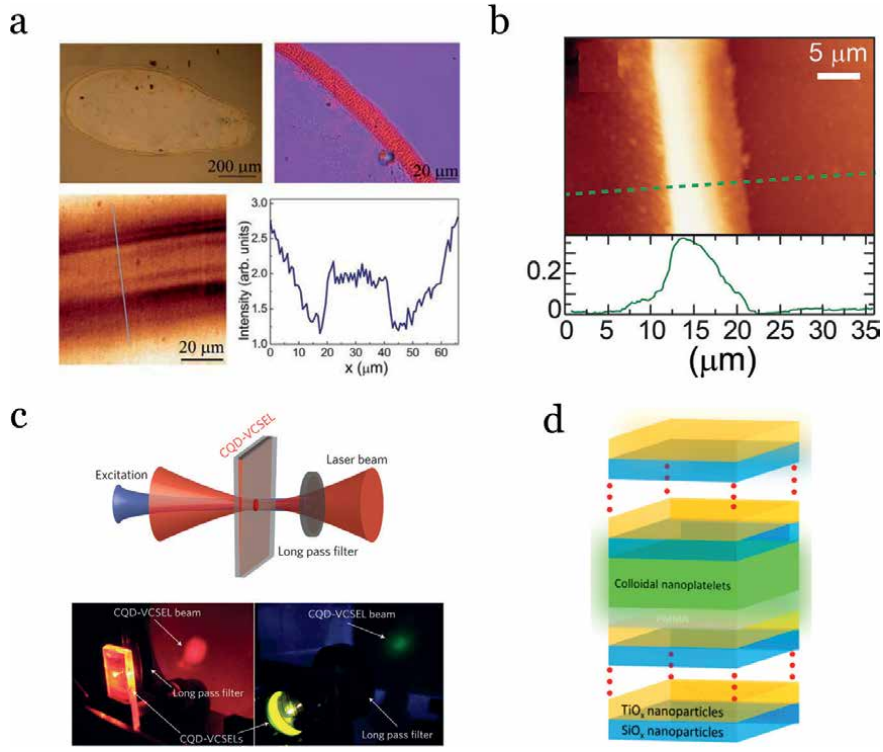

Figure 4.
Representative CQD laser with F-P or VCSEL as optical resonator. (a) Self-assembled F-P CQD resonator laser. (b) Single-mode CQD laser lasing from self-assembled F-P resonator. (c) Optically pumped CQD-VCSELs in red and green. (d) Colloidal nanoplatelets lasing with combining two DBRs together. Reprinted with permission from refs. [33, 43–45].

possibilities of designing optical resonators for CQD lasers to support high-current injection. The choice of resonator geometry and material composition depends on specific application requirements, and integration with other components is crucial. Research is focused on developing efficient cavity structures such as DFB-coupled and planar microcavities, ring resonators, and photonic crystal cavities, among others. The development of suitable optical resonators for high-current injection CQD lasers is an ongoing and challenging area of research but holds promise for various applications. Advances in resonator design, material composition, and integration with other components will continue to drive progress toward practical and efficient CQD laser devices.

3. High-current-density light-emitting diodes (LEDs)

Recent research in CQD laser technology has resulted in advancements in reducing Auger recombination, leading to lower lasing thresholds and continuous wave CQD emission. However, achieving an electrically pumped device, comparable to conventional LED devices, requires a significant reduction in the threshold, which is currently relatively high. To realize an LED-style electrically-pumped CQD laser, new structural designs or electrical-driven methods may help enhance the current

injection of LEDs. Innovative approaches involving materials engineering and device fabrication strategies may also be necessary.

As the device structures of organic light-emitting diodes (OLEDs), CQD light-emitting diodes (QLEDs), and perovskite light-emitting diodes (PeLEDs) are similar, the maximum injection current density of these three types of devices under direct current injection is not significantly different. However, the difference in their luminescence efficiency is substantial. The maximum external quantum efficiency (EQE) of small-molecule OLEDs is usually around 5%, while that of QLEDs and PeLEDs exceeds 20%. This is clearly reflected in the maximum brightness or output power of the devices. Currently, the highest brightness of OLEDs is about 1,500,000 cd/m^2 [47], while that of QLEDs and PeLEDs is 7,646,245 cd/m^2 [48] and 9,800,000 cd/m^2 [28], respectively. While QLED and PeLED technologies are based on OLED technology, CQDs are more suitable for achieving high-performance laser devices in terms of efficiency and output power.

Table 2 summarizes representative high-current density amorphous thin-film LED devices over the past 18 years. The mobility of holes and electrons in high-efficiency LED devices typically ranges from 10^{-4} to 10^{-2}cm^{2}V^{-1} s^{-1}, making it challenging to effectively enhance carrier injection by increasing the mobility of functional layer materials. However, achieving high current injection is crucial for the performance of the LED devices. To this end, it is necessary to address and reduce the negative effects of Joule heating, which can increase device temperature and impact the performance and lifespan of the device. Previous studies have shown that Joule heating can cause OLEDs to overheat by tens or even hundreds of degrees Celsius, even at moderate current densities of only a few amperes per square centimeter due to their high resistivity [58]. Consequently, reducing device resistance and improving its heat dissipation ability are effective methods for mitigating Joule heating. One potential approach is to use a substrate with good thermal conductivity or to perform low-temperature testing. Hajime Nakanotani et al. conducted a study in which OLED devices with identical structures were fabricated on substrates with different thermal conductivities, namely Si, sapphire, and glass [49]. The results showed that the maximum current density achieved in these devices were 1163, 823, and 567 A/cm^2, respectively, indicating that the thermal conductivity of the substrate has a significant impact on Joule heating. Additionally, the implementation of optically pumped CQD lasers at low temperatures is another example of a technique utilized to mitigate Joule heating [37]. By operating the device at a lower temperature, the amount of heat generated due to Joule heating can be reduced, thus preventing thermal damage and lowing the device's threshold.

In addition to these methods, pulsed driving can be used to control the impact of Joule heating. In amorphous thin-film LEDs, using short-pulsed driving can easily increase the injected current density to over 1000 A/cm^2 [15, 28, 48, 52, 54, 60]. Additionally, the width of the electrical driving pulses gradually becomes shorter, transitioning from microseconds [53, 56] to nanoseconds [54, 60]. Using short pulses with a low duty ratio for electrical injection can reduce the effects of Joule heating while maintaining the desired current injection level.

The injected current density in amorphous thin-film LED devices is influenced by the driving method and is closely related to the active area, as shown in **Figure 5**, which illustrates the maximum injected current density as a function of the emission area's size. When the active area is 1–10 mm^2, the maximum injected current typically ranges from 1 to 4 A/cm^2 [28, 51, 57]. However, when the active area is reduced to 0.01–0.1 mm^2, the maximum injected current density can reach up to 600 A/cm^2 [42, 56].

Device	Maximum current density (A/cm^2)	Maximum luminance (cd/cm^2)	Wavelength	Active area	Electrical driven	Publication date	Ref.
Green OLED	12, 000 (Si) 514 (Glass)	1,500,000	~540 nm	25 um (circle) shadow mask	DC	2005	[47]
Green OLED	1163 (Si) 823 (Sapphire) 567 (Glass)		~540 nm	50 um (circle) shadow mask	DC	2005	[48]
Red OLED	800		~610 nm	100 um × 100 um shadow mask	DC	2011	[49]
Red QLED	~1	42,000	640 nm	2 mm× 2 mm shadow mask	DC	2014	[50]
Blue OLED	2800		~460 nm	2 um× 0.05 um E-beam lithography	Pulsed 5 us	2015	[51]
Blue OLED	275		~460 nm	112.5 um (circle) photolithography	Pulsed 5 us	2016	[52]
Green OLED	400/1000		~511 nm	0.07 mm^2 50 um (circle) shadow mask	Pulsed 0.25 us	2017	[53]
Blue OLED	615	~1,000,000	~460 nm		Pulsed	2018	[54]
Green PeLED	620			100 um (circle) shadow mask	Pulsed 2 us	2018	[55]
Red QLED	18 (CW) 1040 (Pulesd)		~614 nm	50 um× 300 um current-focusing	CW Pulsed 1 us	2018	[15]
QLEDs	1 ~ 2	356,000 (R), 614,000 (G), 62,600 (B)	620/545/480 nm	2 mm× 2 mm shadow mask	DC	2019	[56]
Green QLEDs	3.88	1,680,000	540 nm		DC	2019	[57]
Green PeLED	28.9 (CW)	7,646,245	519 nm	0.05 um (circle) photolithography	DC Pulsed 2 us	2020	[58]

Device	Maximum current density (A/cm^2)	Maximum luminance (cd/cm^2)	Wavelength	Active area	Electrical driven	Publication date	Ref.
Blue QLEDs	~1	88,900	457 nm		DC	2020	[59]
Green PeLED	10, 000	1200 kW sr^{-1} m^{-2}	~760 nm	0.01 mm^2 shadow mask	Pulsed 30 ns	2021	[60]
Red QLED	3.4 (CW) 1170 (Pulesd)	9,800,000	~614 nm	2.25 mm^2 50 um× 300 um current-focusing	DC Pulsed 2 us	2022	[28]
Red QLED	557		~614 nm	50 um× 290 um current-focusing	Pulsed 1 us	2023	[42]

Table 2.
Representative high-current-density light-emitting diodes.

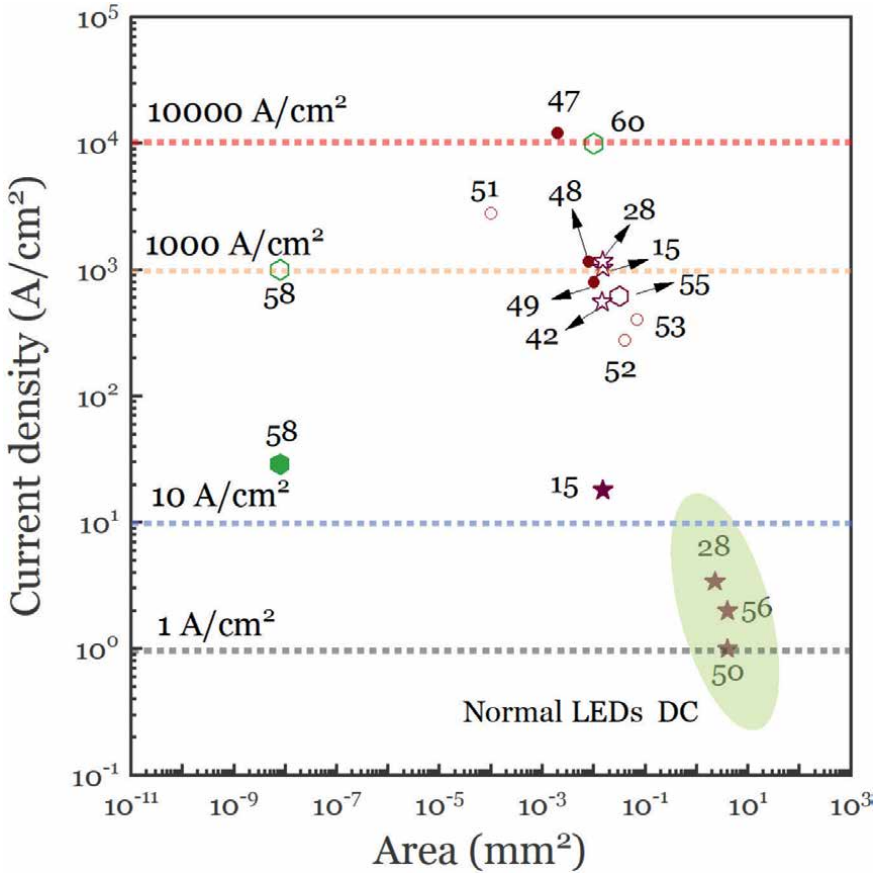

Figure 5.
Enhance the injection current density vs varying the active area and using pulsed-driven mode. The injection current density plotted as a function active area for OLEDs (red circles with pulsed driven [52–54], red solid circles with DC driven [47, 49, 50]), QLEDs (red pentagram with pulsed driven [15, 28, 42], red solid pentagram with DC driven [15, 28, 57]), and PeLEDs (green hexagon with pulsed driven [48, 56, 60], green solid hexagon with DC driven [48]).

The range of 0.001–0.01 mm^2 for the active area is currently the most commonly used for high-current injection LEDs, with the lowest current density exceeding 1000 A/cm^2 [15, 28], and the highest exceeding 10,000 A/cm^2 even under DC driving [47]. However, reducing the active area below 0.001mm^2 will not result in further increases in the maximum injected current [48, 52]. As the active area decreases in amorphous thin-film LEDs, the increase in injected current density can cause thermal effects that affect the device's electrical and optical performance. Balancing the active area and injected current density is crucial for achieving better performance in LED design.

The previous section discussed the effects of the driving method and the active area on the injection current. However, there are also challenges in achieving small-area LEDs. Currently, there are three main methods for obtaining effective areas ranging from tens to thousands of square micrometer, as shown in **Figure 6**. These methods are electron beam lithography [52], photolithography [48], and current-focusing method achieved by depositing wide bandgap LiF in the functional layer [42]. Each method has its own advantages and disadvantages. The first two can be combined with advanced processing technology to obtain high-quality patterns, but

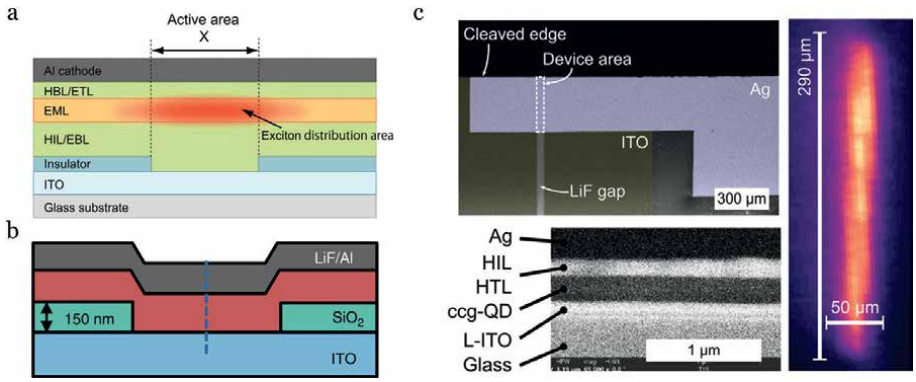

Figure 6.
Representative pattern methods for the small-area LED. (a) E-beam lithography [52]. (b) Photolithography [48]. (c) Current-focusing [42]. Reprinted with permission from refs. [42, 48, 52].

the processing inevitably produces negative effects on the substrate, especially the transparent electrode, which is difficult to eliminate. The last method is particularly suitable for amorphous thin film LEDs, as it can obtain a controllable emitting area without significantly affecting the device performance and fabrication process [15, 28, 42]. However, attention should be paid to the insulation properties of the thinner LiF under high electric fields and the possible manifestation of current diffusion in this structure. Under the premise of not affecting the device's performance, it may be possible to achieve true current-focusing by introducing similar insulation layers in both the hole and electron transport layers.

4. Toward electrical pumping CQD lasing

Electrically pumped CQD lasers have unique optical properties that make them promising for optoelectronic applications, but developing an optical resonator that is compatible with CQD electrical injection is crucial. To achieve this, careful consideration is required for material selection, resonator structure design, CQD material characteristics, compatibility with high-efficiency QLED structures, and fabrication process compatibility. Future development of electrically pumped CQD lasers will require continued improvements in resonator design, such as developing new microcavity structures and design theories to eliminate light scattering, and optimizing the integration processes for resonant cavity and QLED device fabrication to minimize optical losses. With continued research and development in these areas, electrically pumped CQD lasers have the potential to become highly efficient and tunable light sources for various optoelectronic applications.

Yue Wang et al. have pointed out that the scattering problem caused by the nonuniformity of film thickness in CQD results in difficulties or obtaining high-quality factor optical resonant cavities [30]. Klimov et al. have specifically discussed this issue in several review articles [26, 27, 61]. As discussed in the first part of this article, DFB is currently the most commonly used optical resonant cavity for CQD. In recent years, Klimov et al. have made significant progress in the use of DFB structures in continuous-wave pumped CQD lasers [14], LED, and CQD laser dual-function devices [16], and thus, the DFB structure is considered one of the optional structures

for electrically pumped devices. Another optical structure, the planar microcavity or VCSEL, is considered unsuitable for CQD due to high optical. In fact, even in the field of optically pumped CQD lasers, or even QLED, devices based on planar microcavities are rare. Currently, the optically pumped VCSEL CQD laser uses a combination structure [45, 46], where two DBRs are combined physically. There have been no reports of monolithic VCSEL CQD devices. The principle of using planar microcavities to adjust the emission characteristics of CQD is simple in theory, but in practice, there are few reports, and most of them are based on metal microcavities [62–66], which do not significantly improve device performance or regulate emission and laser properties. Wang et al.'s report is one of the few research results that demonstrate the advantages of planar microcavities [67]. If we can combine the above discussion and analyze why the use of planar optical microcavities cannot effectively regulate the emission and laser properties of CQD, it may be possible to develop a new resonant cavity structure to assist in achieving electrically driven CQD lasers.

The use of planar microcavities or VCSELs to regulate the emission and laser properties of CQD lasers has been considered unsuitable due to high optical losses and complex preparation processes. However, a recent study by Wang et al. demonstrates successful use of planar microcavities to regulate CQD laser properties, which may be due to targeted improvements and optimized preparation processes. Overcoming optical losses and preparing high-quality factor planar microcavities remains a challenge. Nonetheless, planar microcavities offer advantages such as simplicity, control, scalability, and wider wavelength tuning range compared to distributed feedback structures. Combining the advantages of planar microcavities and distributed feedback structures may lead to better solutions for improving CQD laser performance. Further research is needed to explore the effective regulation of CQD laser properties using planar microcavities or other optical structures and to develop new resonant cavity structures for electrically driven CQD lasers.

In this case, researchers need to explore new methods to address these issues. Gao et al.'s research has shown that interface engineering can effectively reduce optical losses caused by interface states [68], thereby improving the quality factor and laser characteristics of microcavities (**Figure 7**).

As shown in **Figure 8**, Lin and coauthors have proposed a novel design strategy for microcavities light and laser devices. The non-quarter wave microcavity structural design is a promising approach for enhancing the performance of optoelectronic devices, such as OLEDs [69] and Pe LEDs [70]. The use of non-quarter-wave DBRs in MOLEDs leads to a higher EQE and narrower emission spectrum compared to quarter-wave DBRs. Additionally, the use of non-quarter wave DBRs in metal-dielectric microcavities can provide further enhancements in device performance. This novel microcavity design presents new research opportunities for electrically driven lasers based on planar microcavity structures. The proposed design enables flexible tuning of the cavity resonance modes by adjusting the thickness of the optical spacer layer while maintaining high-performance QLED devices. This approach facilitates efficient coupling between the microcavity modes and the CQD emitting layer, enhancing the laser's overall performance. By employing this new microcavity design, researchers can achieve effective control over the emission characteristics of CQD lasers while maintaining high device performance.

The application of non-quarter-wave microcavity designs in OLED and PeLED devices is a promising approach for optimizing the performance of CQD technology. The design approach solves the challenges associated with balancing the optical

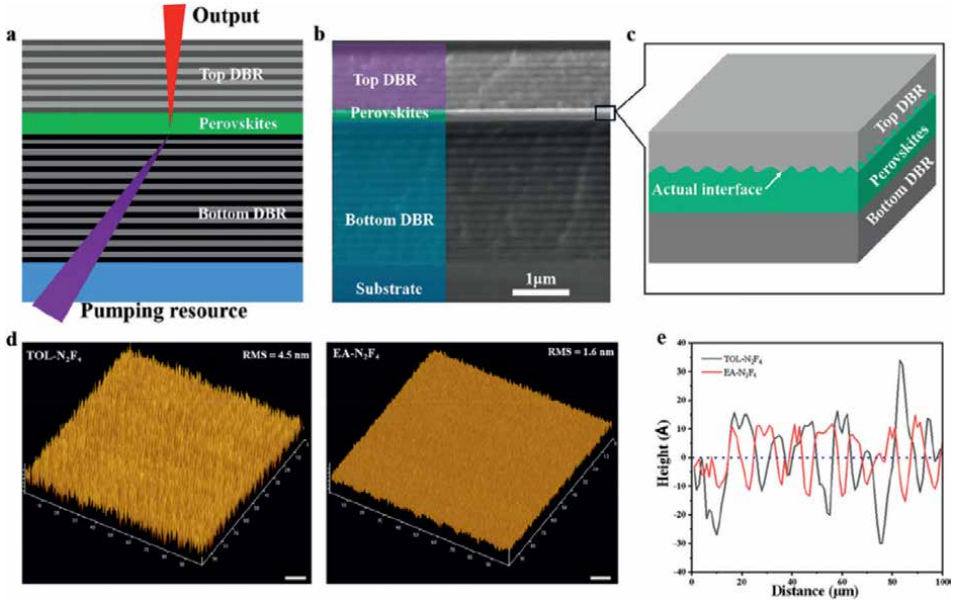

Figure 7.
Schematic representation of the laser device and the surface properties of N2F4 films. (a) Illustrates the ideal schematic of the laser device. (b) Shows a cross-sectional SEM image of the device. (c) Displays the actual schematic of the interface between the perovskite gain layer and top DBR. (d) Presents an atomic force microscopy image of the TOL-N2F4 and EA-N2F4 films, with a horizontal scale bar of 10 μm. (e) Shows the corresponding height profile of the TOL-N2F4 and EA-N2F4 films at the 100-micron scale. Reprinted with permission from ref. [68].

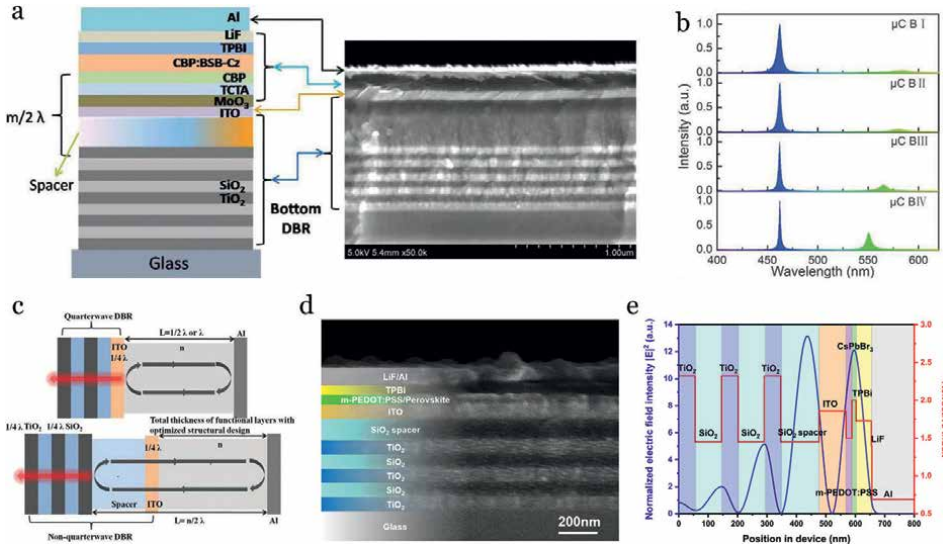

Figure 8.
Structures of OLED and PeLED with non-quarter wave microcavity structural design. (a) Structure and cross-sectional SEM image of MOLEDs. (b) EL spectra of MOLEDs with different non-quarter wave DBRs. (c) Schematic of a metal-dielectric microcavity with different DBRs, including quarter wave DBR and non-quarter wave DBR, forming a Fabry-Perot resonator that surrounds a cavity medium of refractive index n and thickness L. (d) Cross-sectional SEM image of the perovskite microcavity device. (e) the refractive index of each layer and standing wave electric field distribution in the designed MPeLED. Reprinted with permission from refs. [69, 70].

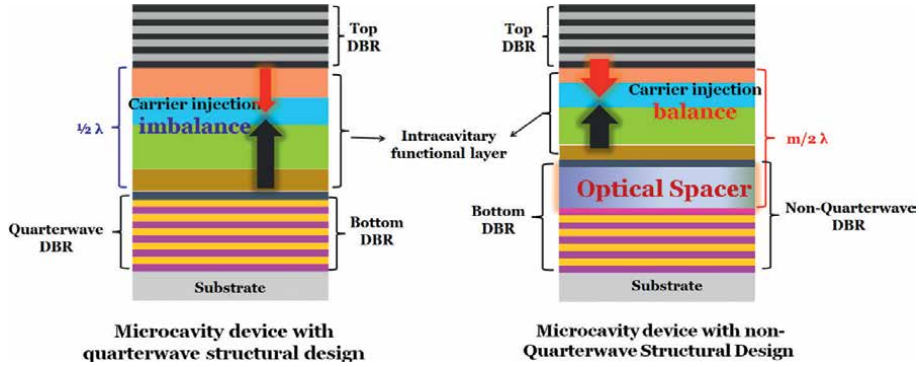

Figure 9.
A proposed planar microcavity structure based on non-quarter-wave DBR for high-efficiency electrical injection based on CQD.

and electrical performance of CQD devices, and enables the optimization of both aspects in tandem. By employing non-quarter-wave DBRs, the actual reflection interface of the microcavity can be relocated inside the DBR, effectively mitigating the optical interface issues that typically arise when reducing the nanometer functional layer and contacting the optical resonant cavity. A novel optical resonant cavity structure has been designed for CQD lasers based on this approach, which improves the coupling efficiency between the microcavity mode and the CQD emitting layer, while also resolving optical interface issues, as illustrated in **Figure 9**. The proposed planar microcavity structure based on non-quarter-wave DBR offers a promising avenue for the development of high-efficiency optoelectronic devices based on colloidal quantum dots. Its unique design enables flexible tuning of the cavity resonance modes and efficient coupling with the CQD emitting layer, which are critical for achieving high-performance CQD devices. The proposed approach provides a simple and effective solution for realizing efficient coupling between the CQD emitting layer and the microcavity modes, which is critical for achieving high-performance CQD lasers.

5. Summary and outlook

After years of extensive research, electrically driven CQD lasers are on the verge of becoming a reality. However, researchers have found that the challenges faced by CQD lasers are similar to those encountered by organic semiconductor lasers [71, 72]. Therefore, there may be potential synergies between these two technologies, and it is essential to explore how to leverage these synergies to the fullest [27, 61]. The latest research progress in CQD has leveraged the design approach of inorganic optoelectronic devices to achieve high current injection through current focusing [73, 74], enabling CQD optical-pumping lasers and LED functional devices [16]. This approach is also inspired by the DFB electrical-driven organic devices [75]. Although many teams have made significant efforts in this regard, the differences between CQD materials and devices have made it challenging to implement promising ideas. Based on the basic principles of optics and materials science [76], and considering the characteristics of colloidal quantum dots, the characteristics of QLED are studied.

Developing a microcavity for efficient electrical injection of CQDs, overcoming optical-electrical balance issues [69].

In summary, the realization of electrically driven CQD lasers still lacks several critical pieces. To address this issue, the novel optical microcavity design theory mentioned in this article, as well as the optical resonant cavity constructed based on the characteristics of CQD materials and devices, successfully separates the optical and electrical interfaces of the electrically driven device. This separation may become a crucial puzzle piece in achieving electrically driven CQD lasers. The potential synergies between CQD and organic semiconductor lasers should be explored further, and leveraging the latest research progress in the field of inorganic optoelectronic devices and organic lasers [77, 78] may hold the key to realizing electrically driven CQD lasers. The novel optical microcavity design theory and the constructed optical resonant cavity may provide an essential breakthrough in this regard. Recent advancements in CQD lasers indicate that unlocking the potential synergies between different technologies will play a critical role in achieving breakthrough progress [79]. Perhaps, the final implementation of electrically driven CQD lasers may depend on the synergistic effects of numerous research fields.

Author details

Jie Lin*, Geng He, Yun Hu and Jingsong Huang
Oxford Suzhou Centre for Advanced Research (OSCAR), University of Oxford, Suzhou, P. R. China

*Address all correspondence to: jie.lin@oxford-oscar.cn

IntechOpen

References

[1] Hall RN, Fenner GE, Kingsley JD, et al. Coherent light emission from GaAs junctions. Physical Review Letters. 1962;**9**:366-368

[2] Tessler N, Denton GJ, Friend RH. Lasing from conjugated-polymer microcavities. Nature. 1996;**382**:695-697

[3] Klimov VI, Mikhailovsky AA, Xu S, et al. Optical gain and stimulated emission in nanocrystal quantum dots. Science. 2000;**290**:314-317

[4] Kondo S, Suzuki K, Saito T, et al. Photoluminescence and stimulated emission from microcrystalline CsPbCl3 films prepared by amorphous-to-crystalline transformation. Physical Review B. 2004;**70**:205322

[5] Kagan CR, Lifshitz E, Sargent EH, et al. Building devices from colloidal quantum dots. Science. 2016;**353**:aac5523

[6] Jung H, Lee M, Han C, et al. Efficient on-chip integration of a colloidal quantum dot photonic crystal band-edge laser with a coplanar waveguide. Optics Express. 2017;**25**:32919

[7] Clark J, Lanzani G. Organic photonics for communications. Nature Photonics. 2010;**4**:438-446

[8] Xie W, Stöferle T, Rainò G, et al. On-chip integrated quantum-dot–silicon-nitride microdisk lasers. Advanced Materials. 2017;**29**:1604866

[9] Cegielski PJ, Giesecke AL, Neutzner S, et al. Monolithically integrated perovskite semiconductor lasers on silicon photonic chips by scalable top-down fabrication. Nano Letters. 2018;**18**:6915-6923

[10] Zhang C, Zou CL, Zhao Y, et al. Organic printed photonics: From microring lasers to integrated circuits. Science Advances. 2015;**1**:e1500257

[11] Kang D, Chen H, Yoon J. Stretchable, skin-conformal microscale surface-emitting lasers with dynamically tunable spectral and directional selectivity. Applied Physics Letters. 2019;**114**:041103

[12] Chen YC, Fan X. Biological lasers for biomedical applications. Advanced Optical Materials. 2019;**7**:1900377

[13] Karl M, Glackin JME, Schubert M, et al. Flexible and ultra-lightweight polymer membrane lasers. Nature Communications. 2018;**9**:1525

[14] Fan F, Voznyy O, Sabatini RP, et al. Continuous-wave lasing in colloidal quantum dot solids enabled by facet-selective epitaxy. Nature. 2017;**544**:75-79

[15] Lim J, Park YS, Klimov VI. Optical gain in colloidal quantum dots achieved with direct-current electrical pumping. Nature Materials. 2018;**17**:42-48

[16] Roh J, Park Y, Lim J, et al. Optically pumped colloidal-quantum-dot lasing in LED-like devices with an integrated optical cavity. Nature Communications. 2020;**11**:271

[17] Gao S, Zhang C, Liu Y, et al. Lasing from colloidal InP/ZnS quantum dots. Optics Express. 2011;**19**:5528

[18] Kozlov OV, Park Y, Roh J, et al. Sub–single-exciton lasing using charged quantum dots coupled to a distributed feedback cavity. Science. 2019;**675**:672-675

[19] Klimov VI, Ivanov SA, Nanda J, et al. Single-exciton optical gain in

semiconductor nanocrystals. Nature. 2007;**447**:441-446

[20] Wang Y, Ta VD, Gao Y, et al. Stimulated emission and lasing from CdSe/CdS/ZnS core-multi-shell quantum dots by simultaneous three-photon absorption. Advanced Materials. 2014;**26**:2954-2961

[21] Htoon H, Hollingworth JA, Malko AV, et al. Light amplification in semiconductor nanocrystals: Quantum rods versus quantum dots. Applied Physics Letters. 2003;**82**:4776-4778

[22] Moreels I, Rainò G, Gomes R, et al. Nearly temperature-independent threshold for amplified spontaneous emission in colloidal CdSe/CdS quantum dot-in-rods. Advanced Materials. 2012;**24**:OP231-OP235

[23] She C, Fedin I, Dolzhnikov DS, et al. Low-threshold stimulated emission using colloidal quantum wells. Nano Letters. 2014;**14**:2772-2777

[24] Taghipour N, Delikanli S, Shendre S, et al. Sub-single exciton optical gain threshold in colloidal semiconductor quantum wells with gradient alloy shelling. Nature Communications. 2020;**11**:3305

[25] Wang Y, Zhi M, Chang YQ, et al. Ultralow threshold amplified spontaneous emission from CsPbBr3 nanoparticles exhibiting Trion gain. Nano Letters. 2018;**18**:4976-4984

[26] Pietryga JM, Park YS, Lim J, Fidler AF, et al. Spectroscopic and device aspects of nanocrystal quantum dots. Chemical Reviews. 2016;**116**:10513-10622

[27] Park YS, Roh J, Diroll BT, et al. Colloidal quantum dot lasers. Nature Reviews Materials. 2021;**6**:382-401

[28] Jung H, Park Y, Ahn N. Two-band optical gain and ultrabright electroluminescence from colloidal quantum dots at 1000A cm^{-2}. Nature Communications. 2022;**13**:3734

[29] Geiregat P, Van Thourhout D, Hens Z. A bright future for colloidal quantum dot lasers. NPG Asia Materials. 2019;**11**:41

[30] Wang Y, Sun H. Advances and prospects of lasers developed from colloidal semiconductor nanostructures. Progress in Quantum Electronics. 2018;**60**:1-29

[31] Malko AV, Mikhailovsky AA, Petruska MA, et al. From amplified spontaneous emission to microring lasing using nanocrystal quantum dot solids. Applied Physics Letters. 2002;**81**:1303-1305

[32] Kazes M, Lewis DY, Ebenstein Y, et al. Lasing from CdSe/ZnS quantum rods in a cylindrical microcavity. Advanced Materials. 2002;**14**:317-321

[33] Wang Y, Leck KS, Ta VD, et al. Blue liquid lasers from solution of CdZnS/ZnS ternary alloy quantum dots with quasi-continuous pumping. Advanced Materials. 2015;**27**:169-175

[34] Snee PT, Chan Y, Nocera DG, et al. Whispering-gallery-mode lasing from a semiconductor nanocrystal/microsphere resonator composite. Advanced Materials. 2005;**17**:1131-1136

[35] Montanarella F, Urbonas D, Chadwick L, et al. Lasing Supraparticles self-assembled from nanocrystals. ACS Nano. 2018;**12**:12788-12794

[36] Le Feber B, Prins F, De Leo E, et al. Colloidal-quantum-dot ring lasers with active color control. Nano Letters. 2018;**18**:1028-1034

[37] Eisler HJ, Sundar VC, Bawendi MG, et al. Color-selective semiconductor nanocrystal laser. Applied Physics Letters. 2002;**80**:4614-4616

[38] Chen Y, Guilhabert B, Herrnsdorf J, et al. Flexible distributed-feedback colloidal quantum dot laser. Applied Physics Letters. 2011;**99**:211103

[39] Foucher C, Guilhabert B, Laurand N, et al. Wavelength-tunable colloidal quantum dot laser on ultra-thin flexible glass. Applied Physics Letters. 2014;**104**:141108

[40] Roh K, Dang C, Lee J, et al. Surface-emitting red, green, and blue colloidal quantum dot distributed feedback lasers. Optics Express. 2014;**22**:18800

[41] Adachi MM, Fan F, Sellan DP, et al. Microsecond-sustained lasing from colloidal quantum dot solids. Nature Communications. 2015;**6**:8694

[42] Ahn N, Park YS, Livache C, et al. Optically excited lasing in a cavity-based, high-current-density quantum dot electroluminescent device. Advanced Materials. 2023;**35**:2206613

[43] Zavelani-Rossi M, Lupo MG, Krahne R, et al. Lasing in self-assembled microcavities of CdSe/CdS core/shell colloidal quantum rods. Nanoscale. 2010;**2**:931-935

[44] Di Stasio F, Grim JQ, Lesnyak V, et al. Single-mode lasing from colloidal water-soluble CdSe/CdS quantum dot-in-rods. Small. 2015;**11**:1328-1334

[45] Dang C, Lee J, Breen C, et al. Red, green and blue lasing enabled by single-exciton gain in colloidal quantum dot films. Nature Nanotechnology. 2012;**7**:335-339

[46] Guzelturk B, Kelestemur Y, Olutas M, et al. Amplified spontaneous emission and lasing in colloidal Nanoplatelets. ACS Nano. 2014;**8**:6599-6605

[47] Yamamoto C, Kasajima H, Yokoyama H, et al. Extremely-high-density carrier injection and transport over 12000 a/cm^2 into organic thin films. Applied Physics Letters. 2005;**86**:083502

[48] Zou C, Liu Y, Ginger DS, et al. Suppressing efficiency roll-off at high current densities for ultra-bright green perovskite light-emitting diodes. ACS Nano. 2020;**14**:6076-6086

[49] Nishioka K, Nasu K, Hamaguchi S, et al. Injection and transport of high current density over 1000 A/cm^2 in organic light emitting diodes under pulse excitation. Japanese Journal of Applied Physics. 2005;**44**:3659-3662

[50] Kasemann D, Brückner R, Fröb H, et al. Organic light-emitting diodes under high currents explored by transient electroluminescence on the nanosecond scale. Physical Review B. 2011;**84**:115208

[51] Dai X, Zhang Z, Jin Y, et al. Solution-processed, high-performance light-emitting diodes based on quantum dots. Nature. 2014;**515**:96-99

[52] Hayashi K, Nakanotani H, Inoue M, et al. Suppression of roll-off characteristics of organic light-emitting diodes by narrowing current injection/transport area to 50 nm. Applied Physics Letters. 2015;**106**:093301

[53] Yoshida K, Nakanotani H, Adachi C. Effect of joule heating on transient current and electroluminescence in p - i - n organic light-emitting diodes under pulsed voltage operation. Organic Electronics. 2016;**31**:287-294

[54] Lenk S, Reineke S, Frob H, et al. Novel organic light-emitting diode design for future lasing applications. Organic Electronics. 2017;**48**:132-137

[55] Mamada M, Fukunaga T, Bencheikh F, et al. Low amplified spontaneous emission threshold from organic dyes based on Bis-stilbene. Advanced Functional Materials. 2018;**28**:1802130

[56] Kim H, Zhao L, Price JS, et al. Hybrid perovskite light emitting diodes under intense electrical excitation. Nature Communications. 2018;**9**:4893

[57] Shen H, Gao Q, Zhang Y, et al. Visible quantum dot light-emitting diodes with simultaneous high brightness and efficiency. Nature Photonics. 2019;**13**:192-197

[58] Sun Y, Su Q, Zhang H, et al. Investigation on thermally induced efficiency roll-off: Toward efficient and Ultrabright quantum-dot light-emitting diodes. ACS Nano. 2019;**13**:11433-11442

[59] Kim T, Kim HK, Kim S, et al. Efficient and stable blue quantum dot light-emitting diode. Nature. 2020;**586**:385-389

[60] Zhao L, Roh K, Kacmoli S, et al. Nanosecond-pulsed perovskite light-emitting diodes at high current density. Advanced Materials. 2021;**33**:2104867

[61] Jung H, Ahn N, Klimov VI. Prospects and challenges of colloidal quantum dot laser diodes. Nature Photonics. 2021;**15**:643-655

[62] Liu G, Zhou X, Chen S. Very bright and efficient microcavity top-emitting quantum dot light-emitting diodes with Ag electrodes. ACS Applied Materials & Interfaces. 2016;**8**:16768-16775

[63] Liu S, Liu W, Ji W, et al. Top-emitting quantum dots light-emitting devices employing microcontact printing with electricfield-independent emission. Scientific Reports. 2016;**6**:22530

[64] Lai KY, Yang S, Tsai TC, et al. Top-emitting active-matrix quantum dot light-emitting diode Array with optical microcavity for micro QLED display. Nanomaterials. 2022;**12**:2683

[65] Yu H, Zhu H, Xu M, et al. High efficiency, large-area, flexible top-emitting quantum-dot light-emitting diode. ACS Photonics. 2023;**10**:2192-2200

[66] Mei G, Wang W, Wu D, et al. Full-color quantum dot light-emitting diodes based on microcavities. IEEE Photonics Journal. 2022;**14**:8219709

[67] Wang L, Lin J, Lv Y, et al. Red, green, and blue microcavity quantum dot light-emitting devices with narrow line widths. ACS Applied Nano Materials. 2020;**3**:5301-5310

[68] Gao X, Lin J, Guo X, et al. Room-temperature continuous-wave microcavity lasers from solution-processed smooth quasi-2D perovskite films with low thresholds. Journal of Physical Chemistry Letters. 2023;**14**:2493-2500

[69] Lin J, Hu Y, Liu X. Microcavity-enhanced blue organic light-emitting diode for high-quality monochromatic light source with Nonquarterwave structural design. Advanced Optical Materials. 2020;**8**:1901421

[70] Liu T, Yang C, Fan Z, et al. Spectral narrowing and enhancement of directional emission of perovskite light emitting diode by microcavity. Laser & Photonics Reviews. 2022;**16**:2200091

[71] Zhang Q, Tao W, Huang J, et al. Toward electrically pumped organic lasers: A review and outlook on material developments and resonator architectures. Advanced Photonics Research. 2021;**2**:2000155

[72] Wang K, Zhao YS. Pursuing electrically pumped lasing with organic semiconductors. Chem. 2021;**7**:3221-3231

[73] Chung T, Walter G, Holonyak N. Coupled strained-layer InGaAs quantum-well improvement of an InAs quantum dot AlGaAs–GaAs–InGaAs–InAs heterostructure laser. Applied Physics Letters. 2001;**79**:4500-4502

[74] Huang Z, Zimmer M, Hepp S, et al. Optical gain and lasing properties of InP/AlGaInP quantum-dot laser diode emitting at 660 nm. IEEE Journal of Quantum Electronics. 2019;**55**:2000307

[75] Sandanayaka ASD, Matsushima T, Bencheikh F, et al. Indication of current-injection lasing from an organic semiconductor. Applied Physics Express. 2019;**12**:61010

[76] Vahala KJ. Optical microcavities. Nature. 2005;**424**:839-845

[77] Liu X, Li H, Song C, et al. Microcavity organic laser device under electrical pumping. Optics Letters. 2009;**34**:503

[78] Lin J, Hu Y, Lv Y, et al. Light gain amplification in microcavity organic semiconductor laser diodes under electrical pumping. Science Bulletin. 2017;**62**:1637-1638

[79] Ahn N, Livache C, Pinchetti V, et al. Electrically driven amplified spontaneous emission from colloidal quantum dots. Nature. 2023;**617**:79-85

Chapter 6

Device Fingerprint as a Transmission Security Paradigm

Pantea Nadimi Goki, Thomas Teferi Mulugeta, Nicola Sambo, Roberto Caldelli, Ramin Solaimani and Luca Potì

Abstract

Optoelectronics plays a crucial role in the field of telecommunications and networks. Specifically, optoelectronic constructions serve as sources, detectors, and light controllers in communication and optical network systems. One of the requirements of a secure system is evaluating the optical components of optoelectronic assemblies and ensuring their security against malicious attacks. To address this, we introduce the concept of optical fingerprints in optical communications and networks. This concept includes reading the fingerprints of devices, sub-systems, and systems to address services that comprise security, authentication, identification, and monitoring. Using optical fingerprints as a signature of optical fibers, it becomes possible to identify and evaluate any optical component of optoelectronic assemblies through their pigtail.

Keywords: security, authentication, identification, monitoring, optical fingerprints, optical physical unclonable functions, digital signature, optical network, communication systems

1. Introduction

The rapid development of optical telecommunication technologies has necessitated the evolution of telecommunication security techniques and protocols. The increasing adoption of fiber optic communication systems, which constitute the foundation of global telecommunications infrastructure [1], poses challenges to ensuring the accessibility and confidentiality of networks and data in the presence of adversarial attacks. Adversarial potency is constantly increasing through the utilization of high-performance devices and the exploitation of intensive machine-learning algorithms to enhance attack effectiveness.

Security and confidentiality within the open systems interconnection (OSI) (framework, which describes the functions of networking or telecommunications systems) are primarily governed by the upper layers. The OSI security architecture, recommended by ITU-T, establishes a standard for data security by identifying the attacks, security services, and security mechanisms. In this model, security protocols are applied from the top layer down. The application layer, which is the layer most users interact with, may include end-to-end cryptography (e.g., WhatsApp messages

are encrypted to be recognized just by users). Additionally, the presentation and session layers, which are responsible for syntax processing and creating communication channels between devices, respectively, may benefit from data cryptography. The transport layer, responsible for transmitting the data across network connections, can utilize protocols such as Secure Sockets Layer (SSL) or Transport Layer Security (TLS). These protocols provide authentication between parties, data integrity, and digital signature. The network layer, which handles the routing of the data, is responsible for security at the network level using functions such as packet authentication, cryptography, and integrity (e.g., Internet Protocol Security – IPsec). In contrast, admission control performs a check at the link layer to guarantee the proposed connection. Wireless systems developed Wi-Fi Protected Access (WPA) protocols to add protection mainly to wireless computer networks. Regarding the physical layer (PHY), security implementation is typically lacking as the establishment of optimal security protocols at this level remains a worldwide problem.

Despite security and confidentiality primarily being addressed at the upper layers, the implementation of physical layer security offers an extra level of protection that is currently lacking in communication networks and remains a significant global technical challenge. With that objective in mind, we introduce optical identification (OI), a novel method that aims to implement a novel (ID) technique for enhancing physical layer security (PLS).

Despite the numerous studies, suggestions, and experimental works reported on physical layer security (PLS) [2, 3], there remains a significant need to establish a practical and effective protocol or technique for physical layer security. In refs. [4,5], PLS has been defined through keys generated by digital signal processing (DSP). The disadvantage of such a method is its vulnerability to digital attacks, similar to other cryptography-based PLS [6]. The PLS enhancement through the monitoring of optical communication with quantum-level sensitivity using a quantum pilot tone, as proposed in ref. [7], or more commonly through the Quantum key distribution (QKD) [8, 9] provides intrinsic security. However, these approaches are not cost-effective and often challenging to implement. Recently, an approach for boosting PLS was introduced with a subcarrier identification process in the receiver DSP [10], which is vulnerable if attackers have knowledge of the transceiver DSP configurations. The investigation of PLS-based optical chaos communication has explored various structures [11–13]. However, the impracticality of this approach arises from the high-level synchronization requirement between the transmitter and the receiver [14]. Additionally, the security of chaotic communication can be compromised by the problems created by the feedback loop of the chaotic system [15]. A viable approach has been proposed lately, in refs. [16, 17], involving the use of optical steganography to hide messages below the noise level, thereby ensuring secure communication. Although this technique is practical, it cannot detect the existence of an eavesdropper. This technique has vulnerability to adversaries who know the system and are able to acquire and analyze the whole spectrum [18, 19]. In recent investigations of security techniques, physical unclonable function (PUF), as a new approach for PLS, attracted considerable attention.

The PUF approach is based on the material's physical features, in which a physical device provides unique output for a given input thanks to its unclonable and unpredictable response. These types of devices are usually implemented in complementary metal-oxide-semiconductor (CMOS) [20, 21]. PUF overcomes the disadvantages of computational cryptography, steganography, and other techniques, and its security level is subject to the difficulty of cloning the function response [22, 23].

Therefore, a specific input function called challenge (*Challenge*) ends with the individual output function called response (*Response*). New challenges will not end with the same response, and every single challenge has its unique response. The significant fact about PUFs is that any PUF material has its own unique function, which means applying the same challenge to two different PUF materials results in two different responses. This feature makes PUFs a strong security technique, and a viable alternative to today's techniques based on cryptography. It is worth mentioning that the term PUF includes several technical and technological categories. Among them, electrical PUF has been considered in ref. [24] as a PLS technique, however, this technique is not practical because both the transmitter and receiver should have access to the same PUF to synchronize their channel [25]. Optical PUF (OPUF), based on the optical token, has also been investigated in several studies to generate secure cryptography keys [26] and for authentication applications [27].

In this Chapter, we introduce the concept of optical identification by reading the optical fingerprint in optical communications and networks, exploiting OPUF, which is a practical technique to enhance network PLS based on OPUF. The fundamental principle of the proposed technique is to identify networks, optical links, systems, sub-systems, network elements, and any optical component of optoelectronic assemblies that possess optical fiber or fiber pigtail. The proposed technique is carried out based on the following procedures: in the first step, the optical fingerprint of the device under test (DUT) is read and stored. The fingerprint is generated using the Rayleigh backscattering pattern (RBP) of the fiber (or fiber pigtail), which is considered a strong OPUF [28]. In this manner, every DUT possesses its unique fingerprint. The second step is DUT identification through the simple technique of comparison between a stored fingerprint and the DUT to be identified. We demonstrate the validation of fingerprints through several different metrics, including security, uniqueness, unpredictability, unlclonability, and reproducibility. The benefit of our proposed technique is that it does not require receiver-transmitter synchronization [25] or the fabrication of OPUF [29] as the inherent feature of the fibers serves as our proposed OPUF.

The proposed method can be used for communication security, authentication, identification, and monitoring purposes, both in point-to-point communication and optical networks. It could be considered an effective security implementation to evaluate the optical components of optoelectronic assemblies and ensure their security against malicious attacks.

The following sections will provide a detailed description of the proposed technique. Section 2 presents an overview of physical unclonable functions, which form the security basis of the proposed method. Section 3 introduces the concept of optical fingerprints in networks and communication systems. The performance evaluation of optical identification (OI) is described in Section 4. Section 5 shows possible applications and discussion. Finally, conclusions are summarized in Section 6.

2. An overview of PUF

Physical unclonable functions (PUFs) [30] can be considered like biometrics [31] for physical objects such as sensors, devices, integrated circuits, and so on. In fact, as it happens for living beings, and for humans in particular, in which biometrics (e. g. fingerprints, DNA) can be adopted to identify and distinguish different exemplars and subjects, PFUs can be similarly used to make a distinction among diverse physical

objects involved in a specific process. The reference to the word "physical" indicates that PUFs are generated by resorting to some physical characteristics that are intrinsically present within a certain electronic device. Such features are generally embedded during the fabrication step and are usually due to some small manufacturing imperfections induced by the construction procedure itself. Such imperfections are randomly generated but remain persistent within each device and, above all, they grant distinctiveness among each different physical object; this desirable aspect can be effectively exploited for security mechanisms in various application scenarios such as IoT (Internet of Things). The other particularly interesting aspect concerns the adjective "unclonable," which means these features, and especially the measurements they determine, cannot be easily duplicated in order to induce a falsification and/or exchange an identity. In addition to this, PUFs do not need to be stored within an electronic memory as it normally happens for a digital secret, but they intrinsically belong to the physical object as a classical fingerprint. This is advantageous because, for instance, specific secure hardware solutions are not required and, furthermore, it is more difficult to perpetrate invasive attacks. This can be better understood if we imagine using a PUF to generate a cryptographic root key for a specific device. In this case, such a key is created by the PUF and neither any key injection is required, nor it can be copied from one device to be used onto another one. The crypto key does not need to be stored anywhere but it can be recovered from the device's fingerprint whenever it is necessary during, for example, an authentication procedure.

PUF-based security systems can be generally implemented as identification mechanisms based on a well-known *challenge-response pairs (CRPs) protocol*. As evidenced in Eq. (1), each time a PUF receives a "challenge" (CH) as input, it outputs a "response" that is highly difficult to be predicted and replicated.

$$PUF_A(CH_i) \neq PUF_A(CH_j), \forall i \neq j \tag{1}$$

A PUF-based circuit can be seen as a black-box model where the input challenge is processed by the function F(.), whose characteristics are determined by the PUF itself; the resulting output is the response such that response = F(challenge). The internal behavior of the function F(.) (namely the PUF) is strictly correlated to the peculiar inner manufacturing variabilities and cannot be manipulated.

PUFs can be categorized in different ways, anyway, a primary mode for their classification is to subdivide them into soft and strong PUFs. Such a distinction is basically related to the number of challenges, when this number is quite limited, they are generally indicated as soft ones and, on the contrary, in the case, such value is higher (e.g., a complete determination of the CRPs would not be possible within a feasible time) they are labeled as strong PUFs. Other important characteristics that permit to catalog PUFs concern uniqueness and reliability. The term uniqueness is intended in that the response provided by a PUF is different for different input challenges (see Eq. (1)) and, furthermore, the same input challenge should generate distinctive output responses when applied to diverse PUFs (as evidenced in Eq. (2)).

$$PUF_A(CH_i) \neq PUF_B(CH_i), \forall A \neq B \tag{2}$$

The distinctiveness between diverse PUF's output is generally evaluated in terms of Hamming distance when it is a binary vector/matrix, but other kinds of measurements can be adopted such as mean squared error (MSE) or cross-correlation (CC). Diversely, the term *reliability* regards the capacity of a PUF to provide always the

same answer when a fixed challenge is passed as input (i.e., an intra-Hamming distance that should be ideally equal to zero). *Reliability* has not to be confused with *steadiness*, though they are strictly related to each other; *steadiness* refers to the degree of response variability but is possibly determined by some changes that occurred in the operative scenario such as variations in temperature or electric supply or even due to aging effect [32].

Different kinds of PUFs exist, one of the first examples of an optical PUF is probably the system introduced in ref. [33]. Such a system is constituted by an input laser beam directed toward a stationary scattering medium afterward the speckle output pattern is recorded. In this case, the challenge is based on the laser XY location and its polarization while the response is the associated speckle pattern. Such a pattern is strongly dependent on the input location/polarization since multiple scattering events can occur inside the scattering medium. A simple example of a soft PUF is represented by the "power-on" state of an SRAM. In fact, though an SRAM cell is symmetric, manufacturing anomalies can induce a tendency toward a logical "0" or "1" when the power is switched on. This variability is random across the entire SRAM and this determines a univocal fingerprint that can provide a distinctiveness. Another interesting kind of soft PUF can be determined by the acquisition process of digital images (videos). In fact, when a photo is taken, the camera sensor, which is composed of a two-dimensional array of CCDs (Charge Coupled Devices), is hit by light photons whose energy is then converted into electron charges. Due to manufacturing imperfections in the silicon wafer, each cell of the camera's sensor differently answers to a uniform incoming light. Consequently, this determines the superimposition, onto each content it takes (images and/or videos), of a systematic noise, named PRNU (photo response nonuniformity noise [34]) Such noise is not perceivable and does not degrade the visual quality of the acquired contents, but it effectively constitutes a sort of fingerprint that is embedded within the image pixels. Such a fingerprint can be successively extracted by means of high-pass filtering and compared with the available reference fingerprints of different cameras to perform a source identification similar to what happens for the association process between the gun and the bullet in ballistics.

Though the possible advantages are significant, PUFs are anyway prone to security issues as well as other security mechanisms and these crucial aspects have to be carefully tackled in relation to the application scenario where PUFs are adopted for security purposes. Above all, the reliability of the verification system has to be assessed in order to avoid false alarms and missing detections, furthermore, PUFs are not immune to malicious security attacks such as spoofing attacks and have to be properly designed to effectively deal with personal data management and user privacy.

3. Optical fingerprint

Clearly, physical elements possess distinctive fingerprints, much like humans do. While we have the capability to identify and potentially render them impervious to cloning, this notable feature remains underutilized in communication systems and networks. The scope of our research covers the concept of optical fingerprinting (ID); where every photonic device, optoelectronic component, sub-system, or system is assigned an exclusive fingerprint extracted from their physical characteristics and the nonideality of the optical object in physical process. This approach serves as an

effective security technique. By assuming the ability to read these fingerprints, we model security, authentication, identification, and monitoring in point-to-point communication and extend it to optical networks.

3.1 Concept

A point-to-point communication system can be represented by three essential subsystems: transmitter, channel, and receiver (**Figure 1**). As previously mentioned in the introduction, each sub-system possesses its unique fingerprint, which may be labeled as ID_{TX}, ID_{Ch}, and ID_{RX}, respectively. We make the initial assumption that each fingerprint can be acquired independently, forming a strong basis for our analysis.

Passive sub-system: In this scenario, where the channel is considered to be a passive sub-system, three potential security approaches may be envisaged:

1. The transmitter reads ID_{Ch} and ID_{RX} to ensure that the information will pass the designated channel and reaches the intended receiver;

2. The receiver reads ID_{TX} and ID_{Ch} to determine the sender's identity and the physical path of transmission;

3. The transmitter reads $ID_{RX,}$ while the receiver acquires ID_{TX} enabling both subsystems to identify each other. Additionally, they can also verify ID_{Ch} to ensure the integrity of the communication path.

In this simple case, each signature can be a sufficiently long binary sequence that can be compared to stored signatures for the purpose of identification. A binary XOR operation would be enough for such a comparison. In a real system, a signature match will occur with a certain probability P_x, which represents X the specific sub-system, and $0 \leq P_x \leq 1$.

Active sub-system: In a slightly more advanced scenario, when the channel is an active sub-system that includes devices, the method is extended to enable reading and validating the signature of the entire system and/or every single sub-system. A direct extension can be represented as illustrated in **Figure 2**, which depicts a network architecture comprising N subsystems each with its unique identifier ID_i where $1 \leq i \leq N$ ('i' represents the i*th* subsystem). In an optical network, sub-systems can encompass various components such as transceivers, optical fibers, and optical nodes, as well as, filters, optical cross-connects, reconfigurable optical add/drop multiplexers, and more. The signature (ID) of each sub-system will be generated and stored in a database. The identification of each subsystem ID_i will be evaluated based on a

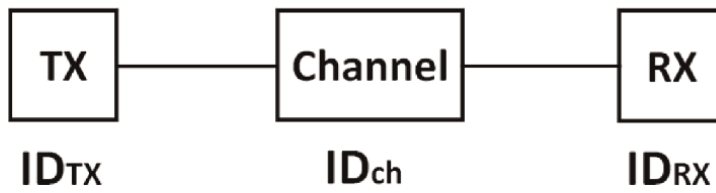

Figure 1.
Point-to-point communications system. ID_{TX}, ID_{Ch}, and ID_{RX} are physical signatures for the transmitter, channel, and receiver, respectively.

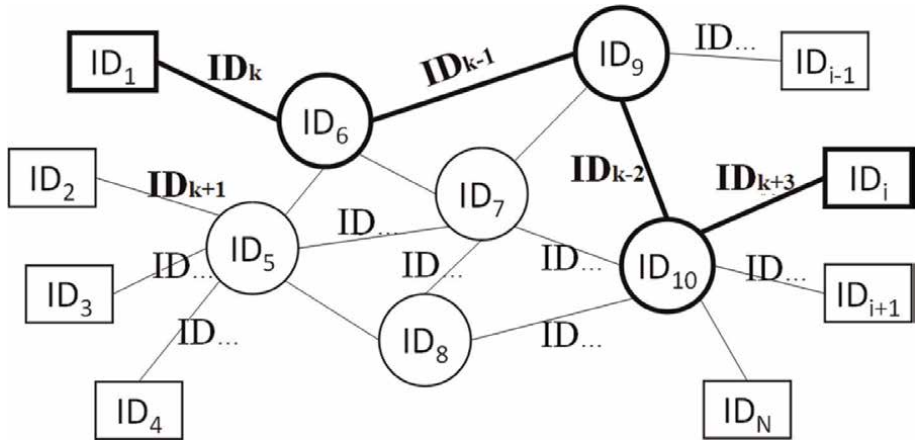

Figure 2.
Network architecture example. Each sub-system has its own physical signature (ID), including transceivers, nodes, and links.

certain probability (P_i), which represents the likelihood of the ID being correct. Any sub-system within the network has the capability to identify other sub-systems and, if necessary, validate each sub-system or even the entire path. In **Figure 2**, a specific path is highlighted in bold. ID_1 has a connection with ID_i through ID_k, ID_6, ID_{k-1}, ID_9, ID_{k-2}, ID_{10}, and ID_{k+3}. Similar to the previous scenario of point-to-point communication, in this case as well, there is a possibility that ID_1 may want to verify the path and/or receiver (IDi). ID_1 will have the capability to evaluate the probability "Pi" for each identification, indicating the likelihood that the sub-system is the expected one. In the case of independent interrogation of sub-systems, it will be easy to evaluate the probability of any sub-set of subsystems or even the entire path by simply multiplying independent probabilities. Thus, the probability can be calculated as follows:

$$p_{path} = \prod_{i \epsilon \{path\}} p_i \tag{3}$$

where P_{path} represents the probability of passing through all subsystems included in the path. In the real system, $P_i < 1$ so that even $P_{path} < 1$. By utilizing the thresholding operation, it is possible to validate the security of the path (as well as the individual sub-systems) with a specific probability. Furthermore, with the capability to independently acquire the fingerprint of each individual sub-system, the system can identify whether any changes have occurred in the path and discover the location of the changes. This approach provides a robust framework for enhancing, authentication, identification, and monitoring. In a more generic approach, it is important to note that the acquisition of signatures may exhibit correlation, rendering them no longer independent. In this case, a more intricate model based on the specific identification technique must be developed, However, we postpone this approach to future studies.

In both scenarios, in the ideal case when a perfect match is achieved ($P_x = 1$), security is guaranteed, and five operations become possible:

1. *Layer security*: If an attack is conducted on one of the identified sub-systems, the match is disrupted, and the attack is unsuccessful.

2. *Authentication*: Authentication can be automatically provided once the sub-system is securely identified.

3. *Identification*: Once the sub-system is securely identified, authentication can be automatically granted.

4. *Monitoring*: By continuously verifying the signature, any changes in the system can be identified.

5. *QoT estimation*: The identification method based on "signature" could enhance the accuracy of estimation.

Regarding network device census [35], it is common for the network operators to have limited knowledge of all the fiber types deployed in a network. This situation poses challenges to the quality of transmission estimation, leading to increased estimation inaccuracies. As a result, network operators may need to adopt higher network margins than initially anticipated, with a consequent underestimation of the optical reach and an increase in the costs for regeneration [36].

We consider the Rayleigh backscattering pattern (RBP), which is a robust OPUF, due to the inherent imperfections in the fabrication process to generate the fingerprint. The RBP of an optical fiber can be measured using optical frequency domain reflectometry OFDR, and this measurement can be converted into a digital signature, which becomes the unclonable and unique signature of each sub-system. In the next sections generating a signature (ID) will be explained in detail.

3.2 Signature

We propose to use the Rayleigh backscattering pattern (RBP) as a signature of the optical fiber. This approach enables us not only to identify the fiber link but also to identify any optical and optoelectronic sub-systems through their pigtail. The Rayleigh backscattering phenomenon that occurs when optical fibers are stimulated by propagating light is an optical physical unclonable function (OPUF), due to the random density fluctuations caused by the fabrication process [37]. The acquisition of RPB can be accomplished through the utilization of an optical frequency or time domain reflectometry (OFDR or OTDR) technique [38, 39]. In this work, we consider the coherent OFDR (COFDR) since it allows us to increase the sensitivity and resolution [40, 41]. COFDR is implemented as follows:

1. A continuous wave (CW) laser emitting light with an amplitude of E_0 is used in the experiment. The laser frequency is linearly swept over time with a sweep rate of γ, and propagates into the fiber under test (FUT).

2. The RBP refers to the photocurrent obtained after self-coherent balance detection. It can be mathematically modeled as follows:

$$I(t) = E_0^2 \sum_{i=1}^{n} \sqrt{R_i} \cos\left(2\pi\gamma t \tau_i\right) \tag{4}$$

when there are n reflection points with reflectivity R_i and roundtrip time τ_i [37, 41].

It should be noted that in this work, the random phase noise is disregarded, and all signatures are simulated based on a fiber pigtail length of 0.5 m. The RBP is measured using the COFDR technique with a sweep time of 0.5 s. For long-distance measurements, where the distance exceeds half of the laser coherence length, it is crucial to appropriately compensate for phase noise and frequency sweeping nonlinearity. This compensation method is described in detail in ref. [41].

The RBP-based signatures rely on the OPUF challenge-response protocol. Thus, any stimulus (called challenge) maps a unique result (called response) and provides a challenge-response pair (CRP). The following CRP protocol procedure is to generate the signature:

Challenge (C): The frequency-modulated continuous wave (FMCW) parameters on the Tx side represent the challenge.

Challenge parameters: (i) sweep rate (γ=Hz/s), which indicates the rate at which the frequency changed in FMCW; (ii) sweep range ($\Delta F=\lambda_{stop}-\lambda_{start}$), which indicates the distance between the start and stop wavelength in FMCW; and the value of (iii) stop and (iv) start sweep wavelengths. Every single parameter has an important role in the spatial resolution and quality of the obtained RBP. This fact is beyond the scope of this work and is clarified in ref. [41].

Response (R): The obtained RBP represents the response.

By changing FMCW parameters, that is, changing the challenge, the RBP will change accordingly. Therefore, if we stimulate the fiber with various challenges, we can extract different RBP patterns from the same fiber. It is important to note that due to the characteristics of the PUF, each challenge will result in a unique response, meaning that different challenges will not produce the same response (as illustrated in **Figure 3**). As a result of this characteristic, even if an adversary gains access to the fiber, they cannot generate the desired signature without using the correct challenge.

To generate the signature, only a single challenge (e.g., C_1) will be applied, and the corresponding response (e.g., R_1) will be used to create the binary signature (ID), which will then be stored in the database (**Figure 4**). For identification, the same challenge will be used.

Using a single-bit analog-to-digital converter (ADC), the RBP is digitized with N samples. Part of the RBP will be selected to generate the binary signal [42]. Depending on the scenario and type of signature, it is straightforward to use quick response (QR) codes to represent signatures.

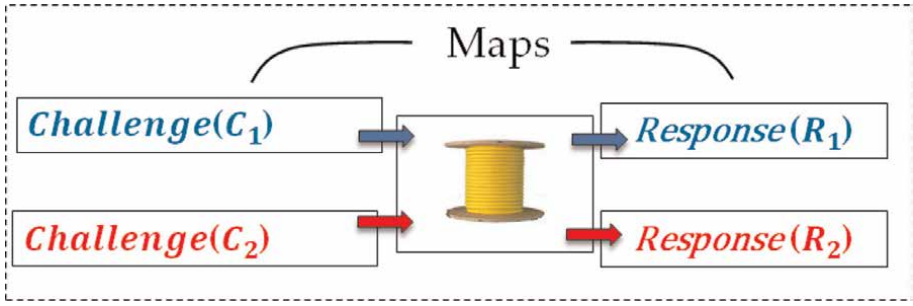

Figure 3.
By changing the challenge, the response will be changed. Therefore, even if the adversary has access to the fiber, he cannot generate the intended signature without applying the correct challenge.

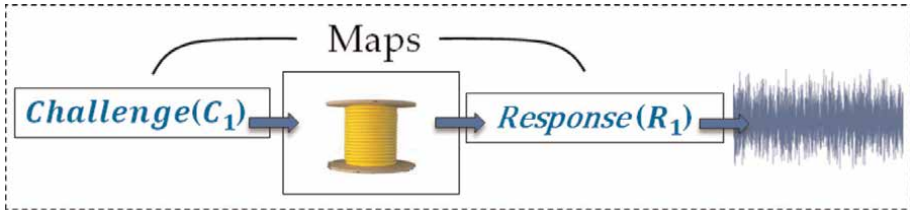

Figure 4.
OPUF protocol to generate OPUF-based signature. Challenge 1 (C_1) ends with response 1 (R_1), which is a specific pattern of RBS of fiber (shown in blue) associated with the specific challenge C_1.

4. System identification and performance evaluation

The identification process can be carried out using either Hamming distance (HD) [43] or the Pearson cross-correlation coefficient (XCOR-C) [42] between the stored signature and the intended signature. Both techniques thoroughly enable us to distinguish the noisy signature from the imposter one, as illustrated in **Figure 5**.

In both techniques, it is possible to define a threshold (TH) can be defined to determine whether the signature should be accepted or rejected as genuine Consequently, the decision rule will be as follow for each method:

XCOR-C: if obtained *XCOR-C,* between the intended signature and the original one, is below a certain threshold, the signature will be considered an imposter. Conversely, if the XCOR-C is above the TH, it will be deemed a genuine signature (**Figure 5a**).

HD: if obtained *HD,* between the intended signature and the original one, is beyond a certain threshold, the signature will be considered an imposter. On the other hand, if it is below the TH, it will be deemed genuine (**Figure 5b, c**).

In order to successfully implement the identification process, it is essential for the acquired signatures to be reproducible. This means that when measurements are taken at different times, they should consistently result in the same signature as the original one stored in the database. Due to the measurement noises, there may be slight deviations between the obtained signature and the original one. However, these deviations are still discernible and distinguishable from the imposter signature. This fact has been

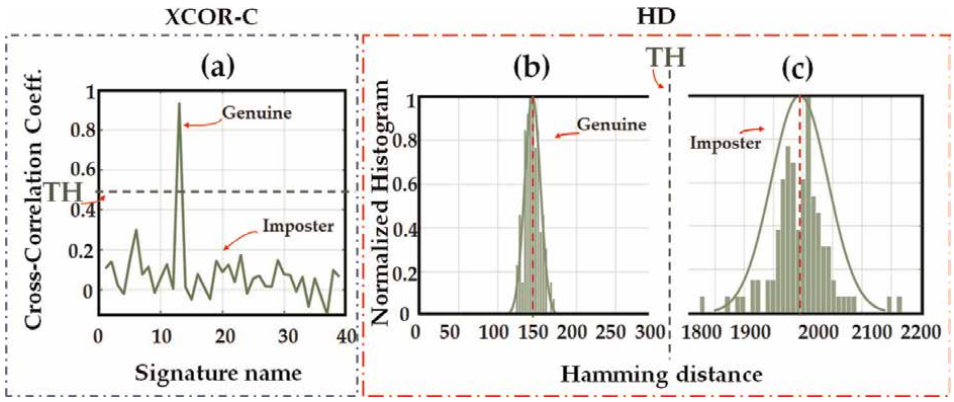

Figure 5.
Two different identification methods: Cross-correlation coefficient (XCOR-C) between the original signature, (a) and a bunch of signatures, that among them the genuine signature is detected (peak). The histogram of hamming distance (HD) between original signature, (b) and a bunch of noisy signatures (mean 144), (c) and a bunch of imposters (mean 1994). Defined threshold: Green dashed line.

shown in **Figure 5b, c**. Regarding **Figure 5b, c**, the mean value of the HD histogram of the noisy signatures is about 144, while the mean value of the HD histogram of the imposter signatures is around 1994. This fact demonstrates the reproducibility as well as the level of security of signatures. The security of the generated signatures relies on the intrinsic unclonability of the OPUF [44–46]. That means the obtained signatures are unique, unclonable, and unpredictable either digitally or physically.

To describe the security validation technique, we assume to have a long binary word provided by the process of fingerprint identification. Such ID is encoded and converted to the two-dimensional (2D) binary image comprising 60 × 60 pixels, **Figure 6**. To assess the robustness of the IDs against digital cloning, we conducted an investigation into their resistance to brute force trials (BFT attacks). This type of attack requires nondeterministic exponential time for data decryption, which shows their robustness in front of digital cloning. We investigate the security level of the generated ID (QR code) against BFTs by considering the number of identical bits in each row of the code with the following process.

The encoded binary image was divided into 60 one-dimensional segments (rows), each including 60 bits, **Figure 6**. Therefore, according to Eq. (5), there are $C_k(n)$ pairs of 1D segments, $C_2(60) = 1770$ pairs for each binary image of 60×60 bits.

$$C_k(n) = \frac{n!}{k!(n-k)!} \tag{5}$$

As a metric for security validation, we consider the Hamming distance between the pairs of 1D segments. The Hamming distance between a pair of 1D segments refers to the number of nonidentical bits that need to be flipped in order for two segments to be similar. The crucial point is that 1D segments with too short or too long Hamming distances are relatively easy to decipher through BFTs, where a Hamming distance equal to half of the segment length ensures maximum uniqueness [47].

The Hamming distance histogram of 1770 segment pairs is illustrated in **Figure 7**, which goes like a Gaussian distribution with a mean value of around 29, ensuring close to maximum uniqueness of the 1D segments. The histogram demonstrates the need for a large number of BFT trials to decipher a single segment of a binary image. This indicates that a significant number of BFTs would be required to decipher the entire 2D image. (i.e., ID).

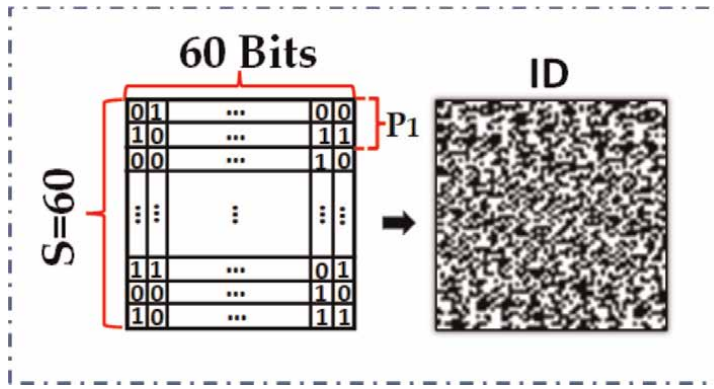

Figure 6.
The system's ID. (left) 2D binary ID data consists of 60 segments (S), each including 60 bits (60×60) bits. (right) the QR code. P1: A pair of sequences.

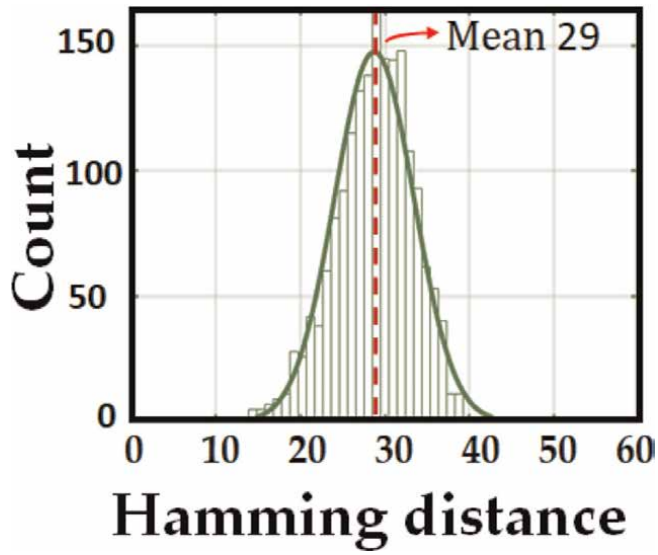

Figure 7.
Validation of the ID robustness against BFT attacks. Histogram of the hamming distance between the $C_2(60) = 1770$ pairs of 1D segments. The obtained mean value is about 29 using a Gaussian fit, which shows close to maximum uniqueness for the 1D segment, and thus for the ID (2D).

It should be noted that the signature length can be defined based on the expected level of security from the signatures [42].

5. Discussion

Based on the proposed technique, any network or its fiber-optical constituent element can be identified and authenticated. Thereby, any attack, whether physical or digital, can be detected. Physically invading the system will cause a change in the system signature that could confirm the presence of an imposter. Even digital invaders with advanced machine learning (ML) knowledge cannot predict the system's signature [48] since every system or device has its unique and unpredictable signature.

Device identification (DI) through optical identification (OI) through the optical signature is a perfect security complementary tool to the networks and guarantees the security of the systems, sub-systems, and devices. Such a DI identification method may find applications within several use cases. It can be used in applications related to classic network security, Quantum network security [43], network census, or network quality of transmission (QoT) [42, 49]. Depending on the scenarios, applications, and the required level of security, the CRP database will be generated and used for identification implementation. Regarding network security, OI can be implemented for different network scenarios [49] to identify, authenticate, and monitor networks.

6. Conclusion

This chapter introduces the concept of optical identification (OI) for network security purposes at the physical layer in optical communication systems and networks. The unique fingerprint of each physical subsystem enables direct

identification, offering new strategies for transmission security, layer security, authentication, identification, and monitoring. This approach allows for the identification of each network's component just using its pigtail (or the fiber itself for a link), without the need for an additional device operating directly at the physical layer. Such a novel security layer concept will play a key role when linked to other security strategies that come from upper OSI layers.

This approach might open an innovative way to impact network security at several layers. The reproducibility and uniqueness of the IDs' have been demonstrated using Hamming distances, ensuring reliable identification. The security validation of the proposed model has been investigated, demonstrating its robustness against various attack types, both physical and digital. The proposed model encompasses various methods and strategies for generating and exerting identification databases.

Future works will be dedicated to extending the technique applications and to further investigating the signature robustness against malicious attacks. These ongoing efforts aim to enhance the security performance of the proposed model and pave the way for new advancements in the field of network security.

Acknowledgements

This research was funded by HORIZON-JU-RIA (101096909), HORIZON-RIA (101092766), it was also partially supported by project SERICS (PE00000014) under the NRRP MUR program funded by the EU - NGEU.

Conflict of interest

The authors declare no conflict of interest.

Author details

Pantea Nadimi Goki[1,2*], Thomas Teferi Mulugeta[2], Nicola Sambo[2], Roberto Caldelli[3,4], Ramin Solaimani[4] and Luca Potì[1,4]

1 CNIT Photonic Networks and Technologies PNT Lab, Pisa, Italy

2 TeCIP Institute Scuola Superiore Sant'Anna, Pisa, Italy

3 Florence Research Unit CNIT, Florence, Italy

4 Universitas Mercatorum, Rome, Italy

*Address all correspondence to: pantea.nadimigoki@santannapisa.it

IntechOpen

References

[1] Andy H. Fiber optic cable market-growth, trends, Covid19 impact, and forecast (2021-2026). Mordor Intelligence; 2021. Report ID: 4773602

[2] Wyner AD. The wire-tap channel. Bell System Technical Journal. 1975; **54**(8):1355-1387

[3] Zhou X, McKay MR. Secure transmission with artificial noise over fading channels: Achievable rate and optimal power allocation. IEEE Transactions on Vehicular Technology. 2010;**59**(8):3831-3842

[4] He J, Giddings R, Jin W, Tang J. DSP-based physical layer security for coherent optical communication systems. IEEE Photonics Journal. 2022; **14**(5):1-11

[5] Lei C, Lin R, Li Y, Wang B, Zhang M, Zhao Y, et al. Integration of self-adaptive physical-layer key distribution and encryption in optical coherent communication. Journal of Lightwave Technology. 2023:1-8. DOI: 10.1109/JLT.2023.3257963

[6] Gidney C, Ekerå M. How to factor 2048 bit RSA integers in 8 hours using 20 million noisy qubits. Quantum. 2021;**5**:433

[7] Gong Y, Wonfor A, Hunt JH, Penty R. Physical layer security monitoring of optical communication using a quantum pilot tone signal. In: Conference on Lasers and Electro-Optics (2022), Paper FTu4A4 [Internet]. San Jose, California United States: Optica Publishing Group; 2022. p. FTu4A.4. Available from: https://opg.optica.org/abstract.cfm?uri=CLEO_QELS-2022-FTu4A.4 [cited 2023 Jun 7]

[8] Bennett CH, Brassard G. Quantum cryptography: Public key distribution and coin tossing. Theoretical Computer Science. 2014;**560**(1):7-11. DOI: 10.1016/j.tcs.2014.05.025

[9] Cavaliere F, Prati E, Poti L, Muhammad I, Catuogno T. Secure quantum communication technologies and systems: From labs to markets. Quantum Reports. 2020;**2**(1):80-106

[10] Chen L, Jin W, He J, Giddings RP, Huang Y, Tang J. A Point-to-multipoint Flexible Transceiver for Inherently Hub-and-Spoke IMDD Optical Access Networks. Journal of Lightwave Technology. DOI: 10.1109/JLT.2023.3249406

[11] Wang L, Mao X, Wang A, Wang Y, Gao Z, Li S, et al. Scheme of coherent optical chaos communication. Optics Letters. 2020;**45**(17):4762-4765

[12] Antonik P, Gulina M, Pauwels J, Rontani D, Haelterman M, Massar S. Spying on Chaos-Based Cryptosystems with Reservoir Computing. In: International Joint Conference on Neural Networks (IJCNN) 2018. Rio de Janeiro, Brazil: IEEE; 2018. pp. 1-7

[13] Liang X, Zhang C, Luo Y, Wang X, Qiu K. Secure encryption and key management for OFDM-PON based on chaotic Hilbert motion. Journal of Lightwave Technology. 2023;**41**(6): 1619-1625

[14] Chen W, Mu P. Research on methods of enhancing physical layer security of optical fiber communication system in the smart grid. Journal of Physics: Conference Series. 2022;**2237**(1): 012002. DOI: 10.1088/1742-6596/2237/1/012002

[15] Jiang N, Zhao A, Liu S, Zhang Y, Peng J, Qiu K. Injection-locking chaos

synchronization and communication in closed-loop semiconductor lasers subject to phase-conjugate feedback. Opt Express, OE. 2020;**28**(7):9477-9486

[16] Wohlgemuth E, Yoffe Y, Attia I, Imran M, Lakshmijayasimha PD, Marotta A, et al. A field trial of multi-homodyne coherent detection over multi-Core Fiber for encryption and steganography. Journal of Lightwave Technol, JLT. 2023;**41**(9):2723-2735

[17] Wu B, Wang Z, Tian Y, Fok MP, Shastri BJ, Kanoff DR, et al. Optical steganography based on amplified spontaneous emission noise. Optics Express, OE. 2013;**21**(2):2065-2071

[18] Rout H, Mishra BK. Pros and cons of cryptography, steganography and perturbation techniques. IOSR Journal of Electronics and Communication Engineering. 2014;**9**(2):76-81

[19] Mishra R, Bhanodiya P. A review on steganography and cryptography. In: International Conference on Advances in Computer Engineering and Applications 2015. Ghaziabad, India: IEEE; 2015. pp. 119-122

[20] Kamal YK, Muresan R, Al-Dweik A. CMOS-based physically unclonable functions: A review and tutorial [Internet]. 2021 Jun [cited 2023 Jun 7]. Available from: https://www.techrxiv.org/articles/preprint/CMOS-Based_Physically_Unclonable_Functions_A_Review_and_Tutorial/14753109/1

[21] Tarik FB, Famili A, Lao Y, Ryckman JD. Scalable and CMOS compatible silicon photonic physical unclonable functions for supply chain assurance. Scientific Reports. 2022;**12**(1):15653

[22] Zhang L, Fong X, Chang CH, Kong ZH, Roy K. Highly reliable memory-based Physical Unclonable Function using Spin-Transfer Torque MRAM. In: 2014 IEEE International Symposium on Circuits and Systems (ISCAS). Melbourne, VIC, Australia: IEEE; 2014. pp. 2169-2172

[23] Mesaritakis C, Akriotou M, Kapsalis A, Grivas E, Chaintoutis C, Nikas T, et al. Physical Unclonable function based on a multi-mode optical waveguide. Scientific Reports. 2018;**8**(1):9653

[24] Shakiba-Herfeh M, Chorti A, Vincent Poor H. Physical Layer Security: Authentication, Integrity, and Confidentiality. In: Le KN, editor. Physical Layer Security. Cham, Switzerland: Springer International Publishing; 2021. pp. 129-150. DOI: 10.1007/978-3-030-55366-1_6

[25] Rothe S, Koukourakis N, Radner H, Lonnstrom A, Jorswieck E, Czarske JW. Physical layer security in multimode Fiber optical networks. Scientific Reports. 2020;**10**(1):2740

[26] Horstmeyer R, Judkewitz B, Vellekoop IM, Assawaworrarit S, Yang C. Physical key-protected one-time pad. Scientific Reports. 2013;**3**(1):3543

[27] Silvério T, Dias LMS, Ramalho JFCB, Correia SFH, Fu L, Ferreira RAS, et al. Functional mobile-based two-factor authentication by photonic physical unclonable functions. AIP Advances. 2022;**12**(8):085316

[28] Du Y, Jothibasu S, Zhuang Y, Zhu C, Huang J. Unclonable optical Fiber identification based on Rayleigh backscattering signatures. Journal of Lightwave Technology, JLT. 2017;**35**(21):4634-4640

[29] Nikolopoulos GM, Fischlin M. Quantum key distribution with post-processing driven by physical unclonable

functions [Internet]. arXiv; 2023 [cited 2023 May 31]. Available from: http://arxiv.org/abs/2302.07623

[30] Herder C, Yu MD, Koushanfar F, Devadas S. Physical Unclonable functions and applications: A tutorial. Proceedings of the IEEE. 2014;**102**(8): 1126-1141

[31] Jain AK, Deb D, Engelsma JJ. Biometrics: Trust, but verify. IEEE Transactions on Biometrics, Behavior, and Identity Science. 2022;**4**(3):303-323

[32] Kong J, Koushanfar F. Processor-based strong physical Unclonable functions with aging-based response tuning. IEEE Transactions on Emerging Topics in Computing. 2014;**2**(1):16-29

[33] Pappu R, Recht B, Taylor J, Gershenfeld N. Physical one-way functions. Science. 2002;**297**(5589): 2026-2030

[34] Chen M, Fridrich J, Goljan M, Lukas J. Determining image origin and integrity using sensor noise. IEEE Transactions on Information Forensics and Security. 2008;**3**(1):74-90

[35] Seve E, Pesic J, Delezoide C, Giorgetti A, Sgambelluri A, Sambo N, et al. Automated Fiber type identification in SDN-enabled optical networks. Journal of Lightwave Technology. 2019;**37**(7):1724-1731

[36] Soumplis P, Christodoulopoulos K, Quagliotti M, Pagano A, Varvarigos E. Network planning with actual margins. Journal of Lightwave Technology. 2017; **35**(23):5105-5120

[37] Ding Z, Yao XS, Liu T, Du Y, Liu K, Jiang J, et al. Compensation of laser frequency tuning nonlinearity of a long range OFDR using deskew filter. Opt Express, OE. 2013;**21**(3):3826-3834

[38] Zhao S, Cui J, Suo L, Wu Z, Zhou DP, Tan J. Performance investigation of OFDR sensing system with a wide strain measurement range. Journal of Lightwave Technology, JLT. 2019;**37**(15):3721-3727

[39] Tsuji K, Shimizu K, Horiguchi T, Koyamada Y. Coherent optical frequency domain reflectometry for a long single-mode optical fiber using a coherent lightwave source and an external phase modulator. IEEE Photonics Technology Letters. 1995;**7**(7):804-806

[40] Ito F, Fan X, Koshikiya Y. Long-range coherent OFDR with light source phase noise compensation. Journal of Lightwave Technology. 2012;**30**(8): 1015-1024

[41] Nadimi Goki P, Mulugeta TT, Caldelli R, Potì L. Optical systems identification through Rayleigh backscattering. Sensors. 2023;**23**(11):5269

[42] Nadimi Goki P, Civelli S, Parente E, Caldelli R, Mulugeta TT, Sambo N, et al. Optical identification using physical unclonable functions. Journal of Optical Communications and Networking. [Internet]. 2023;**15**(10). DOI: 10.1364/JOCN.489889

[43] Peterson E. Developing Tamper-Resistant Designs with Zynq UltraScale+ Devices [Internet]. 2018. Available from: https://docs.xilinx.com/v/u/en-US/xapp1323-zynq-usp-tamper-resistant-designs [Accessed: 2023-7-13]

[44] Rührmair U, Devadas S, Koushanfar F. Security based on physical unclonability and disorder. In: Introduction to hardware security and trust. New York, United States: Springer; 2011. pp. 65-102

[45] Wali A, Dodda A, Wu Y, Pannone A, Reddy Usthili LK, Ozdemir SK, et al.

Biological physically unclonable function. Communications on Physics. 2019;**2**(1):1-10

[46] Pavanello F, O'Connor I, Rührmair U, Foster AC, Syvridis D. Recent Advances in Photonic Physical Unclonable Functions. In: 2021 IEEE European Test Symposium (ETS). Bruges, Belgium: IEEE; 2021. pp. 1-10

[47] Nadimi Goki P, Mulugeta TT, Sambo N, Caldelli R, Potì L. Network Authentication, Identification, and Secure Communication through Optical Physical Unclonable Function. In: European Conference on Optical Communication (ECOC) 2022 (2022), paper We565 [Internet]. Basel, Switzerland: Optica Publishing Group; 2022. p. We5.65. Available from: https://opg.optica.org/abstract.cfm?uri=ECEOC-2022-We5.65 [cited 2023 May 31]

[48] Poti L, Nadimi Goki P, Mulugeta TT, Sambo N, Caldelli R. Optical fingerprint: A possible direction to physical layer security, authentication, identification, and monitoring. In: 2022 61st FITCE International Congress Future Telecommunications: Infrastructure and Sustainability (FITCE) [Internet]. Rome, Italy: IEEE; 2022 [cited 2023 Jun 7]. pp. 1-6 Available from: https://ieeexplore.ieee.org/document/9934467/

[49] Nadimi Goki P, Mulugeta TT, Sambo N, Caldelli R, Potì L. Optical Network Authentication through Rayleigh Backscattering Fingerprints of the Composing Fibers. In: GLOBECOM 2022 - 2022 IEEE Global Communications Conference. Rio de Janeiro, Brazil: IEEE; 2022. pp. 2146-2150

Section 3

Perspective

Chapter 7

Perspective Chapter: Optoelectronics for Neural Interfaces

Abhivyakti Gautam

Abstract

Optoelectronics for neural interfaces is a growing field developing light-based methods for recording and stimulating neural activity. It has the potential to revolutionize the treatment of neurological disorders. The chapter will delve into optoelectronics' basic principles, its applications, and various devices such as implantable optical fibers, microelectrode arrays, and integration with flexible materials. The chapter will highlight the challenges and opportunities facing the field, such as developing small, flexible, and biocompatible devices, controlling light delivery, understanding optogenetic stimulation effects and their scalable integration to achieve high spatiotemporal precision and low invasiveness. Despite challenges, optoelectronics for neural interfaces is a promising approach that could open up new avenues to restore vision to the blind, control prosthetic limbs, and treat diseases like epilepsy.

Keywords: optical neural stimulation, implantable optoelectronics probes, flexible microelectrode arrays, neurological disorders, brain-computer interface

1. Introduction

Human nervous system is made up of billions of neurons that communicate with each other through multiple synapses and therefore create vast web of neural networks, making the brain an exceptionally powerful system. Understanding correlation between animal behavior and these neuronal pathways is one of the primary aim of neuroscience. Another research domain called Brain Computer Interface (BCI), aims to form a direct hardware-based communication link between the brain and the external world. As input, these systems convert the electrical activity from neuron and translate it to control signals, which are used to connect with an external assistive device. BCI systems range from implantable electrocardiography (ECoG) to neuroprosthetics that can rehabilitate vision and hearing. These systems can be utilized to improve our understanding of organization and operation of nervous system and may lead to advancing the current state-of- the-art technologies for treating severe neurological disorders such as paralysis, Alzheimer's disease etc. To achieve this, development of multimodal systems, with capability to record and regulate activities of target neurons is required.

Optoelectronic devices have become ubiquitous in our daily lives, seamlessly integrated into consumer electronics, communication systems, automobiles, and medical

technologies. Their remarkable versatility and ability to bridge the gap between light and electricity have opened a world of possibilities, revolutionizing various aspects of modern life. Optogenetics combines genetic and optical techniques to control neural activities with light. It is a promising tool for selectively targeting nerve cells that allow extensive studies of cell activity which can eventually be extended to neural network connectivities. In more detail, light sensitive ion channels called opsins are injected into target tissue. These opsins are extracted from algae or bacteria and light activation can be of excitatory (e.g. channelrhodopsin i.e. ChR2) or inhibitory (e.g. halorhodopsin i.e. NpHR) nature [1–3]. Therefore, in contrast to traditional electrical stimulation where the surrounding electrode tissue is also affected by the stimulation, optogenetics permits regulation of neural activity with both cell-type specificity and high temporal resolution.

High spatiotemporal resolution is essential to track neuronal activity in order to understand how information is regulated in neural networks. MEAs can be used to detect extracellular action potentials (APs) as well as transient electrical signals generated from summation of excitatory and inhibitory potentials from a cluster of neurons called as local field potentials (LFPs). Synchronous recording and modulation of specific neuronal population in target tissue can be achieved with integration of electrical recording and optogenetic capabilities. This is important to establish their role in information regulation process and therefore gain further insights into animal behavior [4, 5].

Research in the last decade has indicate that integrating electrophysiology and optogenetics capabilities has created a powerful tool to enhance our understanding of neural activity, behavioral outputs as well as sources of defects in nervous system that lead to neurological disorders [6–8]. However, substantial challenges exist in current combined optogenetics & electrophysiology techniques which need to be addressed. This chapter delves into advances in implantable neural probes along with their material and design requirements. It further provides an overview of recent developments in multimodal neural probes for simultaneous optoelectronic modulation and recording via two distinct approaches i.e. using active and passive optical probes. Finally, challenges faced and potential opportunities of further developing these multimodal neural interfaces to potentially use for clinical applications is discussed.

2. Neural Interface technology

2.1 Advancement of microelectrode arrays (MEAs)

Neural prosthetics are BCI devices intended to revive the lost functionality of motor or sensory organs in patients suffering from neural injuries and disorders. Advancement of fabrication of neural prosthetics from single channel devices to flexible Microelectrode arrays (MEAs) consisting of few hundred to thousands of channels (thus improving spatial resolution of input electrical signal as well as the signal-to-noise ratio) has made the clinical applications of these devices more viable. These arrays can be utilized for recording neuronal activity to aid in gaining further insights into functioning of specific areas of the brain, that may eventually lead to diagnosis of neurodegenerative diseases. Another application of these arrays involves electrical stimulation of the brain by injecting electrical impulses with an aim to restore degenerating or impaired motor systems by activating damaged neurons and creating an alternate neural pathway. Additionally, these arrays can also be used for detection of neurotransmitters, which has been an effective approach to gain a better

understanding of neurological disorders such as Alzheimer's disease, Parkinson's disease as these are characteristically associated with imbalance. Another interesting area of research using these arrays is the field of drug delivery which has been plausible by addition of microfluidic channels [9].

Microelectrode arrays (MEAs) have been employed for neural recording and stimulation application with different degrees of precision and invasiveness [10]. For example, Electroencephalography (EEG) electrodes which is non-invasive as the electrodes are implanted on the surface of the brain and thus offer low-resolution data of smoothed field potentials representative of neural activity of the whole cortical surface. Electrocorticography (ECoG) electrodes which is semi-invasive as the electrodes may be positioned outside the dura mater (epidural) or under the dura mater (subdural) and it requires craniotomy for implantation of the electrodes and multiple layers of cortical laminae can be targeted with different designs (e.g. shank type) of electrodes. These provide higher temporal and spatial resolution and are routinely used to identify seizure loci in epilepsy patients [11].

Accurate mapping of neural activity is of significant clinical importance extending beyond the cortex to encompass deep brain regions (such as the subthalamic nucleus in individuals with Parkinson's disease), the spinal cord, and peripheral nerves (particularly in cases of trauma or chronic pain). Furthermore, many nervous system related disorders are associated with atypical activity in specific neuronal classes, justifying the critical need to achieve single-neuron resolution for development of effective therapeutic strategies.

2.2 Material and design requirements for MEAs

Essential requirements for a prospective material for neural probes are as follows:

The material must be biocompatible in order to promote seamless integration with neurons and therefore minimize foreign-body response by causing minimal inflammation and neuronal cell loss.

- The material must be exhibit adequate mechanical strength to withstand compression and tension forces during insertion and retraction stages of implantation procedure. Additionally, it must decrease the mechanical mismatch between the sensing electrode material and the surrounding tissue for suppressing chronic tissue encapsulation.

- The material must be able to inject sufficient charge in the surrounding tissue to cause electrical brain stimulation at clinically relevant charge densities without causing any significant tissue damage due to corrosion or delamination of insulating or substrate layers of the implant.

- During stimulation operation, irreversible reaction should not occur in the brain i.e. the material should have the ability to provide safe levels of therapeutic stimulation.

- The material should be able to withstand implantation as well as exhibit stable electrochemical characteristics for long-term.

Materials for neural probes can be categorized based on their mechanism of charge injection during stimulation i.e. capacitive or faradaic. Capacitive charge injection

involves charging and discharging of the electrode-electrolyte (in-vitro testing) or electrode-tissue (in-vivo testing) double layer while the faradic charge injection involves transfer of electrons resulting in oxidation or reduction of surface bound species. Examples of some capacitive charge-injection materials employed for the purpose of neural stimulation are Titanium nitride, Tantalum/Tantalum oxide while some of the Faradaic materials include noble metals like Platinum and Platinum-iridium alloys, Iridium-oxide, PEDOT. Some of the common materials used for recording electrodes are stainless-steel, tungsten, PEDOT, platinum, platinum-iridium alloys [9].

3. Integration of optoelectronics

As the field of optogenetics has progressed, it has become possible to selectively excite or inhibit specific neurons with millisecond precision [2, 12]. This is realized by genetically targeting light-sensitive proteins called 'opsins' (extracted from algae or bacteria) to demonstrate neuronal response (sensitivity) to various wavelength in visible spectrum of light. Opsins can play excitatory (e.g. channelrhodopsin i.e. ChR2) or inhibitory role (e.g. halorhodopsin i.e. NpHR) based on application of interest. Optogenetics offers a distinct advantage over the electrical stimulation by enabling the precise activation of specific target cell population without impacting the surrounding tissue [13].

A major challenge for these light-based techniques is the highly scattering and absorptive behavior of mammalian tissue in the visible light range, especially in deep neural tissue. Therefore, inclusion of optical waveguides or light emitting device integrated at site of intervention is essential for efficient light delivery and collection within deep tissue. Materials, design and biocompatibility considerations must be addressed for these waveguides similar to considerations for neural recording and stimulation electrodes.

Factors such as proposed implantation site and therefore volume and density of neuron population to be optically stimulated, dictates the required size and illumination area for optical part of probe. Based on the mechanism of light source, probes can be categorized as 'Passive optical neural probes' which route light into tissue from light sources located outside the body while 'Active optical neural probes' where light source directly assembled on source. Using passive probes minimizes the risk of thermal damage to the tissue as the light source is located outside the body while active implants generate light directly inside tissue by converting electricity to light.

3.1 Passive optical neural probes

Essential requirement of optical waveguide for passive optical neural probes is a high refractive index core engulfed by a lower refractive index cladding layer to support optimal transmission of light to the desired neuronal population in target area. Materials exhibiting this behavior in addition to flexibility and biocompatibility, as described in Section 2.2, are needed to form a flexible optical waveguide to integrate into neural implants. As silicon micromachining has the longest history of producing successful neural probes and allows easy integration of electronic circuity, it was a go-to choice as a substrate material in many designs [14, 15]. Other examples include use of silicon dioxide, silicon nitride and zinc oxide as waveguide materials [16].

Alternatively, polymer materials like SU8, Parylene and ORMOCER [17–22] have been used but transparency in most cases is not as high as silicon-based materials.

Using silicon as a substrate is a well-established practice, but it's known for its rigidity, which could potentially result in elevated foreign body responses when compared to more pliable materials. As an alternative substrate, polymers have been employed, featuring integrated waveguides and the possibility of fluidic channels for precise vector injection during optical stimulation and electrical recording at the desired location.

Polymer probes are preferred due to their flexibility and reduction in mechanical mismatch to the tissue i.e. polymers are less stiff than silicon but their flexibility i.e. Young's modulus is still some orders of magnitude larger than nervous tissue. Additionally, larger attenuation of light is observed in polymers as compared to waveguides based on dielectrics. Parylene photonic waveguides have been implemented by [20, 23] where Parylene N is used as core and Parylene C is used as cladding material. A high contrast of refractive index between Parylene-C (used as core here) and PDMS (used as cladding) is favorable and results in highly restricted optical modes [24, 25].

While the overall design of these passive flexible neural probes is important, careful consideration muse be given to the input ports for each optical waveguide. These ports need to be specifically designed to enable efficient light coupling from external backend sources, ensuring optimal performance.

3.2 Active optical neural probes

To avoid connecting an external light source, Active optical neural probes introduce a light source to the neural probe, either in combination with a waveguide or directly on an electrode array. This ensures delivery of light deep into the target tissue with high spatial resolution. These light sources include light emitting diodes (LEDs) or lasers that emit light when powered by electricity [26]. There have been recent developments of implants with LDs and LEDs assembled or monolithically integrated on silicon based as well as polymer-based substrates [18, 27–30].

For example, Gallium Nitride (GaN) LEDs have been utilized in the creating active photonic neural implants that produce blue light within the wavelength spectrum that aligns with the absorption range of Channelrhodopsin (ChR2), a frequently employed opsin in optogenetics, as well as fluorescent markers used for both structural and functional brain imaging. Pre-made LEDs have been packaged with neural probes such that metal traces and bondpads on neural probes are lithographically defined on a polymer substrate and LEDs are subsequently flip-chip bonded onto the polymer via bondpads. This method provides lot of flexibility such that LEDs emitting light at different wavelengths can be integrated on the same array to stimulate different opsins in any arbitrary arrangement, e.g. in cochlear implants [31].

Powering these light sources can result in substantial temperature increment which must be restricted in order to prevent damage to surrounding tissue. To prevent this – pulsing of light pulses can be incorporated rather than continuous use, to keep below the advised temperature increment of ~2 K for medical devices per ISO 14708-1. Additionally, design can be adjusted to incorporate wide spatial distribution between LEDs that stimulate simultaneously by distributing to multiple shanks or levels in the electrode array. Using waveguide internally, light source and illumination volume can be segregated to prevent overheating the tissue [19].

The materials employed for encapsulation, packaging, and waveguides must demonstrate biostability in terms of both insulation and optical transmission to guarantee the extended lifespan of devices during chronic implantation. Recently, a new monolithic fabrication process has been developed where flexible micro-LEDs are directly fabricated on silicon substrate with epitaxially grown GaN layers such

that silicon layer is fully etched to release flexible devices. This approach provides flexibility in terms of size and arrangement of micro-LEDs that can be integrated in conjunction with recording electrodes [32]. Most of the approaches have only been tested for weeks and successful demonstration of reliable stimulation and recording performance is yet to be performed. Apart from shank type arrays, some studies on modification of planar electrodes for electrocardiograms [24, 25, 33, 34] and cuff-electrodes for peripheral nerves [35, 36] with optoelectronic stimulation capabilities are going on. Research efforts in this domain are gaining momentum and progressing along the right trajectory to enhance material capabilities and yield promising results.

4. Challenges and opportunities for optoelectronics in neural interfaces

Neuroscience has significantly progressed with advancement in neural modulation and recording techniques. Specific neuronal populations in target brain regions can be simultaneously recorded and stimulated using multimodal neural interfaces that combine optogenetics with electrophysiology and thus provide a powerful technique for understanding neural circuit functionality. Research and development on the optoelectronic front have emerged relatively recently with promising results for both passive and active optical neural implants. However, many challenges remain to be addressed in the development of multimodal tools for combined optogenetics and electrophysiology. Given the diverse strengths and limitations of each technology platform and their impact on suitability for specific applications, this section compares the current state of passive and active flexible optoelectronic technologies, focusing on the present challenges and opportunities for achieving a high longevity combined optogenetics and electrophysiology platform.

The active optoelectronic implants with micro-LEDs as functional element potentially allow a very high density of light sources. Miniature electrical traces can be densely routed (using advanced lithography techniques) to power these active light sources. On the other hand, passive optoelectronic implants require entire routing from backend to probe shank and cannot be defined over trajectories with sudden sharp bends. However, heat generation and dissipation in the probe shank due to lower efficiency of micro-LEDs is concerning. Temperature change of less than 1°C is prescribed as safe operating condition [37] but it depends upon the duration of exposure as well [38]. Two potential approaches can be adopted to alleviate this – (1) adding a heat-sink layer [39] (2) pulsing active light source to avoid heat accumulation [29]. Different geometric profiles of the micro-LEDs such as integrated planar [40] and hemispherical mirrors [41] have been explored to enhance efficiency of optical stimulation. Additional research is required to improve efficiency of these light sources and control heat dissipation into tissue. Conversely, passive optical waveguides deliver light from external sources to brain regions while minimizing heat transfer to the surrounding tissue in case of passive optoelectronic implants.

Majority of passive flexible optoelectronic interfaces developed so far consist of few optical channels. Miniaturization of waveguide core dimensions and therefore reduction of pitch between adjacent waveguides for high density routing (and therefore high number of channels) is limited by core waveguide materials as well as manufacturing methods. Additional overhead is added from assembly methods for integration of optical elements. Innovative approaches to ease this manufacturing overhead are required. One design-based approach to increase the density of optical

channels, can be exploring multilevel metal traces as well as multilevel photonic guides while maintaining minimal crosstalk between adjacent channels.

Alternatively, a simple thermal drawing process has been explored by Polina et. Al [42], which is inspired by optical fiber production as a method of fabrication for multi-functional neural probes. During this process, using low-end manufacturing processing, a macroscale preform is fabricated which can be drawn into fiber such that lateral dimension can be scaled as much as 10,000-fold using multiple drawing processes & length can be stretched by a factor of ~100. This creates an extended fibrous device where cross-section structures on nanoscale can be created without the need of high-resolution fabrication technology. Another approach to achieve multi-site illumination without modifying the design or fabrication process is wavelength-based multiplexing. This technique involves routing multiple wavelengths of light from a single input waveguide to different output waveguides located at various spatial locations along the probe shank. Each output waveguide then transmits its assigned wavelength to a specific target site, enabling simultaneous stimulation at multiple locations. This unique assignment of different wavelengths neither requires additional power to operate nor generates additional heat [36].

Development of hermetic packaging for both active and passive optoelectronic approaches is another area of focus, where one approach being explored is combining inorganic layers with polymers to protect integrated micro-electronic circuits and conductors [43]. Longevity is a critical aspect to enable transfer of all the exciting approaches to chronic studies. Proof of concept experiments with multimodal process have demonstrated general feasibility such that existing active flexible optoelectronic probes are best suited for acute studies, where high-density light illumination is expected while passive optoelectronic probes have the potential for chronic long-term studies. However, current passive optoelectronic systems are too bulky with fragility concerns regarding the assembly of optoelectronic components to neural probes and therefore challenging to use for the chronic studies in freely behaving animals. Only a few groups have explored passive optoelectronic systems for small animal models [44, 45]. Development of fully implantable systems with wireless power supply and bidirectional data transmission would be the ideal direction to enable translational studies aimed at exploring therapeutic potential of optogenetics and employ miniaturized optoelectronic probes to potentially revolutionize bioelectronic medicine.

5. Conclusion

Progress in the field of neuroscience have been driven by the evolution of techniques for neural recording and stimulation. Multimodal neural probes, seamlessly integrating optoelectronics and electrophysiology, offer the potential for groundbreaking advancements in the field. These probes enable simultaneous recording and stimulation of specific neuronal populations within targeted brain tissue, making them powerful tools for fundamental neuroscientific research. Notably, in a groundbreaking study, Canales et al. (2015) presented a novel multifunctional fiber capable of simultaneously performing optical stimulation, neural recording, and drug delivery [46].

Further research efforts can be directed to development of a high longevity multifaceted probe combining additional capabilities like microfluidic drug delivery to potentially alter gene expression, deliver peptide ligands, and eventually manipulate animal behavior. Implementing these modalities with optoelectronics

and electrophysiology, especially wirelessly [5, 47–49] is extremely challenging but if executed, it holds massive potential to enhance our understanding of mysteries of the brain and potentially develop promising solutions for diagnosis and treatment of neurological disorders.

Author details

Abhivyakti Gautam
Independent Researcher, Fremont, CA, USA

*Address all correspondence to: abhivyakti.gautam2191@gmail.com

References

[1] Arenkiel BR, Peca J, Davison IG, Feliciano C, Deisseroth K, Augustine GJ, et al. In vivo light-induced activation of neural circuitry in transgenic mice expressing channelrhodopsin-2. Neuron. 2007;**54**(2):205-218

[2] Boyden ES, Zhang F, Bamberg E, Nagel G, Deisseroth K. Millisecond-timescale, genetically targeted optical control of neural activity. Nature Neuroscience. 2005;**8**(9):1263-1268

[3] Zhang F, Gradinaru V, Adamantidis AR, Durand R, Airan RD, de Lecea L, et al. Optogenetic interrogation of neural circuits: Technology for probing mammalian brain structures. Nature Protocols. 2010;**5**:439-456

[4] Chen R, Canales A, Anikeeva P. Neural recording and modulation technologies. Nature Reviews Materials. 2017;**2**:16093

[5] Jeong JW, McCall JG, Shin G, Zhang Y, Al-Hasani R, Kim M, et al. Wireless optofluidic systems for programmable in vivo pharmacology and optogenetics. Cell. 2015;**162**(3):662-674

[6] Kim CK, Adhikari A, Deisseroth K. Integration of optogenetics with complementary methodologies in systems neuroscience. Nature Reviews Neuroscience. 2017;**18**(4):222-235

[7] Won SM, Song E, Reeder JT, Rogers JA. Emerging modalities and implantable technologies for neuromodulation. Cell. 2020;**181**(1):115-135

[8] O'Shea DJ, Kalanithi P, Ferenczi EA, Hsueh B, Chandrasekaran C, Goo W, et al. Development of an optogenetic toolkit for neural circuit dissection in squirrel monkeys. Scientific Reports. 2018;**8**(1):6775

[9] Gautam A. Investigation of Electrochemical Kinetics of Glassy Carbon Probe and Self-Powering Probe through Integrated GC Supercapacitor. [Doctoral Dissertation]. San Diego: San Diego State University; 2020

[10] Buzsáki G, Anastassiou CA, Koch C. The origin of extracellular fields and currents—EEG, ECoG, LFP and spikes. Nature Reviews Neuroscience. 2012;**13**(6):407-420

[11] Yang T, Hakimian S, Schwartz TH. Intraoperative ElectroCorticoGraphy (ECog): Indications, techniques, and utility in epilepsy surgery. Epileptic Disorders. 2014;**16**(3):271-279

[12] Zhang F, Prigge M, Beyrière F, Tsunoda SP, Mattis J, Yizhar O, et al. Red-shifted optogenetic excitation: A tool for fast neural control derived from Volvox carteri. Nature Neuroscience. 2008;**11**(6):631-633

[13] Rudmann L, Alt MT, Vajari DA, Stieglitz T. Integrated optoelectronic microprobes. Current Opinion in Neurobiology. 2018;**50**:72-82

[14] Cho IJ, Baac HW, Yoon E. A 16-site neural probe integrated with a waveguide for optical stimulation. In: 2010 IEEE 23rd International Conference on Micro Electro Mechanical Systems (MEMS) 2010 Jan 24. Hong Kong, China: IEEE; 2010. pp. 995-998

[15] Schwaerzle M, Nehlich J, Schwarz UT, Paul O, Ruther P. Hybrid polymer waveguide characterization for microoptical tools with integrated laser

diode chips for optogenetic applications at 430 nm and 650 nm. In: Clinical and Translational Neurophotonics; Neural Imaging and Sensing; and Optogenetics and Optical Manipulation 2016 Mar 9. Vol. 9690. San Francisco, California, United States: SPIE; 2016. pp. 262-265

[16] Lee J, Ozden I, Song YK, Nurmikko AV. Transparent intracortical microprobe array for simultaneous spatiotemporal optical stimulation and multichannel electrical recording. Nature Methods. 2015;**12**(12):1157-1162

[17] Son Y, Jenny Lee H, Kim J, Shin H, Choi N, Justin Lee C, et al. In vivo optical modulation of neural signals using monolithically integrated two-dimensional neural probe arrays. Scientific Reports. 2015;**5**(1):15466

[18] Schwaerzle M, Ringwald P, Paul O, Rüther P. First dual-color optrode with bare laser diode chips directly butt-coupled to hybrid-polymer waveguides. In: 2017 IEEE 30th International Conference on Micro Electro Mechanical Systems (MEMS) 2017 Jan 22. Las Vegas, NV, USA: IEEE; 2017. pp. 526-529

[19] Rubehn B, Wolff SB, Tovote P, Lüthi A, Stieglitz T. A polymer-based neural microimplant for optogenetic applications: Design and first in vivo study. Lab on a Chip. 2013;**13**(4):579-588

[20] Chamanzar M, Denman DJ, Blanche TJ, Maharbiz MM. Ultracompact optoflex neural probes for high-resolution electrophysiology and optogenetic stimulation. In: 2015 28th IEEE International Conference on Micro Electro Mechanical Systems (MEMS) 2015 Jan 18. Estoril, Portugal: IEEE; 2015. pp. 682-685

[21] Kawano T. 3D microtube and 2D flexible film waveguide devices. In: 2016 International Conference on Optical MEMS and Nanophotonics (OMN) 2016 Jul 31. Singapore: IEEE; 2016. pp. 1-2

[22] Li W, Fan B, Yong K, Weber A. Microfabricated optoelectronic neural implants for optogenetics. IEEE Sensors; 2015. pp. 1-4

[23] Yamagiwa S, Ishida M, Kawano T. Flexible optrode array: Parylene-film waveguide arrays with microelectrodes for optogenetics. In: 2015 Transducers-2015 18th International Conference on Solid-State Sensors, Actuators and Microsystems (TRANSDUCERS) 2015 Jun 21. Anchorage, AK, USA: IEEE; 2015. pp. 277-280

[24] Reddy JW, Lassiter M, Chamanzar M. Parylene photonics: A flexible, broadband optical waveguide platform with integrated micromirrors for biointerfaces. Microsystems & Nanoengineering. 2020;**6**(1):85

[25] Reddy JW, Chamanzar M. Low-loss flexible Parylene photonic waveguides for optical implants. Optics Letters. 2018;**43**(17):4112-4115

[26] Ahmed Z, Reddy JW, Malekoshoaraie MH, Hassanzade V, Kimukin I, Jain V, et al. Flexible optoelectric neural interfaces. Current Opinion in Biotechnology. 2021;**72**:121-130

[27] Kim K, English D, Mckenzie S, Wu F, Stark E, Seymour J, et al. GaN-on-Si μLED optoelectrodes for high-spatiotemporal-accuracy optogenetics in freely behaving animals. In: 2016 IEEE International Electron Devices Meeting (IEDM) 2016 Dec 3. San Francisco, CA, USA: IEEE; 2016. pp. 26-25

[28] Tokuda T, Takehara H, Noda T, Sasagawa K, Ohta J. CMOS-based optoelectronic on-chip neural

interface device. IEICE Transactions on Electronics. 2016;**99**(2):165-172

[29] Wu F, Stark E, Ku PC, Wise KD, Buzsáki G, Yoon E. Monolithically integrated μLEDs on silicon neural probes for high-resolution optogenetic studies in behaving animals. Neuron. 2015;**88**(6):1136-1148

[30] Zhang H, Pei W, Yang X, Guo X, Xing X, Liu R, et al. A sapphire based monolithic integrated optrode. In: 2016 38th Annual International Conference of the IEEE Engineering in Medicine and Biology Society (EMBC) 2016 Aug 16. Orlando, FL, USA: IEEE; 2016. pp. 6186-6189

[31] Keppeler D, Schwaerzle M, Harczos T, Jablonski L, Dieter A, Wolf B, et al. Multichannel optogenetic stimulation of the auditory pathway using microfabricated LED cochlear implants in rodents. Science Translational Medicine. 2020;**12**(553):eabb8086

[32] Reddy JW, Kimukin I, Ahmed Z, Towe E, Chamanzar M. High density, double-sided, flexible optoelectrical neural probes with embedded micro-LEDs. Frontiers in Neuroscience. 2019;**13**:572

[33] Lecomte A, Descamps E, Bergaud C. A review on mechanical considerations for chronically-implanted neural probes. Journal of Neural Engineering. 2018;**15**(3):031001

[34] Jia Y, Khan W, Lee B, Fan B, Madi F, Weber A, et al. Wireless opto-electro neural interface for experiments with small freely behaving animals. Journal of Neural Engineering. 2018;**15**(4):046032

[35] Libbrecht S, Hoffman L, Welkenhuysen M, Van den Haute C, Baekelandt V, Braeken D, et al. Proximal and distal modulation of neural activity by spatially confined optogenetic activation with an integrated high-density optoelectrode. Journal of Neurophysiology. 2018;**120**(1):149-161

[36] Segev E, Reimer J, Moreaux LC, Fowler TM, Chi D, Sacher WD, et al. Patterned photostimulation via visible-wavelength photonic probes for deep brain optogenetics. Neurophotonics. 2017;**4**(1):011002

[37] Elwassif MM, Kong Q, Vazquez M, Bikson M. Bio-heat transfer model of deep brain stimulation-induced temperature changes. Journal of Neural Engineering. 2006;**3**(4):306

[38] Yarmolenko PS, Moon EJ, Landon C, Manzoor A, Hochman DW, Viglianti BL, et al. Thresholds for thermal damage to normal tissues: An update. International Journal of Hyperthermia. 2011;**27**(4):320-343

[39] Sridharan A, Shah A, Kumar SS, Kyeh J, Smith J, Blain-Christen J, et al. Optogenetic modulation of cortical neurons using organic light emitting diodes (OLEDs). Biomedical Physics & Engineering Express. 2020;**6**(2):025003

[40] Yasunaga H, Takagi T, Shinko D, Nakayama Y, Takeuchi Y, Nishikawa A, et al. Development of a neural probe integrated with high-efficiency MicroLEDs for in vivo application. Japanese Journal of Applied Physics. 2020;**60**(1):016503

[41] Khan W, Setien M, Purcell E, Li W. Micro-reflector integrated multichannel μLED optogenetic neurostimulator with enhanced intensity. Frontiers in Mechanical Engineering. 2018;**4**:17

[42] Anikeeva P. Biocompatible materials for optoelectronic neural probes: Challenges and opportunities. The Bridge Frontiers of Engineering. 2013;**43**(4)

[43] Rudmann L, Huber SD, Ordonez JS, Stieglitz T. Fused silica microlenses for hermetic packages as part of implantable optrodes. In: 2015 37th Annual International Conference of the IEEE Engineering in Medicine and Biology Society (EMBC) 2015 Aug 25. Milan, Italy: IEEE. pp. 7143-7146

[44] Park SI, Brenner DS, Shin G, Morgan CD, Copits BA, Chung HU, et al. Soft, stretchable, fully implantable miniaturized optoelectronic systems for wireless optogenetics. Nature Biotechnology. 2015;**33**(12):1280-1286

[45] Ho JS. Fully internal, wirelessly powered systems for optogenetics. In: 2016 International Conference on Optical MEMS and Nanophotonics (OMN) 2016 Jul 31. Singapore: IEEE; 2016. pp. 1-2

[46] Canales A, Jia X, Froriep UP, Koppes RA, Tringides CM, Selvidge J, et al. Multifunctional fibers for simultaneous optical, electrical and chemical interrogation of neural circuits in vivo. Nature Biotechnology. 2015;**33**(3):277-284

[47] Qazi R, Gomez AM, Castro DC, Zou Z, Sim JY, Xiong Y, et al. Wireless optofluidic brain probes for chronic neuropharmacology and photostimulation. Nature Biomedical Engineering. 2019;**3**(8):655-669

[48] Sim JY, Haney MP, Park SI, McCall JG, Jeong JW. Microfluidic neural probes: in vivo tools for advancing neuroscience. Lab on a Chip. 2017;**17**(8):1406-1435

[49] Noh KN, Park SI, Qazi R, Zou Z, Mickle AD, Grajales-Reyes JG, et al. Miniaturized, battery-free optofluidic systems with potential for wireless pharmacology and optogenetics. Small. 2018;**14**(4):1702479

Edited by Touseef Para

Embark on a journey through the cutting-edge world of optoelectronics with *Optoelectronics - Recent Advances*. This anthology explores the diverse realms of light and electronics, from fundamental insights to groundbreaking advancements. Discover the future of quantum information processing, gold nanorod assembly, and more. This collection of seven chapters brings together leading minds, offering a glimpse into the transformative potential of recent optoelectronic research. Whether you're a curious reader or a seasoned researcher, *Optoelectronics - Recent Advances* invites you to witness the brilliance where ideas shine bright.

Published in London, UK

IntechOpen

ISBN 978-1-83769-797-7